





This is to certify that the  
dissertation entitled


**NANOPARTICLE-POLYMER COMPOSITE MEMBRANES:  
SYNTHESIS, CHARACTERIZATION AND ENVIRONMENTAL  
APPLICATIONS**

presented by

**JULIAN S. TAUROZZI**

has been accepted towards fulfillment  
of the requirements for the

Ph.D. degree in Environmental Engineering

  
\_\_\_\_\_  
Major Professor's Signature

September 16, 2009

Date

**PLACE IN RETURN BOX** to remove this checkout from your record.  
**TO AVOID FINES** return on or before date due.  
**MAY BE RECALLED** with earlier due date if requested.

DATE DUE	DATE DUE	DATE DUE

**NANOPARTICLE-POLYMER COMPOSITE MEMBRANES: SYNTHESIS,  
CHARACTERIZATION, AND ENVIRONMENTAL APPLICATIONS**

By

Julian S. Taurozzi

A DISSERTATION

Submitted to  
Michigan State University  
In partial fulfillment of the requirements  
For the degree of

DOCTOR OF PHILOSOPHY

Environmental Engineering

2009

## **ABSTRACT**

# **NANOPARTICLE-POLYMER COMPOSITE MEMBRANES: SYNTHESIS, CHARACTERIZATION, AND ENVIRONMENTAL APPLICATIONS**

by

Julian S. Taurozzi

Advances in nanotechnology and materials science offer new possibilities for the development of novel water treatment technologies. A salient example is the emergence of a new generation of nanostructured membranes with improved separation properties and, in some cases, multifunctional capabilities. The present work explores different aspects of the formation of nanoparticle-enabled membranes, focusing on the dependence between synthetic methods, nanoparticle properties, and the performance of the obtained membranes.

The effects of nanoparticle loading, size and morphology, and methods of nanoparticle incorporation on the functional properties of the resulting nanocomposite membranes are studied. Additionally, empirical predictors of membrane performance for the rational design of nanocomposite membranes and novel strategies for the manufacture of membrane-based sensors and biofouling resistant membrane spacers are presented.

The first chapter of the dissertation provides an overview of the theory of phase inversion in polymer blends – one of the main methods for the fabrication of ultrafiltration membranes. The second chapter describes the study of the effect of shape and loading of

carbon nanoparticle fillers on the hydraulic properties of nanocomposite membranes. In the third chapter, the effects of casting mixture composition and nanoparticle incorporation route on the morphological structure and separation performance of nanocomposite membranes are described and the potential use of these nanocomposites for the mitigation of membrane biofouling is discussed. Finally, in the last chapter, a method for the synthesis of a nanoparticle-enabled, membrane-based sensor for water quality control is presented.

Copyright by  
JULIAN S. TAUROZZI  
2009

## **ACKNOWLEDGEMENTS**

This work would not have been possible without the unconditional support and guidance of my PhD advisor and committee chairman, Dr. Volodymyr V. Tarabara. I would like to specially thank him for his invaluable advice, insightful discussions and permanent encouragement and instruction towards the execution of every task with the highest level of excellence.

I would like as well to express my deep gratitude to my committee members: Dr. Merlin L. Bruening, Dr. Thomas C. Voice, Dr. Alison M. Cupples and Dr. Jerome Rose, for their positive feedback, supportive disposition and constructive criticism.

I wish to thank former and current members of my research group at the Environmental Nanotechnology Research Lab: Dr. Fulin Wang, Dr. Jeonghwan Kim, Dr. Seokjong Byun, Wenqian Shan, Alla Alpatova, Elodie Pasco and Adam R. Rogensues, for their wholehearted help and unreserved assistance in conducting experiments, analyzing data, discussing results and enabling a warm and amiable work environment.

My special thanks to Ms. Lori Hasse and Mr. Yang-lyang Pan for their constant administrative and technical support.

My gratitude to Dr. Baokang Bi, Dr. Alicia Pastor-Lecha, Dr. Melinda Frame, Ms. Ewa Danielewicz and Ms. Carol S. Flegler for the helpful discussions and inestimable aid in the conduction of microscopy experiments.

I would like to stress my endless appreciation to the Department of Civil and Environmental Engineering at Michigan State University and the National Science Foundation for their financial support throughout my PhD.

Finally, I wish to express my eternal gratitude to my family, and specially my mother and sister, for their relentless support, unconditional love and endless patience.

## TABLE OF CONTENTS

LIST OF TABLES.....	x
LIST OF FIGURES .....	xi
INTRODUCTION .....	1
Significance and application potential.....	3
Multifunctional membranes.....	4
Hydraulic properties.....	5
Mechanical properties.....	7
Tunable hydrophilicity.....	9
Adaptive membranes .....	11
Dissertation Overview .....	14
References.....	16
CHAPTER ONE .....	21
Theoretical backgorund of the phase inversion process .....	21
1.1. Phase Inversion.....	21
1.2.Liquid-Liquid Demixing.....	23
1.3.Ternary system demixing.....	35
1.4.Wet phase inversion.....	44
1.4.1.Solvent/non solvent affinity .....	49
1.4.2.Polymer concentration in the casting mixture .....	50
1.4.3.Addition of non solvent to the casting mixture.....	52
1.4.4.Immersion bath temperature .....	54
1.4.5.Addition of solvent to the immersion bath .....	56
References.....	58
CHAPTER TWO .....	59
Fullerene-polysulfone nanocomposite ultrafiltration membranes: Effect of filler shape and loading on membrane properties.....	60
Abstract.....	60
2.1 Introduction.....	61
2.2 Experimental .....	64
2.2.1 Materials .....	64
2.2.2 Preparation of polysulfone membranes .....	64
2.2.2.1 Preparation of nanoparticle-filled membranes.....	66
2.2.3 Characterization of casting mixtures and cast membranes .....	67
2.3. Results and Discussion .....	69
2.3.1 Casting mixture properties.....	69
2.3.1.1 Nanoparticle dispersions in N-methyl-pyrrolidone .....	69
2.3.1.2 Viscosity of nanoparticle (C <sub>60</sub> ) – polymer (PSf) – solvent (NMP) – porogen (PVP) blends: Effect of nanoparticle loading .....	69

2.3.1.3 Demixing behavior of polymer (PSf) – nanoparticle (nC <sub>60</sub> ) – solvent (NMP) – porogen (PVP) blends exposed to nonsolvent (water): Effect of nanoparticle loading.....	72
2.3.2 Membrane hydraulic properties .....	76
2.3.3 Nanocomposite membranes doped with nanoparticles of different shapes .....	78
2.4. Conclusions.....	81
Supporting Documentation .....	84
References.....	92
<b>CHAPTER THREE .....</b>	<b>96</b>
Effect of filler incorporation route on the properties of polysulfone-silver nanocomposite membranes of different porosities .....	97
Abstract.....	97
3.1 Introduction.....	98
3.2 Experimental .....	102
3.2.1 Materials .....	102
3.2.2 Preparation of polysulfone membranes .....	102
3.2.3 Preparation of polysulfone-silver nanocomposite membranes .....	105
3.2.4 Characterization of membranes: SEM, TEM, EDS, FTIR, XPS .....	106
3.2.5 Permeability and rejection tests .....	107
3.2.6 Measuring silver losses .....	108
3.2.7 Membrane biofouling characterization .....	109
3.2.7.1 Biofilm growth inhibition under diffusive conditions .....	109
3.2.7.2 Biofilm growth inhibition under convective conditions .....	110
3.2.7.3 Assessment of silver leaching.....	111
3.3. Results and Discussion .....	113
3.3.1 Silver-free polysulfone membranes .....	113
3.3.1.1 Surface morphology.....	114
3.3.1.2 Cross-sectional morphology .....	114
3.3.2 Polysulfone-silver nanocomposite membranes.....	116
3.3.2.1 Cross-sectional morphology .....	116
3.3.2.2 Surface morphology.....	118
3.3.2.3 Formation-structure links for nanocomposite membranes .....	121
3.3.2.4 Permeability and rejection of nanocomposite membranes .....	123
3.3.3 Antibacterial properties of nanocomposites.....	125
3.3.4 Practical aspects of the application of silver nanocomposites as membrane and membrane spacer materials.....	130
3.3.4.1 Effect of antibacterial activity on the efficiency of hydraulic cleaning..	130
3.3.4.2 Antibacterial efficiency of nanocomposite membranes under convective transport conditions.....	131
3.4. Conclusions.....	135
Acknowledgements.....	137
Supporting Documentation .....	138
References.....	151
<b>CHAPTER FOUR.....</b>	<b>155</b>

Silver nanoparticle arrays on track etch membrane support as flow-through optical sensors for water quality control.....	156
Abstract.....	156
4.1. Introduction.....	157
4.2. Experimental.....	161
4.2.1 Materials .....	161
4.2.2 Synthesis of silver nanoparticles.....	161
4.2.3 Membranes and membrane surface modification.....	162
4.2.3.2 APTMS used as a linker .....	163
4.2.3.3 CysA used as a linker.....	164
4.2.4 XPS, UV-vis, Raman and SERS measurements.....	164
4.2.5 Particle size and zeta potential measurements.....	167
4.2.6 SEM and TEM imaging.....	167
4.2.7 SERS characterization of APTMS modified membranes.....	168
4.2.8 Membranes filtration performance .....	168
4.2.9 Preconcentration studies .....	169
4.3. Results and Discussion .....	170
4.3.1 Silver nanoparticle hydrosol .....	170
4.3.2 Modified membranes characterization.....	173
4.3.2.1 Surface chemistry.....	173
4.3.2.2 Silver nanoparticle array morphology .....	174
4.3.2.3 Optical properties of modified membranes.....	176
4.3.2.4 Filtration performance of modified membranes .....	184
4.3.2.5 Preconcentration .....	187
4.4. Conclusions.....	192
Acknowledgements.....	193
References.....	194

## LIST OF TABLES

Table 2.1.Components of membrane casting mixtures (% w/w). Weight % of filler is expressed with respect to the mass of PSf. ....	65
Table SD.2.1.Cluster sizes for different silica powders sonicated at a variety of intensities and times. 100 % sonication intensity corresponds to a maximum power output of 600 W. PEG denotes Polyethyleneglycol (400 Mw). ....	89
Table 3.1.Components of membrane casting mixture (% mass) .....	104
Table 3.2.Resistance and rejection values for all membrane types. Mass fractions of silver were the same for PSf/Ag <sup>ex</sup> and PSf/Ag <sup>in</sup> casting mixtures.....	124
Table SD.3.1.Statistical data analysis for released protein on diffusive biofouling experiments without hydraulic rinsing (Figure 3.5 of main document). Mean values are normalized to that of PSf/Type I membranes, errors are calculated with a 90% confidence level, the “t values” columns indicate the comparative basis for each pair. ....	149
Table SD.3.2.Statistical data analysis for released protein on convective biofouling experiments (Figure 3.6 of main document). Mean values are normalized to that of PSf/Type I membranes, errors are calculated with a 90% confidence level, the “t values” columns indicate the comparative basis for each pair.....	150

## LIST OF FIGURES

Figure 1.1. Plot of $\Delta G_m$ vs. $\phi_2$ for the polymer/solvent system at temperature $T_4$ , above the critical point. ....	26
Figure 1.2. Polymer/solvent system's $\Delta G_m$ vs. $\phi_2$ plot at a temperature $T_2$ below the critical point .....	29
Figure 1.3. $\Delta G_m$ vs. $\phi_2$ curves for the polymer/solvent system at different temperatures, from the completely mixed system at $T_4$ , above the critical temperature ( $T_c$ ), to $T_1$ , final temperature of the demixed system. ....	34
Figure 1.4. Ternary phase diagram of a three component system (solvent, non-solvent and polymer). ....	37
Figure 1.5. Solubility diagram for the three component system, showing the binodal and spinodal curves, tie lines, and the critical point. ....	39
Figure 1.6. Demixing and gelation regions for the three component system. ....	42
Figure 1.7. Schematic of solvent ( $J_S$ ) and non-solvent ( $J_{NS}$ ) transport for the wet phase inversion process. ....	45
Figure 1.8. Demixing paths for a three component system during wet phase inversion ...	47
Figure 1.9. Effect of polymer concentration (point a*) on the demixing path of ternary system .....	51
Figure 1.10. Effect of non solvent addition to the casting mixture (point a*) on the demixing path of ternary system. ....	53
Figure 1.11. Effect of temperature increase on the demixing path of the ternary system. ....	55
Figure 1.12. Effect of solvent addition to the coagulation bath on the demixing path of ternary system. ....	57
Figure 2.1. Viscosity and demixing front propagation rate for PSf-PVP- $C_{60}$ blends (a) and hydraulic resistance and 150 kDa rejection for $C_{60}$ -filled PSf membranes (b) at 0% (control), 0.7 % and 10 % w/w $C_{60}$ /PSf loadings. ....	70
Figure 2.2. Schematic (A) of an isothermal phase diagram for a three component (solvent-polymer-nonsolvent) system and laser-scanned brightfield images (B) of demixing front propagation in PSf- $C_{60}$ -PVP-NMP blends as a function of time (in seconds) of exposure to nonsolvent (water). ....	75

Figure 2.3. Hydraulic resistance (circles) and rejection (triangles) of 150 kDa dextran for PSf membranes filled with C <sub>60</sub> and SWCNTs at a filler/polymer weight loading of 0.7 %. .....	79
Figure SD.2.1. SEM images of 1 mg/mL SWCNT/NMP (A) and C <sub>60</sub> /NMP (B) organosols. ....	86
Figure SD.2.2. Cloud points for PSf-NMP-water system. ....	88
Figure SD.2.3. Front thickness vs. the square root of time plots for 0, 0.7 and 10 % C <sub>60</sub> loading casting mixtures. ....	91
Figure 3.1. SEM surface (a, b, c) and cross-section (d, e, f) images of PSf Type I (a, d), Type II (b, e) and Type III (c, f) membranes. Inset A shows the permeate side surface of PSf Type II membranes. ....	115
Figure 3.2. Schematic illustration of the distribution of silver nanoparticles in the silver-polysulfone nanocomposites prepared using different methods of silver incorporation. On micrographs, the black dots with arrows pointing to them correspond to silver nanoparticles. TEM micrographs (A, C and D) show membrane cross-sections, while SEM micrograph (B) shows the top cross section layer, with large silver clusters embedded into the polysulfone matrix. ....	117
Figure 3.3. Representative SEM images of the surfaces of PSf Type I (a), PSf/Ag <sup>in</sup> Type I (b) and PSf/Ag <sup>ex</sup> Type I (c) membranes. ....	120
Figure 3.4. Typical SEM images of the surface of biofouled PSf Type I silver-free (a), PSf/Ag <sup>in</sup> (b) and PSf/Ag <sup>ex</sup> (c) membranes. Evident is the stark contrast between the thick biofilm developed on the surface of a silver-free membrane (a), and the absence of biofilm growth on the nanocomposite surface. The sample preparation procedure is detailed in section 3.2.4. ....	127
Figure 3.5. Bradford assay results describing the biofilm growth on the surface of PSf membranes and PSf/Ag nanocomposites of different porosities under diffusive transport conditions. ....	129
Figure 3.6. Biofilm growth on PSf/Ag Type I nanocomposites after 48 hr of continuous filtration of a) LB medium (first two columns) and b) leachate obtained by continuously filtering DI water through PSf/Ag Type I nanocomposite for 2 days (third column). The leachate was Ag-loaded water obtained from the filtration of DI water through a bacteria-free PSf/Ag Type I nanocomposite; the leachate was then mixed with LB medium to be filtered through an inoculated Ag-free membrane. ..	133
Figure SD.3.1. TEM image (top) of silver nanoparticles (Spectrum 1) embedded in the PSf matrix (Spectrum 2) of a PSf/Ag <sup>in</sup> Type I membrane, and EDS spectra (bottom) of both the PSf matrix (yellow filled spectrum) and the Ag nanoparticles (line	

spectrum) showing the silver peaks for the nanoparticle. The x-axis for the EDS spectra is in KeV units. ....	141
Figure SD.3.2.FTIR spectra of PSf Type I (Top) and PSf/Ag <sup>in</sup> Type I (bottom) membranes. ....	143
Figure SD.3.3.XPS survey spectrum and atomic concentration (relative) table for a PSf/Ag <sup>in</sup> Type I membrane. The silver signal is not visible in the survey spectrum. ....	145
Figure SD.3.4.Bradford assay results describing the biofilm growth on the surface of PSf membranes and PSf/Ag nanocomposites of different porosities under diffusive transport conditions, both with and without hydraulic rinsing. ....	147
Figure 4.1.Proposed mechanism for the APTMS reaction with polycarbonate and further silver chemisorption to the incorporated nitrogen. ....	165
Figure 4.2.Micrographs of Ag nanoparticles: SEM image of filtered hydrosol (A), and TEM image of Ag nanoparticles deposited onto TEM grids by drop-coating (B). ....	171
Figure 4.3.Size distribution profile of silver nanoparticle suspension. Also shown are the predominant spherical diameters for the two major distribution peaks, and the estimated rod lengths for the two high end size peaks (Schematics not to scale) ..	172
Figure 4.4.SEM micrographs of PCTE membrane filter that is non-modified (A), modified using APTMS linker (B, C, D), and modified using CysA linker (E, F). ....	175
Figure 4.5.UV-vis spectra of a modified PCTE membrane (bare membrane used as baseline), and of silver hydrosol (250 $\mu$ L in 2 mL ultrapure water, ultrapure water used as baseline). ....	177
Figure 4.6.Absorption (A) and Raman spectra (B) of methylene blue. ....	179
Figure 4.7.Raman spectra of an untreated membrane (bottom) and modified membrane (top). ....	180
Figure 4.8.Raman spectrum of a 1 mmol/L aqueous solution of MB (bottom), a $10^{-5}$ mol/L aqueous solution of MB in pre-coagulated silver sol (middle), and a $10^{-5}$ mol/L aqueous solution of methylene blue after “drop and dry” on a modified membrane (top). ....	183
Figure 4.9.Box plots for enhancement factors of MB on precoagulated sol and modified membranes (A) and after preconcentration of modified membranes (B). ....	185
Figure 4.10.Results of clean water flux test for bare and modified membranes. ....	186

Figure 4.11. Raman spectrum of a  $10^{-7}$  mol/L aqueous solution of MB after 2 hours of pre-concentration on a modified membrane. .... 188

**Images in this dissertation are presented in color**

# INTRODUCTION

## **Nanoparticle-polymer composite membranes: Synthesis, characterization, and environmental applications**

Membrane-based separation is a well established water treatment process and an integral component in a growing number of drinking water and wastewater treatment facilities. A membrane is a semi-permeable barrier designed for the separation of targeted compounds from source waters. Membranes perform a variety of operations involving the removal of pollutants from contaminated waters, the recovery of valuable or recyclable components from treated streams, or the identification and quantification of targeted compounds. The versatility of membranes in treating source waters is further enhanced by their minimal environmental footprint.

An emerging field of materials engineering with promising applications for membrane manufacture is that focused on the development of Nanocomposites. Nanocomposites are materials that combine two or more components, wherein at least one of the components has nanoscale dimensions. Materials at the nanoscale - or nanoparticles - with at least one dimension of less than 100 nm, exhibit unique properties that are fundamentally different from those observed for the same materials at the macroscopic scale. Nanocomposite structures thus incorporate distinctive properties to yield exceptional mechanical, thermal, or electrical features, among others.

The increasing choice of available nanoparticles offers new possibilities for the manufacture of a new generation of nanoenabled membranes. Examples of such potential include the bottom-up design of nanoparticle-enabled multifunctional membranes capable of performing multiple tasks or the incorporation of nanoparticles within the membrane structure to obtain membranes with improved mechanical and separation properties. Research at the interface of nanomaterials science and membrane manufacture holds promise for more efficiently safeguarding the quality and ensuring the availability of drinking water.

## **Significance and application potential**

The expanding availability and diversity of nanoparticles stresses the potential of their application towards the synthesis of a new generation of nanoparticle-enabled membranes. Exceptional features such as supramagnetism or enhanced catalytic and optical properties have been reported for nanoparticles of different materials, while the possibility of chemically functionalizing the nanoparticle surface further broadens the spectrum of potential nanoenabled features [1, 2].

A conventional approach for the synthesis of nanocomposite membranes relies on the incorporation of nanoparticles to a polymer blend or a pre-formed membrane. The development of such porous nanocomposites however, should not be undertaken without focusing on issues that will affect the operational viability of the final product. The structure of the resulting membranes can be expected to be a function of the physical and chemical properties of both the polymer phase and nanoparticles, as well as the method of nanoparticle incorporation. However, only a few of the studies available to date have focused on the understanding of links between the operational properties of the obtained membranes, and the characteristics and incorporation method of the nanoparticles.

In what follows, different examples of the application potential of the use of nanoparticles towards the development of novel or improved membrane-based water treatment strategies, and the importance of understanding the underlying mechanisms and fundamental aspects of nanocomposite membrane manufacture are discussed.

## Multifunctional membranes

*Multifunctional membranes couple separation with one or more additional functions, allowing for a decrease in operational redundancy and thus lowering overall costs and minimizing the environmental footprint.*

The increasing availability and diversity of nanoparticles with unique physicochemical properties is opening up new possibilities for the fabrication of multifunctional membranes. An example of multifunctional membranes is that of membrane-based sensors [3, 4], which couple the separation and pre-concentration functions afforded by the membrane with additional sensing features, allowing for the detection, identification and quantification of targeted compounds as they are separated from treated streams.

*This dissertation (Chapter 4) describes a novel approach for the synthesis of a nanoparticle-enabled membrane sensor.*

Another example of multifunctional membranes are those which can controllably release a specific compound to the treated stream [5-7]. Such membranes are of special interest for the mitigation of biofouling, a major cause of membrane breakdown and high replacement costs. In particular, silver nanoparticles show promise as nanoscale fillers that can controllably release bactericidal silver ions directly into the membrane feed stream and thus prevent the formation of biofilm on the membrane surface. *Chapter 3 describes the synthesis and characterization of polysulfone-silver nanocomposite membranes and their potential towards biofouling prevention and control.*

## Hydraulic properties

*Wet phase inversion is the main method of preparation of integrally skinned, polymeric ultrafiltration membranes [8, 9]. A comprehensive, systematic study of the connection between the process of phase inversion in nanoparticle-polymer blends, and the properties of the resulting membranes is thus required. The results of the studies published to date strongly imply that the microstructural changes induced by nanoparticle incorporation can potentially be controlled, to prepare membranes with desirable hydraulic properties.*

Recent works on the incorporation of nanoparticles using the wet phase inversion process have resulted in the development of membranes with enhanced hydraulic performance (significant simultaneous improvement of fluxes and selectivities).

Available knowledge on the processes governing the formation of porous nanocomposite membranes is insufficient and limited in scope. Most studies published so far involved the incorporation of passive fillers into polymeric matrices and indicated that the presence of nanoparticles affected both the porosity (pore size and density) of the membrane skin and the macrovoid morphology of the asymmetric support layer [6, 10-23]. A number of such published studies described the synthesis of organic-inorganic porous (10 kDa to 200 kDa) composite membranes by adding particles to the solution of the membrane-forming polymer [6, 10-23]. Incorporation of increasing loadings of silica

nanoparticles into polysulfone membranes was reported to result in higher porosity and interconnectedness of macrovoid walls [12], increased density and size of surface pores and thicker skin layer [11]. For clay-polysulfone composite membranes, skin layer thickness was found to decrease with increasing clay loadings [21]. Macrovoid suppression and increased porosity and thickness of the membranes skin layer for higher filler concentrations was also reported for hybrid  $\text{TiO}_2$ -polysulfone ultrafiltration membranes [19]. Similarly, incorporation of activated carbon was found to diminish macrovoid formation in composite polysulfone membranes; while the cross sectional asymmetry and the uniformity in the mean pore size of membranes increased with an increase in the size of carbon filler particles [24]. In a recent study, nanotube fillers were used to prepare a nanocomposite PSf membrane with acid-treated multiwall carbon nanotubes [25]. The average porosity of the composite membranes peaked at a nanotube loading of 1.5%, which also corresponded to the highest permeate flux. Interestingly, the only pronounced change in membrane macroscopic morphology was an increase in surface roughness.

These studies proved that skin layer properties (porosity, surface porosity, thickness) as well as the macrovoid morphology of the support layer can be affected by nanoparticle incorporation. Both of these structurally distinct membrane regions (skin and support) are important; the skin layer determines the permeability, rejection, and selectivity of membranes, while the structure of the support layer affects its compaction behavior [26, 27].

*It is thus important to understand the links between nanofiller shape, size and inclusion methodology, (namely loading concentration and synthetic incorporation route); and, the effect of these parameters on the morphological structure of the nanofilled porous matrix. This is the main focus of Chapters 2 and 3 of this dissertation.*

## **Mechanical properties**

Mechanical stability is of major importance for membranes, as it is required to prevent structural breakage at high pressures and thus ensure the membrane's operational viability. *Improvement of the mechanical properties of polymeric membranes via nanoparticle incorporation into polymer blends is a design strategy that is earning considerable attention.*

In recent studies on the development of polymer nanocomposites, significant improvements in tensile stiffness and strength, toughness, rigidity and impact resistance were found to be directly dependent on nanoparticle size and loading [28-33]. Tensile strength and elongation-at-break of UF polyvinylidene fluoride (PVDF) membranes prepared by phase inversion were improved by 50% upon addition of 10 nm alumina particles at a 2 % wt loading [15]. A significant increase in tensile modulus was also reported for polysulfone-clay composite membranes [21]. Yang et al. [19] reported a significant improvement in breaking and bursting strength values for porous UF polysulfone membranes upon incorporation of TiO<sub>2</sub> nanoparticles (30 nm) via phase inversion. Separately, Li et al. [22] showed that TiO<sub>2</sub> nanoparticle (10-20 nm) filled,

phase inversion polyphthalazinone ether sulfone ketone (PPESK) membranes exhibited a remarkable enhancement of tensile strength as compared to  $\text{TiO}_2$  free membranes.

A common undesirable feature of porous polymeric membranes is the decrease in permeate flow due to compaction. Given their intrinsically flexible nature and porous, sponge-like morphology, the matrices of polymeric membranes can be compressed under sufficiently high pressure, resulting in pore constriction and a consequent decline in flow. Compaction is thus detrimental to process efficiency, due to the reduction of permeate flux and increased energy costs, since higher pressures are needed to compensate for the decline in flux upon compaction. *Mitigation of membrane compaction is yet another benefit of improving the mechanical robustness of membranes. The introduction of nanoparticles to the bulk membrane material and could reduce the membrane compaction and thus reduce operating costs.*

Nunes et al. [34] studied the *in situ* formation of silica nanoparticles within porous polyetherimide (PEI) phase inversion membranes, used as supports for dense composite membranes. The nanoparticle-filled membranes experienced a permeate flow loss of only 10% upon compaction, as compared to a higher than 60% permeate loss for silica-free membranes. In a later work, Ebert et al. [16] observed a significant reduction (more than 50 %) in flux loss upon compaction for porous, phase inversion,  $\text{TiO}_2$  nanoparticle filled PVDF membranes, with respect to nanoparticle-free controls.

*In all of the studies cited above, the dependence of mechanical strength on nanoparticle loading showed a peak at a specific nanoparticle concentration. This observed nonlinear dependence of mechanical strength on nanoparticle loading points to the importance of understanding the effects of nanoparticle incorporation on the mechanisms of membrane formation and membrane performance, in order to allow for an optimized design of mechanically robust nanocomposites.*

### **Tunable hydrophilicity**

The most common component of natural waters is highly hydrophobic organic matter. A straightforward approach to reduce membrane fouling due to deposition of organic matter on the membrane surface is therefore to reduce the affinity between the membrane material and the foulants. This can be attained by increasing the hydrophilicity of the membrane material, thus decreasing its propensity to adsorb hydrophobic organics from the feed stream.

*The integration of nanoparticles and polymeric materials is an emerging approach to modify the physico-chemical properties of the host polymer matrix.* Incorporating nanoparticles into the bulk polymer, as opposed the traditional strategy of applying chemical pre-treatments or chemically active surface coatings offers the advantage of minimizing the environmental footprint of the hybrid composite by reducing the risk of release of toxic compounds derived from chemical treatments. An additional advantage of nanoparticle inclusions vs. chemical coatings is the increased durability of the

incorporated feature, as it becomes part of the bulk material, rather than simply a surface feature, more prone to be removed under flow through conditions.

Few studies addressed the effect of incorporated particles on the hydrophilicity of resulting nanocomposite membranes. Polysulfone-clay phase inversion composite membranes showed a 25% higher hydrophilicity when compared to clay free membranes [21]. Increasing loadings of alumina ( $\text{Al}_2\text{O}_3$ ) nanoparticles in phase inversion PVDF membranes were correlated with an increase in hydrophilicity of the modified membranes [15], while incorporation of titanium ( $\text{TiO}_2$ ) nanoparticles to phase inversion PSf [19] and PPESK [22] membranes showed hydrophilicity enhancements of above 40% in both cases.

Given that the surface area of nanoparticles is related to the nanoparticle size, one can expect significant hydrophilic enhancements as the size of hydrophilic nano inclusions is reduced, at equal loadings. Furthermore, similar hydrophilic enhancements to those observed for higher nanoparticle loadings or micro-scaled particles could be attained with lower loadings of smaller sized nanoparticles; thus allowing for further optimization and cost reduction strategies.

*In light of the potential use of hydrophilic nanoparticles as membrane fillers for the mitigation of membrane fouling, it is important to study the effect of nanoparticle loading and size on the performance of nanoparticle-filled membranes.*

## **Adaptive membranes**

*A relevant example of membranes with a dynamic function is stimuli-responsive (or adaptive) membranes that can reversibly adjust their permeability or rejection in response to external stimuli [3, 35-52].*

In recent years, numerous studies have focused on the development a new generation of magnetically responsive dense polymer nanocomposites, or magneto-elastomers, obtained when magnetically active nanoscale inclusions are embedded into an elastic polymeric matrix. The ability of such composites to reversibly change their structural and mechanical properties as they are subject to an external magnetic field, is raising considerable attention towards various applications including “smart” actuators, dampers and artificial muscles, among others [53-55].

An appealing aspect of the phase inversion approach relies in the additional possibilities for the tailored design of nanocomposite membranes and the coupling between their hydraulic and mechanical properties and the nanoparticles reactivity to external stimuli. Magnetically susceptible nanoparticles are of particular interest for the development of such reactive, or adaptive, porous nanocomposites. The introduction of magnetically active nanoparticles to the matrix of a polymeric membrane could allow for the possibility of externally controlling, via application of a magnetic field, the structural morphology and consequently the hydraulic properties of the nanostructured membranes.

Nanoparticle loading, size and morphology should all be expected to affect the degree of susceptibility of the nano-structured composite to the external stimuli. Supra-magnetic properties of nanoparticles are enabled and dictated by their size, as they are intrinsically a surface-based effect. As reported by Thapa et al. [56], the enhancement of saturation magnetization in magnetite nanoparticles was strongly size dependent, increasing at lower particle diameters, but reaching a size threshold beyond which a sudden drop in magnetization was observed.

Additionally, nanoparticle aspect ratio (e.g. nano-rods vs. nano-spheres) is expected to be of critical relevance for the development of mechanically adaptive nanocomposites, allowing for the anisotropic alignment of nano-inclusions within the polymeric matrix, to achieve direction dependant enhancements of mechanical properties. Thostenson et al. [57] compared the tensile behavior of polystyrene films doped with aligned (via extrusion) carbon nanotubes, with respect to non-aligned nanotube filled polystyrene films. Nanotube alignment resulted in a significant improvement in the elastic modulus of the composites, as compared to randomly oriented nanotube-polystyrene films. In a later work, Camponeschia et al. [58] showed that the mechanical properties (glass transition temperature, Young's modulus and elastic and viscous moduli) of carbon nanotube doped epoxy composites could be altered upon exposure to an external magnetic field. Furthermore, upon magnetic alignment, the composites showed enhancements in their mechanical properties that were not observed for non-aligned composites.

*The above findings point to promising research opportunities involving the development of magnetically adaptive porous nanocomposites, and stress the importance of studying the interplay between nanoparticle loading, size and morphology and the performance of nanoparticle-filled composites.*

## **Dissertation Overview**

This work explores various aspects of the fabrication of nanoparticle-enabled membranes and its potential environmental applications. As follows, a brief summary of each chapter is offered.

Chapter 1 is introductory. It offers a theoretical background covering the thermodynamic and kinetic principles that govern the wet phase inversion process, which is one of the synthetic methods used to fabricate polymeric membranes (see Chapters 2 and 3.)

Chapter 2 focuses on the effect of nanoparticle shape and loading on the hydraulic resistance and rejection of polysulfone membranes filled with two types of carbon nanoparticles: Fullerenes (nanospheres) and Single-walled carbon nanotubes (nanorods). The rate of precipitation front advancement and viscosity of the casting mixtures are found to correlate with the permeability and rejection of cast nanocomposite membranes. These correlations are rationalized in terms of the effect of nanoparticle fillers on the demixing and gelation processes occurring during phase inversion. The propagation rate of the precipitation front and the viscosity of the casting mixture are proposed as simple-to-measure predictors of membrane performance with potential application for the rational design of porous nanocomposites.

Chapter 3 describes the synthesis of flat sheet porous polysulfone-silver nanocomposite membranes by the wet phase inversion process. In particular, the effects of casting

mixture composition and nanoparticle incorporation route on the morphological and separation properties of the prepared membranes. Furthermore, the built-in antibacterial capacity due to the gradual release of ionic silver by the prepared nanocomposites was found to be effective in reducing intrapore biofouling. Such nanocomposites could in principle be used as materials for macroporous membrane spacers to inhibit the biofilm growth on downstream membrane surfaces.

Finally, Chapter 4 presents a method for the synthesis of a nanoparticle-enabled, membrane-based sensor. Silver nanoparticle arrays are deposited on the surface of polycarbonate track etch membranes. The nanoparticle-modified membranes are characterized in terms of their hydraulic and optical properties and evaluated as flow-through surface-enhanced Raman scattering (SERS) sensors for water quality monitoring. The membrane-supported nanoparticle arrays were found to be SERS-active with slightly lower but significantly more reproducible enhancements in comparison with enhancements afforded by source nanoparticle suspensions. The findings point to the promise of combining high specification SERS-active systems and the flow-through design for the development of membrane based analytical sensors for the trace detection of aqueous pollutants.

## References

1. W. Liu, Nanoparticles and their biological and environmental applications, *J. Biosci. Bioeng.* 102 (2006) 1-7.
2. F. E. Kruis, H. Fissan and A. Peled, Synthesis of nanoparticles in the gas phase for electronic, optical and magnetic applications--a review, *J. Aerosol Sci.* 29 (1998) 511-535.
3. B. Adhikari and S. Majumdar, Polymers in sensor applications, *Prog. Polym. Sci.* 29 (2004) 699-766.
4. P. Vadgama, Membrane based sensors: A review, *J. Membr. Sci.* 50 (1990) 141-152.
5. D. G. Yu, M. Y. Teng, W. L. Chou and M. C. Yang, Characterization and inhibitory effect of antibacterial PAN-based hollow fiber loaded with silver nitrate, *J. Membr. Sci.* 225 (2003) 115.
6. W. L. Chou, D. G. Yu and M. C. Yang, The preparation and characterization of silver-loading cellulose acetate hollow fiber membrane for water treatment, *Polym. Adv. Technol.* 16 (2005) 600 - 607.
7. R. Bhattacharya, T. N. Phaniraj and D. Shailaja, Polysulfone and polyvinyl pyrrolidone blend membranes with reverse phase morphology as controlled release systems: experimental and theoretical studies, *J. Membr. Sci.* 227 (2003) 23.
8. R. E Kesting, *Synthetic Polymeric Membranes, A Structural Perspective*. Second ed. 1985, New York: John Wiley & Sons.
9. M. Mulder, *Basic Principles of Membrane Technology*. Second ed. 2003, Dordrecht, Netherlands: Kluwer Academic.
10. A. Bottino, G. Capannelli and A. Comite, Preparation and characterization of novel porous PVDF-ZrO<sub>2</sub> composite membranes, *Desalination* 146 (2002) 35-40.
11. P. Aerts, I. Genne, S. Kuypers, R. Leysen, I. F. J. Vankelecom and P. A. Jacobs, Polysulfone-aerosil composite membranes: Part 2. The influence of the addition of aerosil on the skin characteristics and membrane properties, *J. Membr. Sci.* 178 (2000) 1-11.
12. P. Aerts, E. Van Hoof, R. Leysen, I. F. J. Vankelecom and P. A. Jacobs, Polysulfone-aerosil composite membranes: Part 1. The influence of the addition of Aerosil on the formation process and membrane morphology, *J. Membr. Sci.* 176 (2000) 63-73.

13. N. M. Wara, L. F. Francis and B. V. Velamakanni, Addition of alumina to cellulose acetate membranes, *J. Membr. Sci.* 104 (1995) 43-49.
14. I. Genne, S. Kuypers and R. Leysen, Effect of the addition of ZrO<sub>2</sub> to polysulfone based UF membranes, *J. Membr. Sci.* 113 (1996) 343-350.
15. L. Yan, Y. S. Li, C. B. Xiang and S. Xianda, Effect of nano-sized Al<sub>2</sub>O<sub>3</sub>-particle addition on PVDF ultrafiltration membrane performance, *J. Membr. Sci.* 276 (2006) 162-167.
16. K. Ebert, D. Fritsch, J. Koll and C. Tjahjaviguna, Influence of inorganic fillers on the compaction behaviour of porous polymer based membranes, *J. Membr. Sci.* 233 (2004) 71-78.
17. D. G. Yu, M. Y. Teng, W. L. Chou and M. C. Yang, Characterization and inhibitory effect of antibacterial PAN-based hollow fiber loaded with silver nitrate, *J. Membr. Sci.* 225 (2003) 115-123.
18. X. He, Q. Shi, X. Zhou, C. Wan and C. Jiang, In situ composite of nano SiO<sub>2</sub>-P(VDF-HFP) porous polymer electrolytes for Li-ion batteries, *Electrochim. Acta* 51 (2005) 1069-1075.
19. Y. Yang, H. Zhang, P. Wang, Q. Zheng and J. Li, The influence of nano-sized TiO<sub>2</sub> fillers on the morphologies and properties of PSF UF membrane, *J. Membr. Sci.* 288 (2007) 231-238.
20. W. K. Son, J. H. Youk, T. S. Lee and W. H. Park, Preparation of antimicrobial ultrafine cellulose acetate fibers with silver nanoparticles, *Macromol. Rapid Commun.* 25 (2004) 1632-1637.
21. O. Monticelli, A. Bottino, I. Scandale, G. Capannelli and S. Russo, Preparation and properties of polysulfone-clay composite membranes, *J. Appl. Polym. Sci.* 103 (2007) 3637-3644.
22. J. B. Li, J. W. Zhu and M. S. Zheng, Morphologies and properties of poly(phthalazinone ether sulfone ketone) matrix ultrafiltration membranes with entrapped TiO<sub>2</sub> nanoparticles, *J. Appl. Polym. Sci.* 103 (2006) 3623-3629.
23. A. Bottino, G. Capannelli, V. D'Asti and P. Piaggio, Preparation and properties of novel organic-inorganic porous membranes, *Sep. Purif. Technol.* 22-23 (2001) 269-275.
24. L. Ballinas, C. Torras, V. Fierro and R. Garcia-Valls, Factors influencing activated carbon-polymeric composite membrane structure and performance, *J. Phys. Chem. Solids* 65 (2004) 633-637.

25. J.-H. Choi, J. Jegal and W.-N. Kim, Fabrication and characterization of multi-walled carbon nanotubes/polymer blend membranes, *J. Membr. Sci.* 284 (2006) 406-415.
26. K. M. Persson, V. Gekas and G. Tragardh, Study of membrane compaction and its influence on ultrafiltration water permeability, *J. Membr. Sci.* 100 (1995) 155-162.
27. G. Jonsson, Methods for determining the selectivity of reverse osmosis membranes, *Desalination* 24 (1977) 19-37.
28. R. Kotsilkova, D. Fragiadakis and P. Pissis, Reinforcement effect of carbon nanofillers in an epoxy resin system: Rheology, molecular dynamics, and mechanical studies, *J. Polym. Sci. Pol. Phys.* 43 (2005) 522-533.
29. A. Zhu, A. Cai, J. Zhang, H. Jia and J. Wang, PMMA-grafted-silica/PVC nanocomposites: Mechanical performance and barrier properties, *J. Appl. Polym. Sci.* 108 (2008) 2189-2196.
30. M. Q. Zhang, M. Z. Rong, H. B. Zhang and K. Friedrich, Mechanical properties of low nano-silica filled high density polyethylene composites, *Polym. Eng. Sci.* 43 (2003) 490-500.
31. J. N. Coleman, U. Khan and Y. K. Gun'ko, Mechanical reinforcement of polymers using carbon nanotubes, *Adv. Mater.* 18 (2006) 689-706.
32. M. I. Sarwar, S. Zulfiqar and Z. Ahmad, Polyamide-silica nanocomposites: mechanical, morphological and thermomechanical investigations, *Polym. Int.* 57 (2008) 292-296.
33. K. Yang, Q. Yang, G. Li, Y. Sun and D. Feng, Mechanical properties and morphologies of polypropylene with different sizes of calcium carbonate particles, *Polym. Compos.* 27 (2006) 443-450.
34. S. P. Nunes, K. V. Peinemann, K. Ohlrogge, A. Alpers, M. Keller and A. T. N. Pires, Membranes of poly(ether imide) and nanodispersed silica, *J. Membr. Sci.* 157 (1999) 219-226.
35. Y. Wang, Z. Liu, B. Han, Z. Dong, J. Wang, D. Sun, Y. Huang and G. Chen, pH Sensitive polypropylene porous membrane prepared by grafting acrylic acid in supercritical carbon dioxide, *Polymer* 45 (2004) 855-860.
36. N. Minoura, K. Idei, A. Rachkov, Y. W. Choi, M. Ogiso and K. Matsuda, Preparation of azobenzene-containing polymer membranes that function in photoregulated molecular recognition, *Macromolecules* 37 (2004) 9571-9576.

37. S. Petrov, T. Ivanova, D. Christova and S. Ivanova, Modification of polyacrylonitrile membranes with temperature sensitive poly(vinylalcohol-co-vinylacetal), *J. Membr. Sci.* 261 (2005) 1-6.
38. W. Lequeieu, N. I. Shtanko and F. E. Du Prez, Track etched membranes with thermo-adjustable porosity and separation properties by surface immobilization of poly(N-vinylcaprolactam), *J. Membr. Sci.* 256 (2005) 64-71.
39. N. I. Shtanko, V. Ya Kabanov, P. Yu Apel, M. Yoshida and A. I. Vilenskii, Preparation of permeability-controlled track membranes on the basis of 'smart' polymers, *J. Membr. Sci.* 179 (2000) 155-161.
40. L. Liang, X. Feng, L. Peurrung and V. Viswanathan, Temperature-sensitive membranes prepared by UV photopolymerization of N-isopropylacrylamide on a surface of porous hydrophilic polypropylene membranes, *J. Membr. Sci.* 162 (1999) 235-246.
41. J. F. Hester, S. C. Olugebefola and A. M. Mayes, Preparation of pH-responsive polymer membranes by self-organization, *J. Membr. Sci.* 208 (2002) 375-388.
42. A. Kumar, A. Srivastava, I. Y. Galaev and B. Mattiasson, Smart polymers: Physical forms and bioengineering applications, *Prog. Polym. Sci.* 32 (2007) 1205-1237.
43. T. Peng and Y. L. Cheng, pH-responsive permeability of PE-g-PMAA membranes, *J. Appl. Polym. Sci.* 76 (2000) 778-786.
44. L. Ying, P. Wang, E. T. Kang and K. G. Neoh, Synthesis and characterization of poly(acrylic acid)-graft-poly(vinylidene fluoride) copolymers and pH-sensitive membranes, *Macromolecules* 35 (2002) 673 -679.
45. H. Iwata, I. Hirata and Y. Ikada, Atomic force microscopic analysis of a porous membrane with pH-sensitive molecular valves, *Macromolecules* 31 (1998) 3671 - 3678.
46. H. Iwata, M. Oodate, Y. Uyama, H. Amemiya and Y. Ikada, Preparation of temperature-sensitive membranes by graft polymerization onto a porous membrane, *J. Membr. Sci.* 55 (1991) 119-130.
47. W. Y. Wang, L. Chen and X. Yu, Preparation of temperature sensitive poly(vinylidene fluoride) hollow fiber membranes grafted with N-isopropylacrylamide by a novel approach, *J. Appl. Polym. Sci.* 101 (2006) 833-837.
48. L. Y. Chu, T. Niitsuma, T. Yamaguchi and S. Nakao, Thermoresponsive transport through porous membranes with grafted PNIPAM gates, *AIChE J.* 49 (2003) 896-909.

49. X. Liu, K. G. Neoh and E. T. Kang, Redox-sensitive microporous membranes prepared from poly(vinylidene fluoride) grafted with viologen-containing polymer side chains, *Macromolecules* 36 (2003) 8361 -8367.
50. Y. Ito, S. Nishi, Y. S. Park and Y. Imanishi, Oxidoreduction-sensitive control of water permeation through a polymer brushes-grafted porous membrane, *Macromolecules* 30 (1997) 5856 -5859.
51. S.A. Piletsky, T.L. Panasyuk, E.V. Piletskaya, A.V. El'skaya, R. Levi, I. Karube and G. Wulff, Imprinted membranes for sensor technology: Opposite behavior of covalently and noncovalently imprinted membranes, *Macromolecules* 31 (1998) 2137-2140.
52. T. Yamaguchi, T. Ito, T. Sato, T. Shinbo and S. Nakao, Development of a fast response molecular recognition ion gating membrane, *JACS* 121 (1999) 4078-4079.
53. G. Filipcsei, I. Csetneki, A. Szilagyi and M. Zrinyi, Magnetic field-responsive smart polymer composites, in *Oligomers Polymer Composites Molecular Imprinting*. 2007. p. 137-189.
54. I. Park, K. J. Kim, J. Nam, J. Lee and W. Yim, Mechanical, dielectric, and magnetic properties of the silicone elastomer with multi-walled carbon nanotubes as a nanofiller, *Polym. Eng. Sci.* 47 (2007) 1396-1405.
55. Z. Varga, G. Filipcsei, A. Szilágyi and M. Zrínyi, Electric and Magnetic Field-Structured Smart Composites, *Macromol. Symp.* 227 (2005) 123-134.
56. D. Thapa, V. R. Palkar, M. B. Kurup and S. K. Malik, Properties of magnetite nanoparticles synthesized through a novel chemical route, *Materials Letters* 58 (2004) 2692-2694.
57. E. T. Thostenson and T. W. Chou, Aligned multi-walled carbon nanotube-reinforced composites: processing and mechanical characterization, *Journal Of Physics D-Applied Physics* 35 (2002) L77-L80.
58. E. Camponeschi, R. Vance, M. Al-Haik, H. Garmestani and R. Tannenbaum, Properties of carbon nanotube-polymer composites aligned in a magnetic field, *Carbon* 45 (2007) 2037-2046.

# **CHAPTER ONE**

## **Theoretical background of the phase inversion process**

This chapter provides a comprehensive theoretical framework regarding the basic principles that govern the wet phase inversion process; as this is the synthetic method used to fabricate the porous polymeric matrices in the work detailed in Chapters Two and Three.

### **1.1. Phase Inversion**

The vast majority of both dense and porous commercially available polymeric membranes, as well as the porous supports of composite membranes, are produced by the phase-inversion process [1-3].

The phase inversion process was first applied in the 1960s, when Loeb and Sourirajan [4] developed the method to prepare asymmetric, integrally skinned, dense reverse osmosis membranes. The development of polymeric asymmetric membranes constituted a turning point towards overcoming a fundamental barrier for the extensive application of membranes; the achievement of simultaneous high selectivities and permeation fluxes. Such breakthrough is now recognized as the milestone that gave rise to the expansion of membrane technologies, and ultimately led to the widespread commercial application of

membranes. Later, in 1971, Michaels [5] adapted the method to produce ultrafiltration membranes using a variety of commercial polymers.

In the phase inversion process, a viscous polymer solution is cast into a thin film or a hollow fiber, and immersed into a homogeneous phase (non solvent) which has a high affinity for the polymer solvent, but low or no affinity for the polymer. As both phases are brought into contact, a mass transfer process is initiated as solvent and non solvent are exchanged, eventually resulting in the precipitation of a solid porous polymeric matrix that constitutes the membrane.

The described “demixing” of the polymer solution can be brought about using a variety of strategies that give rise to different phase inversion alternatives.

When the immersion phase is the atmosphere, or dry phase inversion, the polymer precipitates as the solvent evaporates from the polymer solution and/or a non solvent (dissolved in the gas phase) slowly diffuses into the viscous film.

Phase inversion can also be induced by using a latent polymer solvent; which is a solution component that behaves as a solvent at high temperatures, but becomes the non solvent as temperature decreases; such is the underlying principle of the thermally induced phase inversion process.

Finally, when the immersion medium is a non solvent liquid, the process is known as wet phase inversion. This process can be as well preceded by a brief solvent evaporation stage (dry-wet phase inversion). The wet phase inversion process is the preferred method for the synthesis of porous membranes; for this reason, further analyses will be focused on the basic principles of wet phase inversion and the effect of different process parameters on the morphological features of the cast membranes.

The following sections offer a detailed qualitative description of the basic concepts and fundamental thermodynamic and kinetic principles affecting membrane formation during wet phase inversion. The understanding of such principles is of critical importance as they dictate the membrane's final structural morphology, and thus have a critical impact on its performance and viability.

## **1.2.Liquid-Liquid Demixing**

In all phase inversion methods, the process starts with a thermodynamically stable polymer solution, or casting mixture. For illustrative simplicity, the solution will be composed solely of polymer and solvent. It must be noted though that in many cases three or four solution components are used, incorporating additional pore forming agents or a small fraction of non solvent into the casting mixture.

For a binary (polymer/solvent) system, the free energy of mixing ( $\Delta G_m$ ), as derived from the Flory-Huggins theory [6], is given by:

$$\frac{\Delta G_m}{RT} = n_1 \ln \phi_1 + n_2 \ln \phi_2 + n_1 \phi_2 \chi$$

Where,  $n_1$  and  $n_2$  represent the total moles of solvent and polymer in the mixture, respectively;  $\phi_1$  and  $\phi_2$  are the volume fractions of solvent and polymer in the mixture and  $\chi$  is the Flory-Huggins solvent-polymer interaction parameter, which encompasses all excess enthalpic contributions due to the non ideal behavior of the solution constituents.

The variation in chemical potential ( $\Delta\mu$ ) for each component upon mixing can be obtained as:

$$\Delta\mu_i = \mu_i - \mu_i^0 = \left. \frac{\partial \Delta G_m}{\partial \mu_i} \right|_{T,P,n_j}$$

Where  $\mu_0$  represents the chemical potential of the pure component.

For a given overall solvent/polymer ratio, at a given temperature, the two components will tend to minimize their respective  $\Delta\mu$ . Such tendency can be better visualized by analyzing a polymer solution that is subject to progressive cooling.

At a sufficiently high temperature ( $T_4$ ), the two components will tend to mix at any relative composition. This is illustrated in Figure 1.1.

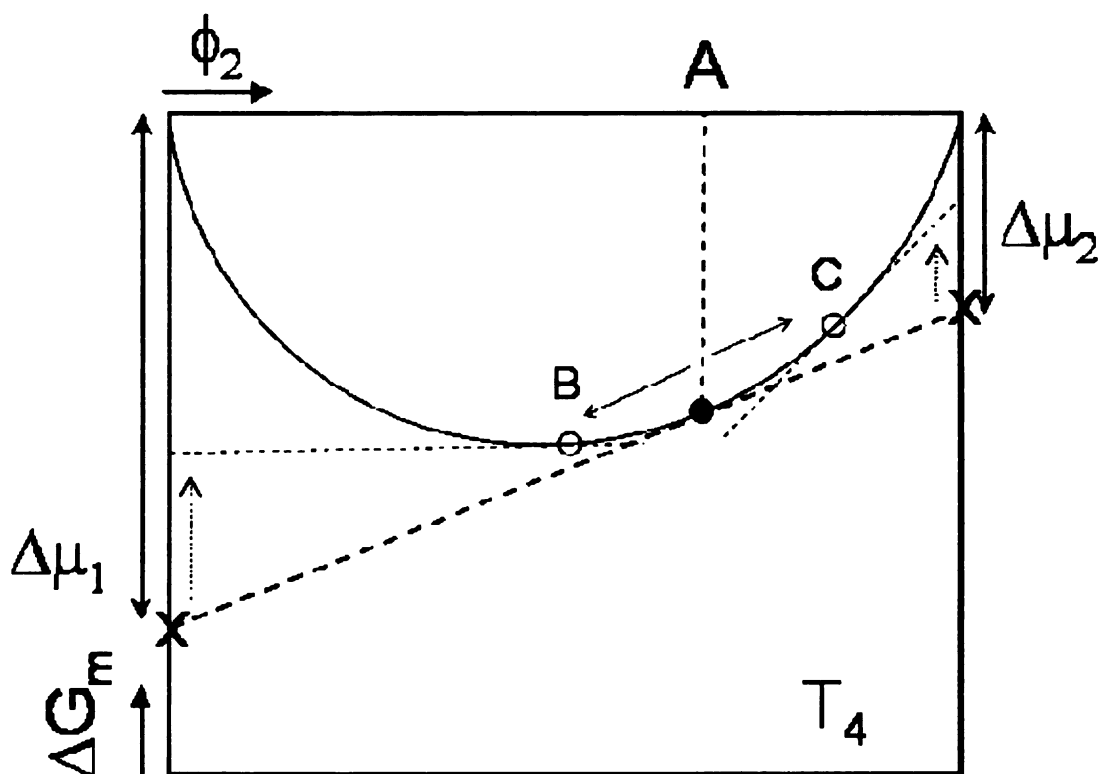


**Figure 1.1.** Plot of  $\Delta G_m$  vs.  $\phi_2$  for the polymer/solvent system at temperature  $T_4$ , above the critical point.

At an arbitrary composition A, both components are completely mixed. The variation in the chemical potential for each component upon mixing, with respect to each component in its pure (non-mixed) state ( $\Delta\mu_1$  and  $\Delta\mu_2$ ) can be obtained from the intersections of the tangent to the  $\Delta G_m$  curve (at composition A) with each of the pure component axes.

As can be seen on Fig. 1.1, both  $\Delta\mu_1$  and  $\Delta\mu_2$  are negative, indicating a decrease in the chemical potentials for both components upon mixing, and thus a favorable mixing tendency.

Let us now consider a hypothetical demixing process, by which the two components separate from each other to form two separate phases, each of which is predominantly concentrated in one of the components (points B and C). For such demixing to occur, component 1 has to be transferred from the original mixture (A) to the new, component 1 rich, phase B. However, as can be seen from the graph, this transference process would result in a tangent (at point B) line that would produce an increase (with respect to point A) in the chemical potential for component 1. A similar analysis can be done for the formation of phase C, in this case, this would result in an increase in the chemical potential for component 2 (point C). The chemical potential increase for each component is shown by the dotted arrows. Consequently, the demixing process is thermodynamically unfavorable (the components tend to decrease their chemical potentials and thus the free energy of the system), and the two components will remain completely mixed with composition A.

The situation, however, changes when temperature is decreased. Below a given temperature - or Critical Temperature ( $T_c$ ) - which is specific to the studied component pair; the  $\Delta G_m$  curve starts eliciting two inflection points ( $A'_1$  and  $A'_2$ ), as shown in Figure 1.2.

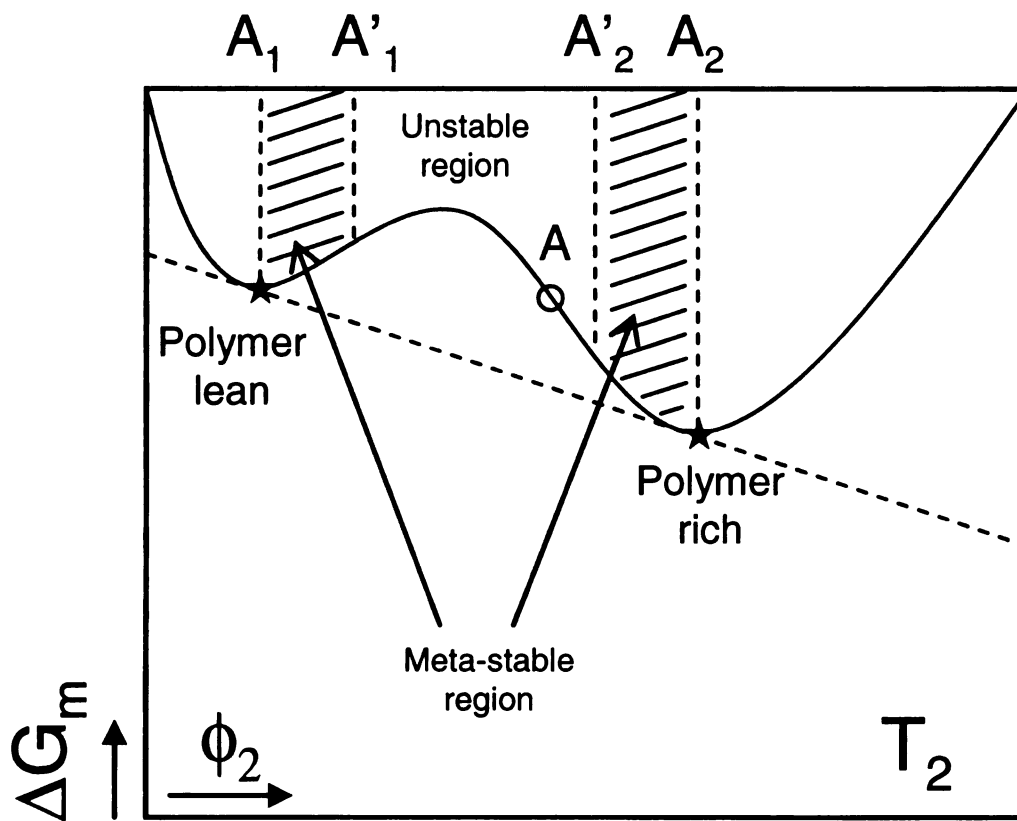


**Figure 1.2.** Polymer/solvent system's  $\Delta G_m$  vs.  $\phi_2$  plot at a temperature  $T_2$  below the critical point

The intersection of the tangent to the curve (at point A) with the pure component 1 axis now yields a positive  $\Delta\mu_1$ . The original mixture of composition A (Fig. 1.1), stable at  $T_4$ , now lies in a thermodynamically unstable region and the mixture will thus tend to demix. The system will demix by “pulling” the two components apart, forming two separate phases, each of which will be relatively richer in one of the components. By doing so, the system separates into two liquid phases, until a new equilibrium state of minimum free energy is reached. This process is known as Liquid-Liquid (L-L) demixing.

From unstable composition A, the two components will tend to reduce their respective chemical potentials, by moving along the  $\Delta G_m$  curve towards curve points where their chemical potentials are reduced with respect to those in initial point A, in other words, along points where  $\delta\Delta\mu_i/\delta\phi < 0$ . This negative chemical potential variation region will occur between points A and  $A'_1$  for component 1 (solvent) and between points A and  $A'_2$  for component 2 (polymer). For this reason, this region is called the demixing or unstable region, and any mixture inside this region will spontaneously experience L-L demixing, compositions  $A'_1$  and  $A'_2$  are called the spinodal points. As demixing unfolds, component 1 will move towards point  $A'_1$  and component 2 will do so towards  $A'_2$ , thereby progressively forming two separate phases enriched in either component 1 ( $A'_1$ ) or component 2 ( $A'_2$ ). The demixing process will continue until the two phases reach equilibrium with each other, or in thermodynamical terms, until the overall variation in chemical potentials for each component is the same in both phases. This final state is shown in figure 1.2: Points  $A_1$  and  $A_2$ ; that share a common tangent, indicating they have

reached the same final chemical potentials in the  $\Delta G_m$  curve. These two compositions ( $A_1$  and  $A_2$ ) are known as the binodal compositions. The common tangent line connecting the binodal points is known as a tie line.

As the two components demix and separate, two distinct phases are formed. We will now focus the analysis on the path followed by the polymer (component 2) molecules.

As demixing unfolds, the solvent molecules will progressively “de-solve” the polymer molecules. As solvent and polymer molecules separate, a finely interconnected network of polymer lean and polymer rich regions are created. This process is known as spinodal demixing, and will continue as long as there is a driving force for spontaneous demixing, that is,  $\delta\Delta\mu_2/\delta\phi < 0$ . Eventually,  $\delta\Delta\mu_2/\delta\phi$  becomes zero at inflexion –spinodal- point  $A'_2$ , and there is thus no longer a driving force for the spontaneous separation of polymer from the solvent within the system. However, the solvent has not yet reached its spinodal point ( $A'_1$ ); this creates a thermodynamically meta-stable region (from  $A'_2$  to  $A_2$ ). Within this region, the polymer rich phase will remain stable for small compositional fluctuations in the surrounding system (since  $\delta\Delta\mu_2/\delta\phi \geq 0$ ). Simultaneously, component 1 (the solvent) is following a parallel trend as it moves towards the opposite end of the  $G_m$  curve, forming the polymer lean (or solvent rich) phase  $A_1$ , and thus continuously “releasing” solvent to the system. These “free” solvent molecules will initially become part of the polymer lean phase during spinodal demixing, however, when the polymer rich phase has reached its meta-stable region, new solvent molecules will start forming

isolated nuclei within the continuous polymer rich phase. As the solvent molecules separate from the polymer molecules to form the polymer lean phase, these freed polymer molecules will create a thermodynamical pressure against the polymer rich phase, which is now in its meta-stable state. The polymer molecules will be gradually incorporated to the meta-stable polymer rich phase, “pushing” its composition towards stable binodal point  $A_2$ . What was originally an interconnected network of two coexisting phases during spinodal demixing, now becomes a distinctly separated system of growing nuclei of polymer lean phase within a “sea” of polymer rich phase. This distinct demixing process occurring within the meta-stable region, by which the system equilibrates itself via formation and growth of polymer lean nuclei of composition  $A_1$  within the polymer rich phase, is called demixing by nucleation and growth. In parallel, and analogously, the polymer lean phase evolves to its own stable composition  $A_1$ .

The preceding discussion focused on the formation of polymer lean phase nuclei within a polymer rich phase. However, the inverse process can also occur, that is, the formation of polymer rich blobs in a sea of solvent rich phase; what will determine the kind of nucleation and growth mechanism will be which of the two phases reach the spinodal point first. If the spinodal point is first reached by the polymer rich phase; then the solvent will constitute the forming nuclei, as described above, if instead the polymer lean phase reaches its spinodal point before the polymer rich phase, then polymer blobs will grow within the solvent rich phase.

Figure 1.3 shows the  $\Delta G_m$  curves for the polymer/solvent system at different temperatures. Below a critical temperature ( $T_c$ ), the  $\Delta G_m$  curves start showing spinodal and binodal points, the first spinodal/binodal pair coinciding in the critical point. By joining the binodal and spinodal points for each temperature; the binodal and spinodal curves for the system, as a function of temperature, are obtained. The miscibility gap is delimited by the binodal curve; any point lying inside the binodal curve will experience demixing, and will separate into two distinct phases (polymer lean and polymer rich) of equilibrium compositions given by the intersections between the tie lines and the binodal curve, at a given temperature. A mixture, stable at a high temperature, will enter the miscibility gap as it is subject to progressive cooling. If it enters the miscibility gap on the left side of the critical point, that is closer to the polymer lean spinodal points, then demixing will occur by nucleation and growth of the polymer rich phase (polymer blobs within a “sea” of polymer lean phase); the opposite nucleation and growth process (polymer lean nuclei growing in a polymer rich phase) will hold if the gap is entered on the right side of the critical point. Figure 1.3 (adapted from [7]) shows the starting stable point (A) of the described system at  $T_4$  and the endpoint binodal compositions of the separated equilibrium phases ( $A_1$  and  $A_2$ ) after cooling down the system to an arbitrary temperature  $T_1$ . In this case, demixing will occur by nucleation and growth of the polymer lean phase.

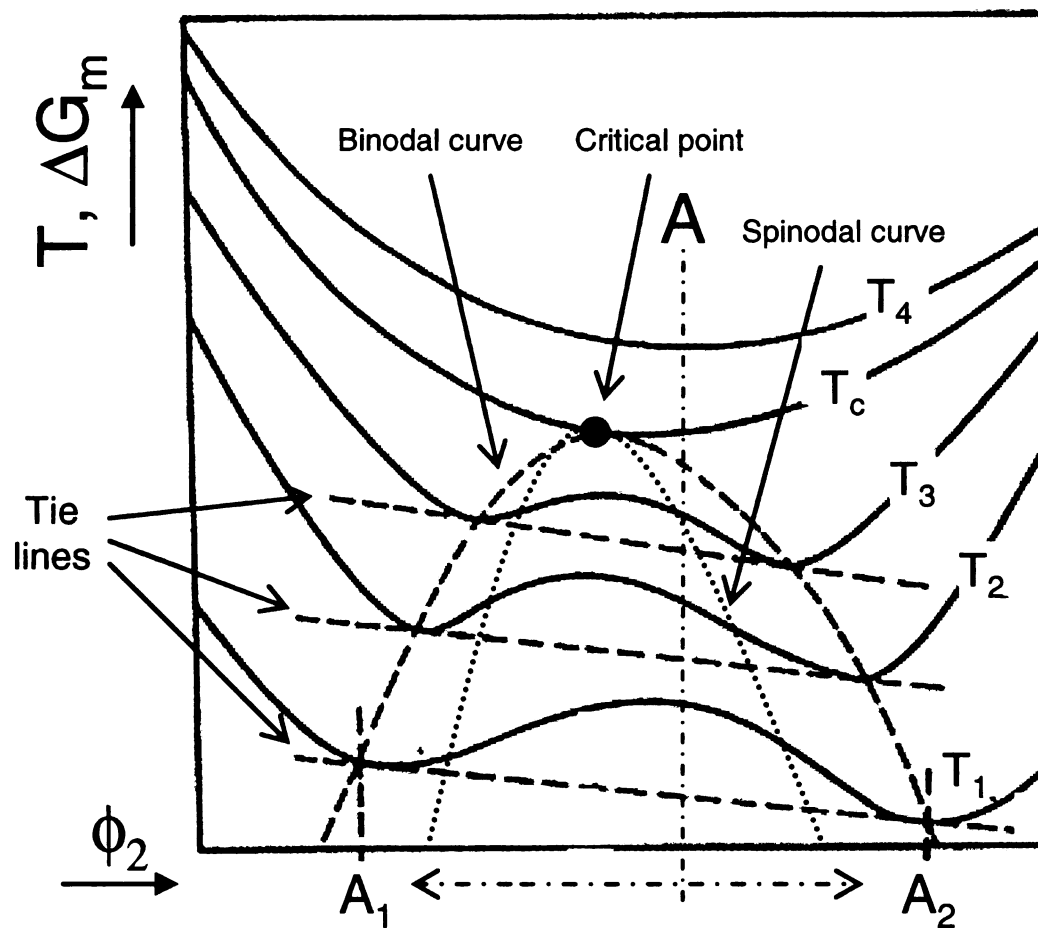


**Figure 1.3.**  $\Delta G_m$  vs.  $\phi_2$  curves for the polymer/solvent system at different temperatures, from the completely mixed system at  $T_4$ , above the critical temperature ( $T_c$ ), to  $T_1$ , final temperature of the demixed system.

### 1.3. Ternary system demixing

The offered thermodynamic analysis applies to the demixing of a polymer/solvent mixture as it is cooled down; wherein thermodynamic destabilization is induced by a temperature decrease. However, temperature decrease is not the only way to destabilize a polymer/solvent mixture. Demixing of the system can also be brought about by incorporating a third component into the system; a non-solvent. At a constant temperature, the progressive incorporation of non solvent to the system will have a similar destabilizing effect (and  $\Delta G_m$  curves deformation patterns) than that of progressive cooling for the polymer/solvent mixture. An equivalent analysis to the one offered for cooling induced demixing can be performed for non-solvent induced demixing. Analogously, binodal and spinodal curves can be obtained beyond a critical point, this time not as a function of decreasing temperature, but as a function of an increasing non-solvent concentration in the system.

In a three-component system (polymer, solvent and non solvent), the relative composition of each component in the system can be graphically represented using a ternary phase diagram (Fig. 1.4). Each vertex of the diagram represents the pure component (100 % relative concentration), while the triangle side that is opposite to each component vertex represents its respective zero concentration. For an arbitrary three-component mixture (star point in Fig.1.4), the relative concentration of each component in the system can be obtained by drawing a line parallel to the zero axis for that component. The relative position of the line between the pure component vertex and its respective zero axis will

represent its relative concentration within the system. This is exemplified and illustrated in Figure 1.4. For the example mixture the relative component concentrations are 15, 40 and 45% for non solvent, solvent and polymer, respectively.

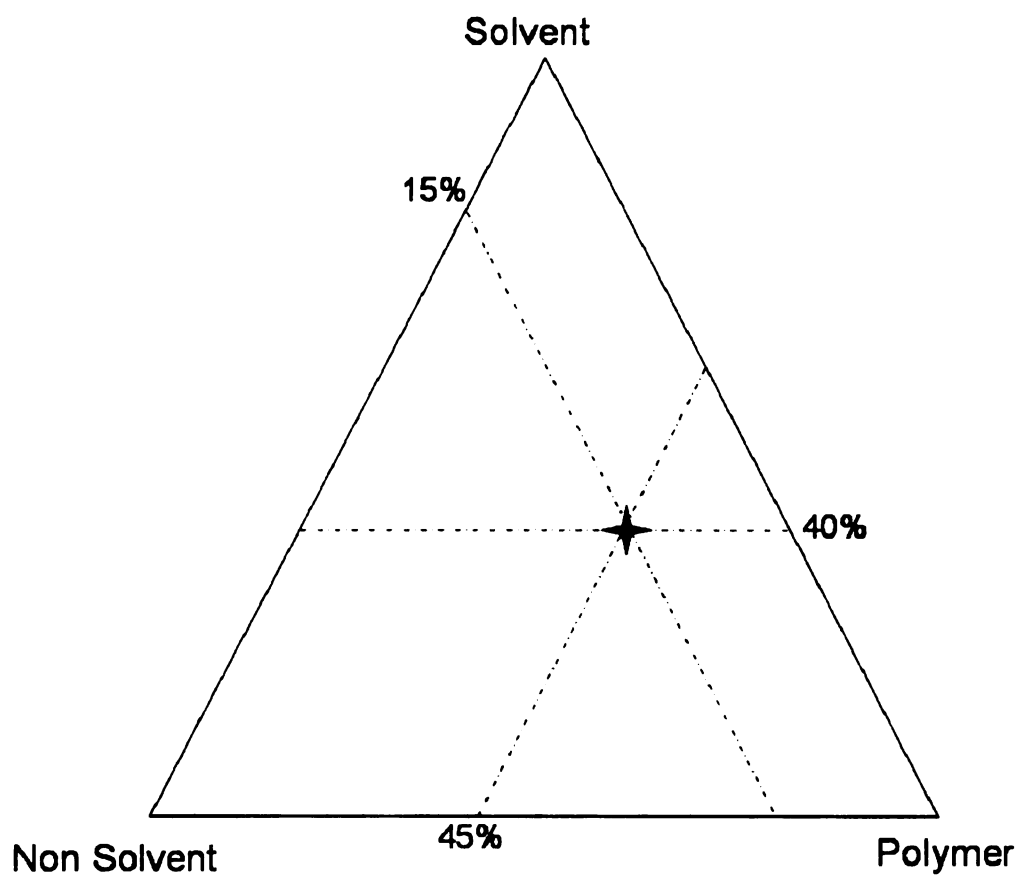


**Figure 1.4.** Ternary phase diagram of a three component system (solvent, non-solvent and polymer).

As explained before, an increase in non solvent concentration will result in the demixing of the system into two separate phases. The demixing region, or miscibility gap, can be schematically represented by the critical point, and binodal and spinodal curves. In this case, the critical point and demixing curves will appear as we move from the zero non solvent axis (polymer/solvent axis) towards the pure non solvent vertex, as shown in Fig.

1.5.

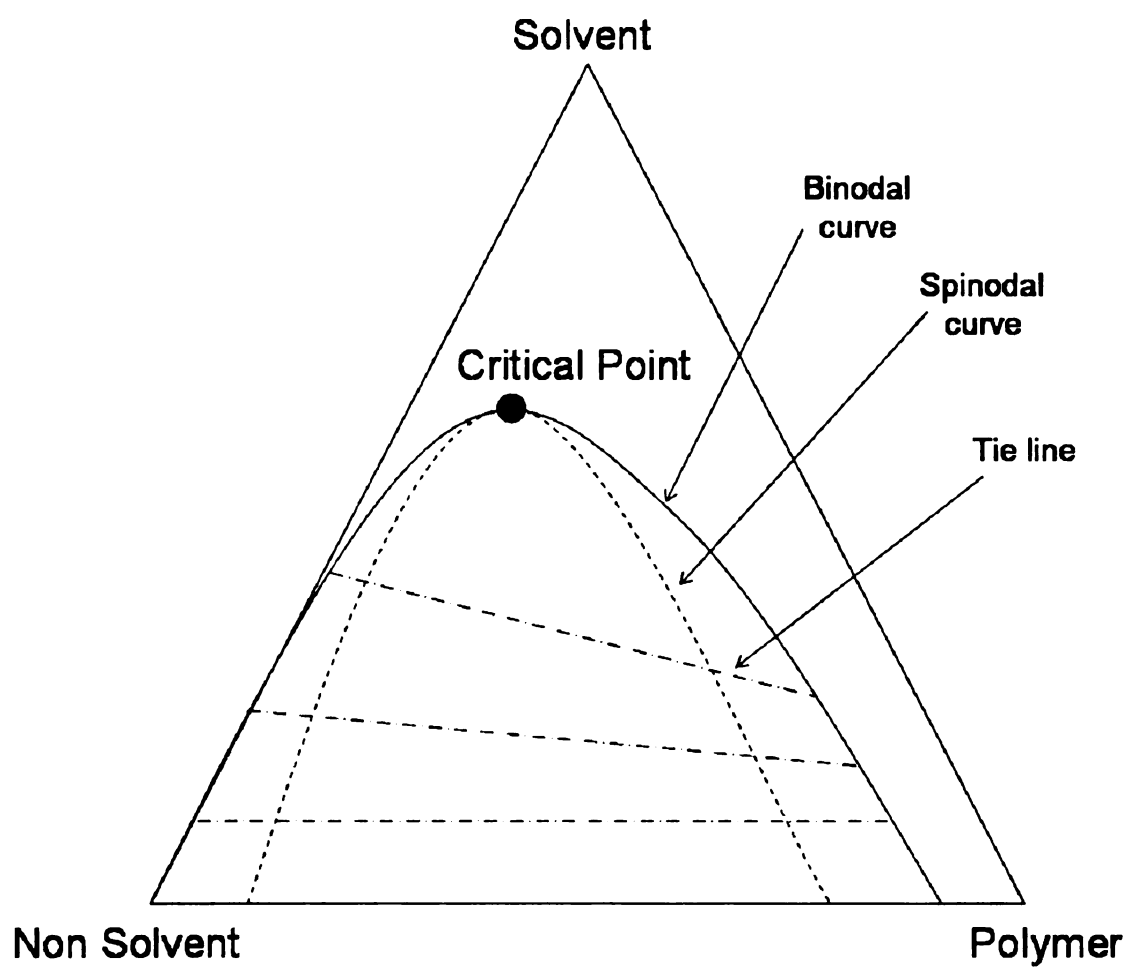


**Figure 1.5.** Solubility diagram for the three component system, showing the binodal and spinodal curves, tie lines, and the critical point.

A final consideration must be given to the solidification of the polymer network.

Depending on the arrangement of the polymer molecules in the solid state, polymers can be classified into three categories: Crystalline, with a regular and highly ordered molecular arrangement in the solid state; amorphous, with randomly packed molecules in no discernible order, and semi-crystalline, where both crystalline and amorphous regions coexist in the solid state. Since the polymer of choice for the present work – Polysulfone - is an amorphous polymer, the analysis will be focused on the solidification of this type of polymers.

The solid state for amorphous polymers can be visualized as a frozen (or “glassy”) state of their randomly oriented molecules, which can be brought about by cooling the system past a certain glass transition temperature ( $T_g$ ). Beyond the  $T_g$ , the mobility of the polymer chains is significantly reduced and the solid state is achieved. This solidification process is known as vitrification.

An additional solidification phenomenon of critical importance for membrane formation is gelation. Amorphous gelation is a physical transition which results in a highly elastic, solid three dimensional network, or gel. This transition can occur due to an increase in the viscosity of a homogeneous polymer/solvent solution beyond a fluidity threshold (at increasingly higher polymer concentrations); or by enhancing the formation of polymer-polymer hydrophobic bonds, reducing the mobility of the molecules to finally achieve the gelled state. The latter can be brought about by incorporation of non solvent to a ternary

system, and can induce gelation at a lower polymer concentration threshold than that needed for viscosity increase induced gelation in a binary mixture.

In a ternary system, gelation can occur at constant temperature, both due to breaching of the viscosity threshold as the concentration of the polymer within the polymer rich phase increases during demixing, and also due to non solvent induced enhancement of polymer chain interactions. Gelation will thus occur beyond a polymer concentration threshold within the studied ternary system, and is independent of the vitrification process. If the molecules are sufficiently immobilized, the gel will not experience molecular structural changes, while it may continue to lose liquid due to outward diffusion. Otherwise, and depending upon the degree of immobilization of the polymer chains, the forming gel can further shrink and contract its molecular structure as polymer molecules get entangled by formation of hydrophobic bonds, resulting in an increased compaction of polymer molecules and release of liquid within the gel matrix, in a process known as syneresis.

All of the above discussed processes are illustrated in Fig. 1.6. Note that the ternary diagram has been rotated for illustrative purposes.

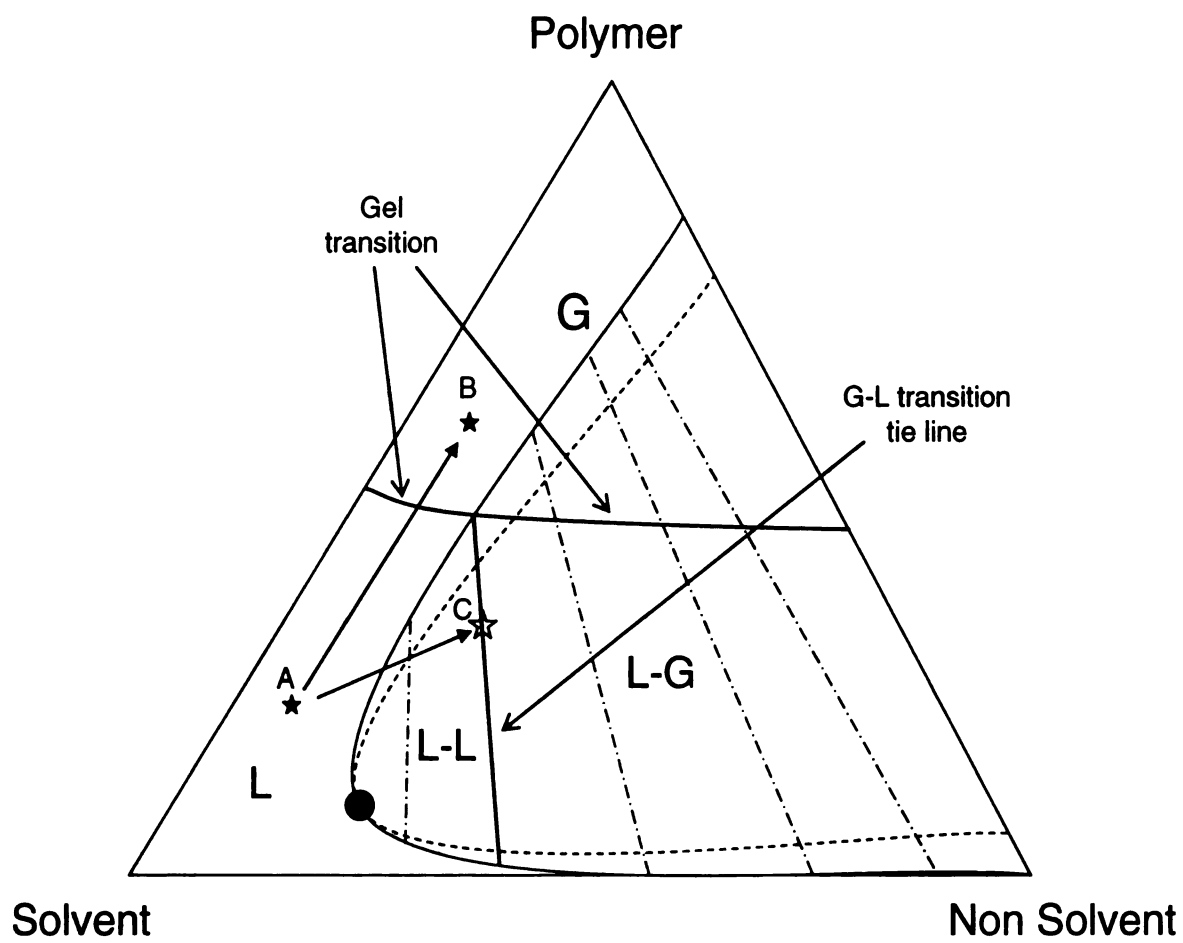


**Figure 1.6.**Demixing and gelation regions for the three component system.

The figure shows four distinct regions. A mixture point within each region will experience different thermodynamic states and thus demixing or solidification driving forces. Within the thermodynamically stable (liquid state) region for the three component mixture (L), delimited by the gel transition line and the binodal curve, all mixture components will be completely mixed forming a homogenous solution (A). As the polymer concentration in solution increases at constant non solvent concentration (path A-B); it will cross the gelation threshold (gel transition line) and enter the gelation region (G), encompassed beyond the gel transition line. The solution will then experience homogeneous gelation without a preceding liquid demixing step. Two other regions can be defined; both within the miscibility gap inside the binodal curve. These regions can be entered by increasing the non solvent content in the mixture, moving towards the non solvent/polymer axis (path A-C). The first region (L-L) involves the formation of two separate liquid phases due to liquid-liquid demixing. As explained in the previous section, if a mixture in the stable region (L) enters the miscibility gap below the critical point, and is able to reach the meta-stable region before gelling, demixing will occur by nucleation and growth of the polymer rich phase, while if it enters the gap above the critical point (path A-C), it will demix by nucleation and growth of the polymer lean phase. If gelation occurs before reaching the meta-stable region, the demixing system will be “frozen” in the spinodal state. The compositions of each demixed phase will be given by the intersections of the tie lines with the opposite branches of the binodal curve. As demixing progresses before gelation, the composition of the polymer rich phase will follow the upper branch of the binodal curve, towards the polymer/non solvent axis. Beyond a given non solvent concentration in the mixture (G-L transition tie line, point C)

the polymer rich phase will have a polymer concentration that falls within the gelation region, the G-L transition tie line marks the beginning of the G-L region, that is, the region where a gelled polymer rich phase coexists with the liquid polymer lean phase. Once it has entered the G region, the gelled phase can either experience further syneresis, contracting its polymer structure, or simply continue to lose liquid by diffusion, with a fixed polymer structure.

#### **1.4. Wet phase inversion**

We can now analyze the membrane formation process during wet phase inversion. As explained in the previous sections, wet phase inversion occurs when a stable polymer mixture (binary or ternary) is immersed in a non solvent bath. The progressive exchange of solvent and non solvent within the system will eventually cause the precipitation of a polymeric matrix that constitutes the membrane.

In order to better understand the evolution of the system as it undergoes phase inversion, both diffusional and thermodynamic phenomena must be taken into consideration. As the homogeneous solution is cast into a thin film on a support (usually a glass plate) and immediately immersed in a non solvent bath (Fig. 1.7), the solvent, which must have a certain degree of affinity for the non solvent, experiences a diffusional drive towards the immersion bath ( $J_S$ ), while the non solvent does so towards the cast mixture ( $J_{NS}$ ).

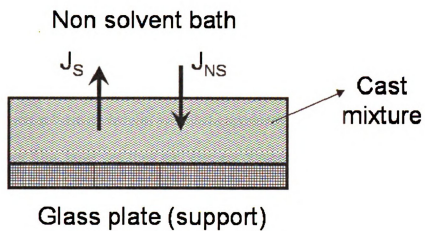


**Figure 1.7.** Schematic of solvent ( $J_S$ ) and non-solvent ( $J_{NS}$ ) transport for the wet phase inversion process.

The relative magnitudes of these two flows will have a critical effect on both the degree of asymmetry and the porosity of the final membrane. As soon as the film is immersed into the non solvent bath, the solvent molecules at the film/bath interface, which have a high affinity for the non solvent, will experience a high diffusive drive towards the non solvent bath. The non solvent molecules will also experience a diffusive drive towards the non solvent poor film; however, they will also encounter a diffusive resistance from the polymer molecules in the film, which have no affinity for the non solvent molecules. Such a difference between the high solvent outflow (from the film interface) and low non solvent influx into the film will result in a net solvent depletion at the film/bath interface. The film top layer thus becomes concentrated in polymer content with respect to the underlying bulk portion of the film, which still retains the original mixture composition. This is the basic phenomenon responsible for the formation of dense skin layers, characteristic of asymmetric membranes. The process is illustrated in Figure 1.8, represented by compositional path a-b.

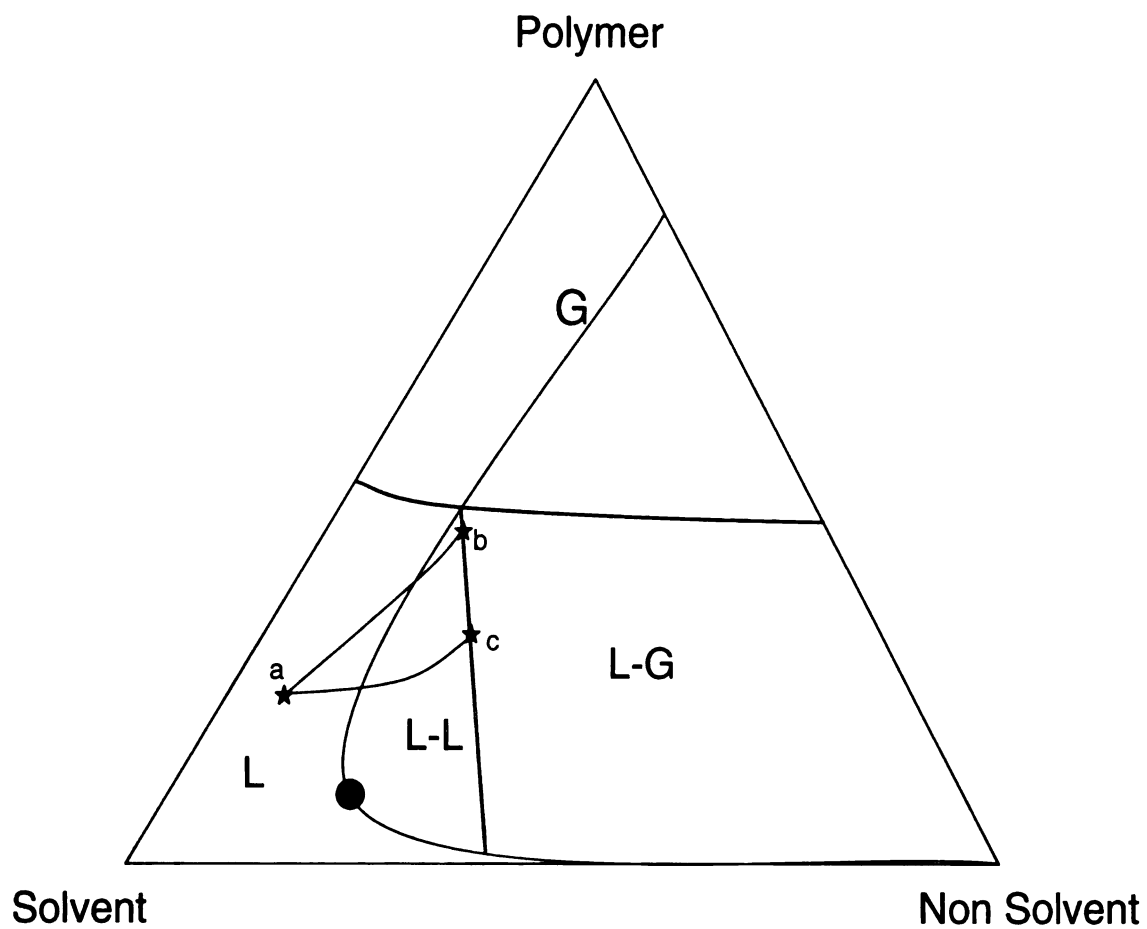


**Figure 1.8.**Demixing paths for a three component system during wet phase inversion

The interface area concentrates in polymer (moves towards the polymer vertex), with a less significant incorporation of non solvent (gradual inclination towards the non solvent vertex). Following this trend, most of the compositional path occurs within the stable region (L), delaying its entrance to the demixing gap. For this reason, this process is called delayed demixing. Eventually, the mixture enters the demixing zone; however, its “residence time” within the L-L region is small, almost immediately crossing the gelation threshold and solidifying in its polymer rich phase. During its short residence in the L-L region, the polymer lean phase demixes by nucleation and growth (the miscibility gap was crossed above the critical point), forming small solvent rich nuclei within the polymer rich phase. Upon gelation of the polymer rich phase, these small nuclei will constitute the final pores of the skin layer.

As the top layer concentrates in polymer and as non solvent penetrates within the system and mixes with the solvent, it gels creating a physical barrier to flow, thus reducing the diffusive drive for the solvent to leave the film towards the immersion bath; solvent outflow progressively slows down, causing the bulk film layers to follow a different compositional path (path a-c) than that of the toplayer. In this case, as solvent outflow is restricted, the mixture experiences a less drastic polymer concentration step before entering the miscibility gap; or, in other words, the compositional path does not markedly moves towards the polymer vertex, shifting instead towards the demixing zone.

Moving along this path, the residence time of the sub skin layers of the film in the thermodynamically stable region (L) is minimal, entering the miscibility gap almost

immediately after immersion, and thus experiencing what is known as instantaneous demixing. As sub skin layers enter the miscibility gap farther from the gelation threshold, liquid-liquid demixing unfolds for a longer period of time, allowing for the formation and growth of bigger nuclei before the onset of gelation and solidification of the polymer rich phase.

The above explained instantaneous demixing process becomes more pronounced towards the bottom of the film, where solvent outflow is most restricted due to the increasing resistance exercised by the coagulating layers above. Such decrease in solvent outflow rates along the film depth, from its fastest at the film/bath interface, to the slowest rate at the bottom of the cast film, and its direct effect on delayed (toplayer, path a-b) vs. instantaneous (towards the film bottom, Fig. 1.8, path a-c) demixing kinetics will give rise to the typical asymmetric structure observed in wet phase inversion membranes. If L-L demixing is allowed to unfold for a sufficient period of time before gelation, the solvent rich phase nuclei will grow and coalesce within the polymer rich phase, to form distinct solvent rich macro-nuclei, which will grow until the polymer rich phase gels and restricts further nuclei growth. These macro scale nuclei will reflect as macrovoids in the membranes solidified structure.

As follows, an analysis of the main parameters affecting the phase inversion process and thus directly influencing the membranes final structure will be offered.

#### **1.4.1.Solvent/non solvent affinity**

As the affinity between solvent and non solvent increases, the higher will be the tendency for these two components to mix. The increased propensity for mixing will result in an increased non solvent inflow, thus pushing compositional paths of the film's top layer, and sub layers, towards the binodal curve. Delayed demixing will shift towards instantaneous demixing, producing a thinner, more porous skin, as well as enhancing asymmetry and macrovoid formation.

#### **1.4.2.Polymer concentration in the casting mixture**

An increase in the polymer concentration of the mixture will shift the film interfacial polymer concentration towards the polymer vertex of the ternary system (Fig. 1.9, point a\*). This will result in delayed demixing, either causing the interface to enter the gelation region before liquid demixing, or reducing the L-L demixing period. In any case, the end result will be a denser and thicker skin, and in some cases further suppression of macrovoid formation. An increase in polymer concentration before phase immersion can be artificially induced by a pre-immersion evaporation step, during which a portion of the solvent is lost to the atmosphere and the solution interface is therefore pre concentrated in polymer before wet phase inversion proceeds. This combined approach is also known as dry-wet phase inversion.

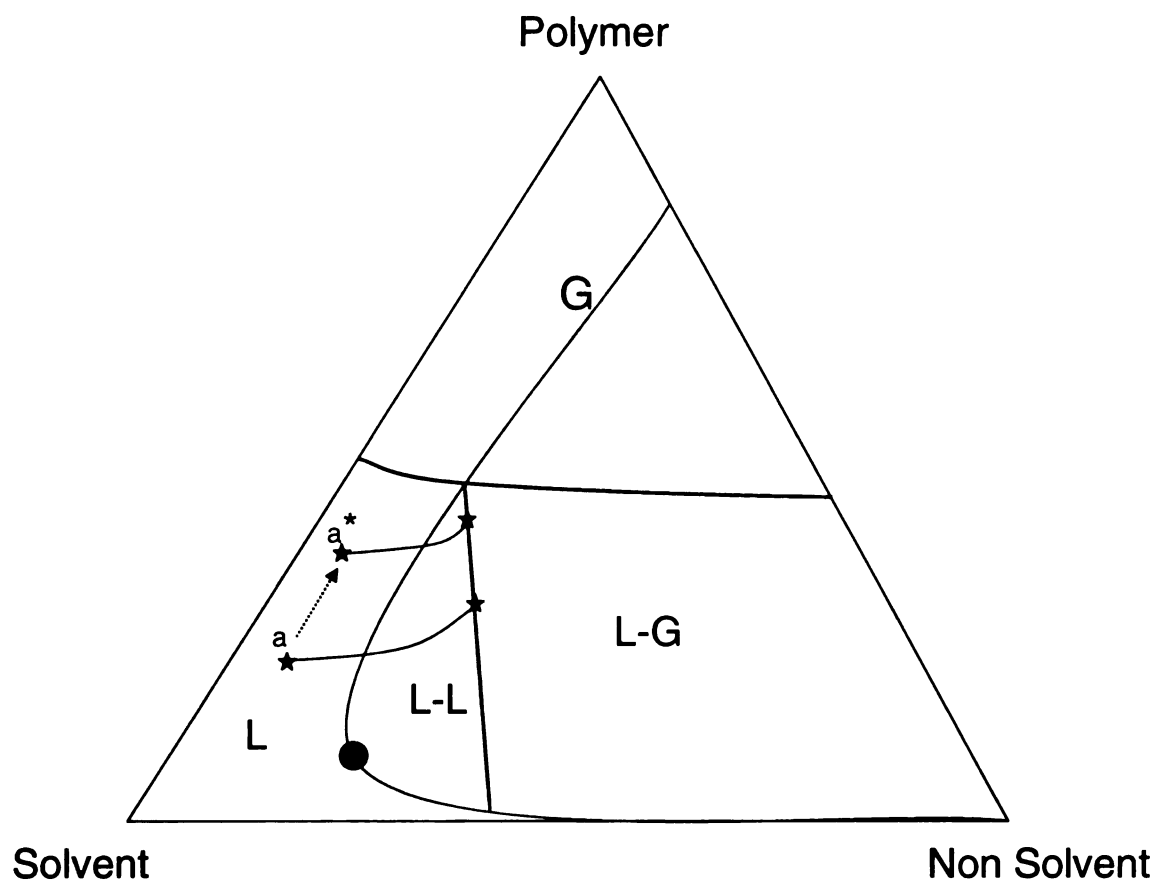


**Figure 1.9.**Effect of polymer concentration (point  $a^*$ ) on the demixing path of ternary system

### **1.4.3.Addition of non solvent to the casting mixture**

The addition of non solvent to the casting mixture will push the mixture composition closer to the miscibility gap (Fig 1.10, point a\*), therefore hastening the onset of L-L demixing and producing a more porous structure. The addition of non solvent can thus shift demixing kinetics from delayed to instantaneous.

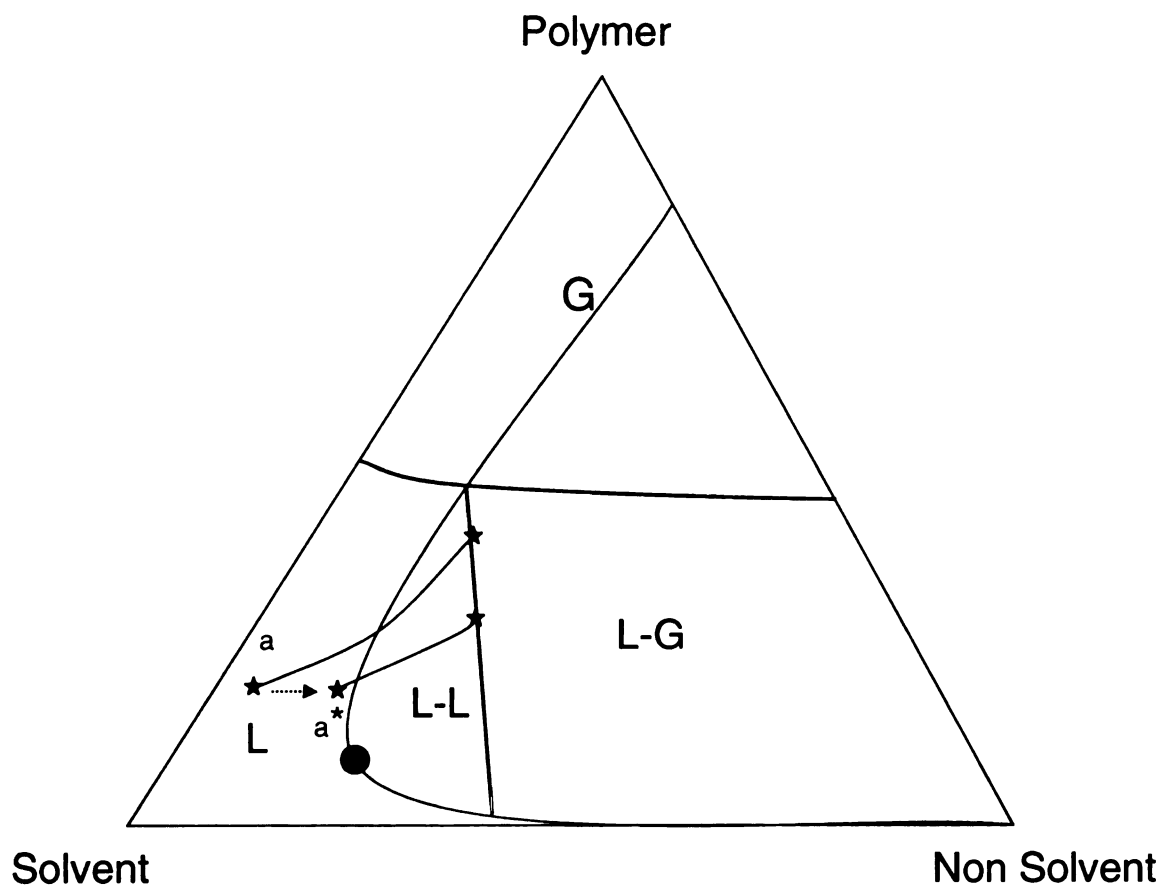


**Figure 1.10.**Effect of non solvent addition to the casting mixture (point  $a^*$ ) on the demixing path of ternary system

#### **1.4.4.Immersion bath temperature**

Increasing the temperature of the immersion bath can have different effects, specific to the particular studied system and immersion temperature. Generally, an increase in temperature results in an increase in the overall miscibility of the three components, which translates into the shrinking of the miscibility gap (Fig 1.11, horizontal arrow). The mixture thus remains in the homogeneous region (L) for a longer period of time during solvent/non solvent exchange, until it eventually gels. If gelation occurs before demixing, such delayed demixing effect results in a final denser membrane. However, an increase temperature can also delay the onset of gelation, as molecules have higher mobility at higher temperatures. The latter effect results in a viscosity decrease, which can simultaneously facilitate non solvent influx and retard gel formation, thus promoting instantaneous demixing (Fig 1.11, downwards arrow) and producing in turn a more porous membrane. The interplay and relative weight of these two opposing responses to an increase in temperature; namely delayed demixing due to binodal curve shrinkage versus instantaneous demixing induced by a decrease in the viscosity of the mixture and the gelation retardation, will determine the final structure of the membrane. The resulting trend will of course depend on the specific combination of solvent, polymer, non solvent and bath temperature.

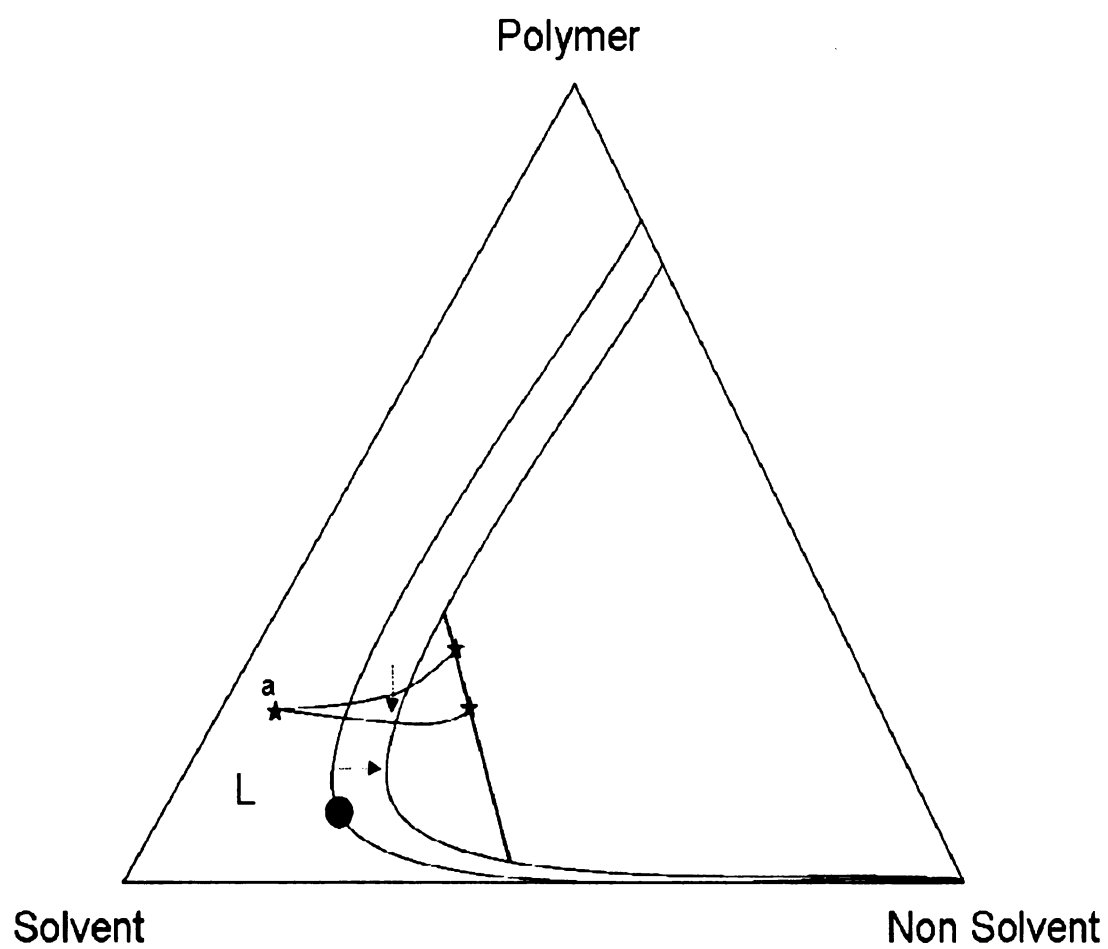


**Figure 1.11.**Effect of temperature increase on the demixing path of the ternary system.

#### **1.4.5.Addition of solvent to the immersion bath**

The effects of the addition of solvent to the coagulation bath can be evaluated in terms of the overall tendency of solvent and non solvent to exchange between the film interface and the immersion bath. The addition of solvent to the immersion bath will essentially reduce the driving forces (diffusive gradients) for both the non solvent to enter the film and the solvent to leave the film. Which of these two tendencies is more significantly reduced will determine whether the demixing process is delayed (faster solvent outflow than non solvent inflow, Fig 1.12 upwards arrow) or instantaneous (faster non solvent inflow than solvent outflow, Fig 1.12 downwards arrow); and will thus result in either a denser or more porous structure for the precipitated membrane, respectively. Again, this effect will be strictly dependant on the polymer/solvent/non solvent combination, and the concentration of solvent in the immersion bath.

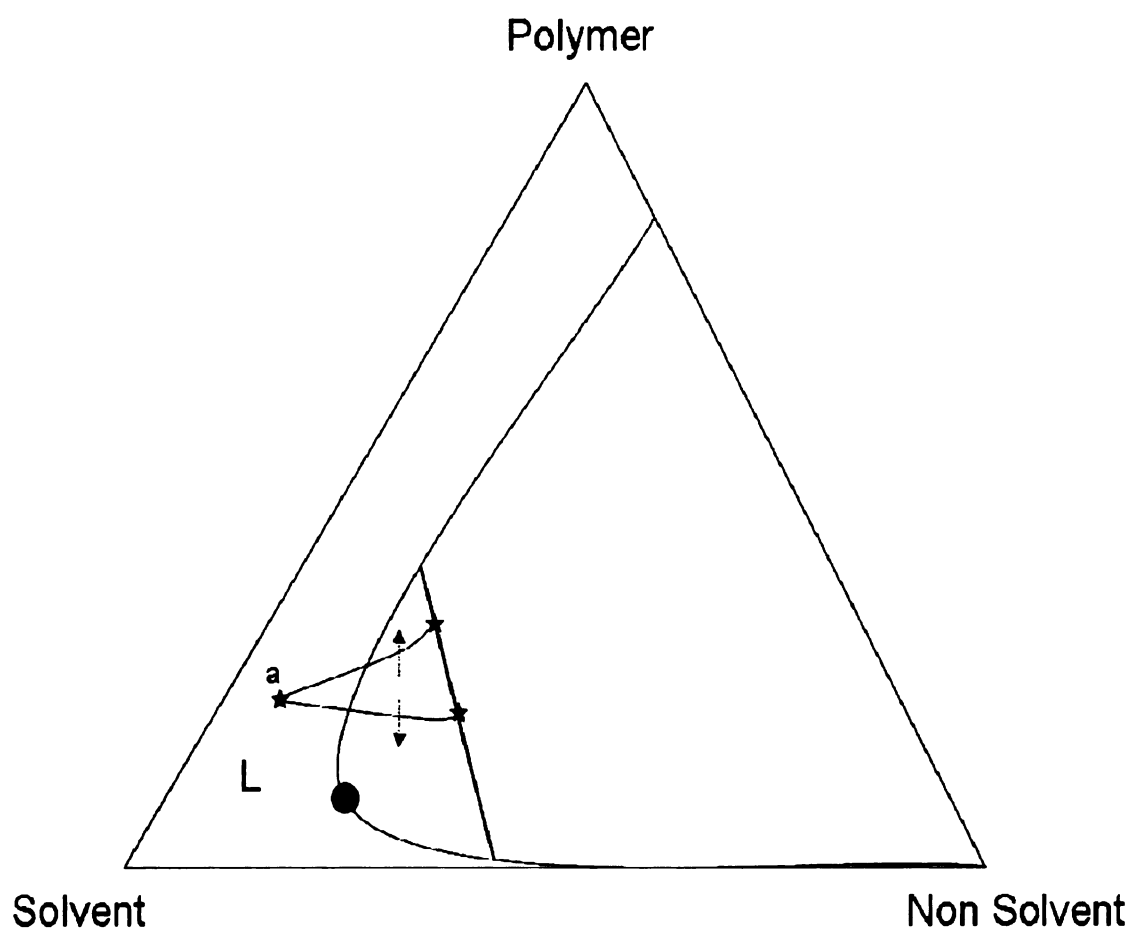


**Figure 1.12.**Effect of solvent addition to the coagulation bath on the demixing path of ternary system.

## References

1. R. W. Baker, Membrane Technology and Applications. Second ed. 2004, West Sussex, England: John Wiley & Sons.
2. R. E Kesting, Synthetic Polymeric Membranes, A Structural Perspective. Second ed. 1985, New York: John Wiley & Sons.
3. M. Mulder, Basic Principles of Membrane Technology. Second ed. 2003, Dordrecht, Netherlands: Kluwer Academic.
4. S. Loeb and S. Sourirajan, Sea water demineralization by means of an osmotic membrane, Adv. Chem. Ser. 38 (1962) 117-132.
5. A. S. Michaels, High Flow Membrane, US Patent 3.615.024. October 1971.
6. P. J. Flory, Principles of Polymer Chemistry. 1953, New York: Cornell Univ. Press.
7. D. Nunn, J. Elliot and J. C. Tan, Thermodynamics of mixing and separating polymers. 2008, University of Cambridge.

## CHAPTER TWO

### **Fullerene-polysulfone nanocomposite ultrafiltration membranes: Effect of filler shape and loading on membrane properties**

Original version submitted for a possible publication in

*Journal of Membrane Science*

by

Julian S. Taurozzi, Adam R. Rogensues, and Volodymyr V. Tarabara

Department of Civil and Environmental Engineering, Michigan State University,  
East Lansing, MI 48824, USA

## CHAPTER TWO

### **Fullerene-polysulfone nanocomposite ultrafiltration membranes: Effect of filler shape and loading on membrane properties**

#### **Abstract**

Nanoparticle-filled polysulfone membranes were synthesized by the wet phase inversion method. Two types of carbon nanoparticles of different shapes -  $C_{60}$  (nanospheres) and SWCNTs (nanorods) were used as fillers. In the study of the effect of nanoparticle loading, the membranes with 0.7 %  $C_{60}$ /polymer loading had higher hydraulic resistance and rejection as compared to polysulfone-only membranes and membranes with 10 %  $C_{60}$ /polymer loading. In the study of the effect of nanofiller shape, no significant differences were found in the hydraulic permeabilities and observed rejections for membranes filled with either  $C_{60}$  or SWCNTs. The demixing rate, indirectly evaluated as the rate of precipitation front advancement, and the viscosity of the casting mixture were found to correlate with the permeability and rejection of cast nanocomposite membranes. The correlations were rationalized in terms of the effect of nanoparticle fillers on the demixing and gelation processes occurring during phase inversion. The observed dependencies on the nanoparticle loading and shape were explained as resulting from the combined effect of 1) nanoparticle-induced destabilization of the polymer blend including the hastening of solvent transfer to the polymer-lean phase due to the hydrophobicity of the nanofiller and 2) nanofiller aggregation. The propagation rate of the precipitation front and the viscosity of the casting mixture were proposed as simple-to-measure predictors of membrane performance with potential application for the rational design of porous nanocomposites.

## 2.1 Introduction

Porous nanocomposite membranes can be prepared by incorporating nanoscale filler into a casting mixture (polymer, solvent, porogen, other components) and exposing the blend to a nonsolvent in order to initiate wet phase inversion [1-8]. The dependence of the wet phase inversion process on the composition of polymer/solvent/nonsolvent system can be understood within the framework of the Flory-Higgins model [9, 10]. The practical benefits of the model are limited because in practice, membranes are cast from blends with four or more components and because the determination of relevant thermodynamic parameters can be difficult [10, 13].

Numerous published studies on the effects of pore-forming additives (i.e., porogens) on the wet phase inversion process suggest that complex interactions arise from the porogen-induced changes in rheological and thermodynamic properties of polymer blends [14-21]. Less is known about the effect of *nanoparticulate* additives. Research on the preparation of phase inversion membranes from polymer blends doped with  $\text{TiO}_2$  [2, 3, 8],  $\text{Ag}^0$  [5, 22, 23],  $\text{Al}_2\text{O}_3$  [6, 7], and  $\text{SiO}_2$  [4, 20, 21] nanoparticles demonstrated that membrane skin properties (thickness, overall porosity, surface porosity) as well as the macrovoid morphology of the support layer can be affected by nanoparticle incorporation. The effect of carbon nanofillers on the properties of nanocomposite membranes prepared by wet phase inversion was also studied recently [1,26]. Brunet et al. [1] evaluated mechanical, hydraulic, and antifouling properties of SWCNT-filled polysulfone (PSf) membranes (1.4 % w/w SWCNT/PSf loading) using polyvinylpyrrolidone as the porogen and found no

significant changes in membrane properties, possibly due to the incomplete dispersion of the nanotubes in the casting mixture. Choi et al. [26] incorporated different amounts of multi-walled carbon nanotubes into PSf blends without porogen and correlated the nanotube loading to the hydraulic properties of the resulting membranes. The authors reported an increase in permeability and a decrease in rejection at intermediate loadings, with a reversal of the trend at higher loadings.

To our knowledge, the only experimental study focused on the links between the phase inversion process and properties of porous composite membranes formed from particle-doped polymer blends was that by Aerts et al. [20, 21]. The authors used light microscopy to investigate the effect of the addition of hydrophilic particles ( $\text{SiO}_2$ , Aerosil 200) to polysulfone blends by measuring changes in viscosity and demixing behavior in the porogen-free quaternary (polymer, filler, solvent, nonsolvent) blends and related the changes to morphological characteristics of the cast membranes. The presence of a small amount of filler was shown to lead to an increase in the demixing rate; a decrease in the demixing rate with the further increase of the filler was attributed to a higher viscosity, which increased with an increase in filler loading throughout the entire loading range studied (up to 3 vol. %). Aerosil 200 primary particles are 12 nm spheres but the size of the filler dispersed in the solvent/polymer mixture or embedded in the cast membrane was not reported. Aerts et al. used a low intensity dispersion technique (mixing rather than sonication), which was likely not sufficient to disperse silica powders into aggregates of sizes comparable to the primary particle size (see Supporting Documentation (SD)).

The present work is on the mechanisms of formation of phase inversion porous membranes cast from fullerene-filled polymer blends. The study focused on the effects of nanoparticle loading and shape and, indirectly, by contrasting our findings with those of Aerts et al. [20, 21], on the effects of filler hydrophilicity. Two types of carbon nanoparticles - C<sub>60</sub> (nanospheres) and single-walled carbon nanotubes (nanorods) - were used as model fillers representing idealized zero- and one-dimensional fillers of very similar surface chemistry. Polyvinylpyrrolidone, which is also a known dispersing aide for C<sub>60</sub> and carbon nanotubes [32, 33], was used as the porogen in all polymer blends studied. The differences between nanoparticle-free and nanocomposite membranes were interpreted in terms of nanoparticle-induced changes in the properties of the casting mixture and resulting changes in demixing and gelation processes.

## **2.2 Experimental**

### **2.2.1 Materials**

N-Methyl-2-pyrrolidone (Aldrich, 99% ACS reagent), polyvinylpyrrolidone (Aldrich, MW avg. 10 kDa), and polysulfone (Solvay, Udel P-3500 LCD pellets, MB8, MW avg. 79 kDa) were all used as received. C<sub>60</sub> fullerenes (99+ % purity) were purchased from MER Corp. Single-walled carbon nanotubes (purity > 90%) were purchased from Cheaptubes, Inc. The ultrapure water used in all experiments was supplied by a commercial ultrapure water system equipped with a terminal 0.2 µm cartridge microfilter. The resistivity of water was greater than 16 MΩ·cm. 150 kDa dextran (DIN certified standard, Sigma-Aldrich) was used as rejection probe.

### **2.2.2 Preparation of polysulfone membranes**

Polysulfone membranes were prepared by wet phase inversion. Polyvinylpyrrolidone (PVP) was added to the casting mixtures as a pore forming agent (i.e., a porogen.) The composition of each casting mixture is given in Table 2.1.

Component	Membrane			
	PSf	PSf/C <sub>60</sub> -0.7	PSf/C <sub>60</sub> -10	PSF/NT-0.7
PSf (% w/w)	12.0	12.0	11.9	12.0
PVP (% w/w)	5.0	5.0	4.9	5.0
NMP (% w/w)	83	82.9	82.0	82.9
Filler (% w/w)	---	0.7	10.0	0.7

**Table 2.1.** Components of membrane casting mixtures (% w/w). Weight % of filler is expressed with respect to the mass of PSf.

To prepare the membranes, PSf pellets and porogen were added to N-methyl-2-pyrrolidone (NMP) and the mixture was stirred at 60 °C until PSf completely dissolved and a homogeneous casting solution was formed. The resulting viscous solution was cast as a thin film on a 25 cm x 30 cm flat glass plate using a micrometric film applicator (Model 3570, Elcometer, Inc.). All of the cast films had a drawdown thickness of  $(300 \pm 1) \mu\text{m}$ . Immediately after casting, the film was immersed in a nonsolvent (water) bath to induce phase inversion. The water bath was maintained at the room temperature (ca. 22 °C). Free standing membrane sheets that formed were thoroughly rinsed with deionized water to remove residual solvent.

#### *2.2.2.1 Preparation of nanoparticle-filled membranes*

Dry C<sub>60</sub> powder was added to NMP to produce nC<sub>60</sub> organosols with two different C<sub>60</sub> loadings: 1 mg/mL and 15 mg/mL. Porogen (PVP) and polymer (PSf) were then added to the organosols to obtain the casting mixtures used to prepare nanocomposite membranes with two different filler-to-polymer ratios (0.7 % and 10 % by weight, respectively). Similarly, 0.7 % w/w SWCNT-filled membranes were prepared following the same procedure and using 1 mg/mL SWCNT/NMP organosols. The 1 mg/mL organosols were dispersed by sonication for 20 min at 25 W (horn probe, Sonicator 3000, Misonix, Inc.). The obtained organosols were then transferred to 25 mL Erlenmeyer flasks containing the polymer (PSf) and the porogen (PVP). The resulting casting mixtures were then homogenized by prolonged (ca. 1 day) stirring. The 15 mg/mL organosols were prepared directly in 25 mL Erlenmeyer flasks and dispersed by sonication for 24 h using a bath

sonicator (Aquasonic 50T, VWR Scientific). Probe sonication was not used in this case to prevent nanoparticle losses, since at such high loadings a considerable amount of organosol residue was observed to remain in the scintillation vials after transfer to the Erlenmeyer flasks when horn probe sonicator was used. Such residue was not observed for the lower loadings; thus probe sonication was used for mixtures with lower NP loadings to shorten dispersion time. PSf and PVP were added to the 15 mg/mL filler/NMP organosols and the mixtures were stirred at 60 °C until homogeneous solutions were obtained. Nanoparticle-filled membranes were then cast from these viscous mixtures following the procedure explained in section 2.1.2.2.

### **2.2.3 Characterization of casting mixtures and cast membranes**

Particle size distribution in the organosols was measured using dynamic light scattering (ZetaPALS, BI\_MAS Option, Brookhaven Instrument Corp.). Measurements were recorded in 5 cycles of 2 min each using a 30% cutoff dust filter.

The steady zero-shear viscosity of casting mixtures with variable C<sub>60</sub> loadings was recorded at room temperature using a programmable rheometer (Model DV-III, Brookfield).

The influx of the non-solvent (water) into the casting mixture was quantified using confocal microscopy. For each casting mixture, a water droplet and a droplet of the casting mixture were placed on a microscope slide; the two droplets were then brought

into contact by capillary action, induced by pressing a cover slip against the glass slide.

The advancement of the precipitated polymer front was monitored over time by laser-scanned brightfield imaging using an Olympus FluoView<sup>TM</sup> FV1000 confocal microscope with a 488 nm Ar laser line and a 4X PlanFLN objective (NA 0.13). For each sample, 333 brightfield images were taken with 1.13 s interval between images (Fig. 2.2 B).

The hydraulic resistance and rejection of the membranes were measured using a stirred Amicon 8010 dead-end ultrafiltration cell (Millipore Corp.) connected to a 5 L pressurized feed tank (Alloy Products Corp) filled with ultrapure water. Prior to each test, the membrane coupons were compacted at 40 psi until steady permeate flux was attained. The permeate flux was measured continuously by collecting the filtered water on a digital balance (AV8101C, Ohaus Corp.). The extent of membrane compaction was determined by comparing the initial and steady state values of permeate flux. To measure membrane rejection, 20 mg/L aqueous solution of 150 kDa dextran was filtered through the compacted membrane. Dextran concentration in the permeate was measured using a total organic carbon analyzer (Model 1010, OI Analytical).

## 2.3. Results and Discussion

### 2.3.1 Casting mixture properties

#### 2.3.1.1 Nanoparticle dispersions in *N*-methyl-pyrrolidone

Suspensions of SWCNTs and nanoscale  $C_{60}$  aggregates ( $nC_{60}$ ) in NMP were prepared by mixing the nanoparticles with NMP and sonicating the resulting organosols for 20 min (see section 2.2.2.1.) Particle size distribution was measured for 1 mg/L organosols of SWCNTs and  $nC_{60}$  by dynamic light scattering. The measured sizes of  $nC_{60}$  aggregates and SWCNT bundles in NMP (before other components - PSf, PVP - were added to the casting mixture) were  $(181 \pm 20)$  nm and  $(183 \pm 17)$  nm, respectively. SEM images of sonicated and dried 1 mg/mL  $C_{60}$ /NMP and SWCNT/NMP organosols are given in SD (Fig. SD.2.1)

#### 2.3.1.2 Viscosity of nanoparticle ( $C_{60}$ ) – polymer (PSf) – solvent (NMP) – porogen (PVP) blends: Effect of nanoparticle loading

Casting mixtures with 0.7% loading of  $nC_{60}$  had a higher viscosity than nanoparticle-free controls; this trend was reversed when the nanoparticle loading was increased to 10% (Fig. 2.1 a).

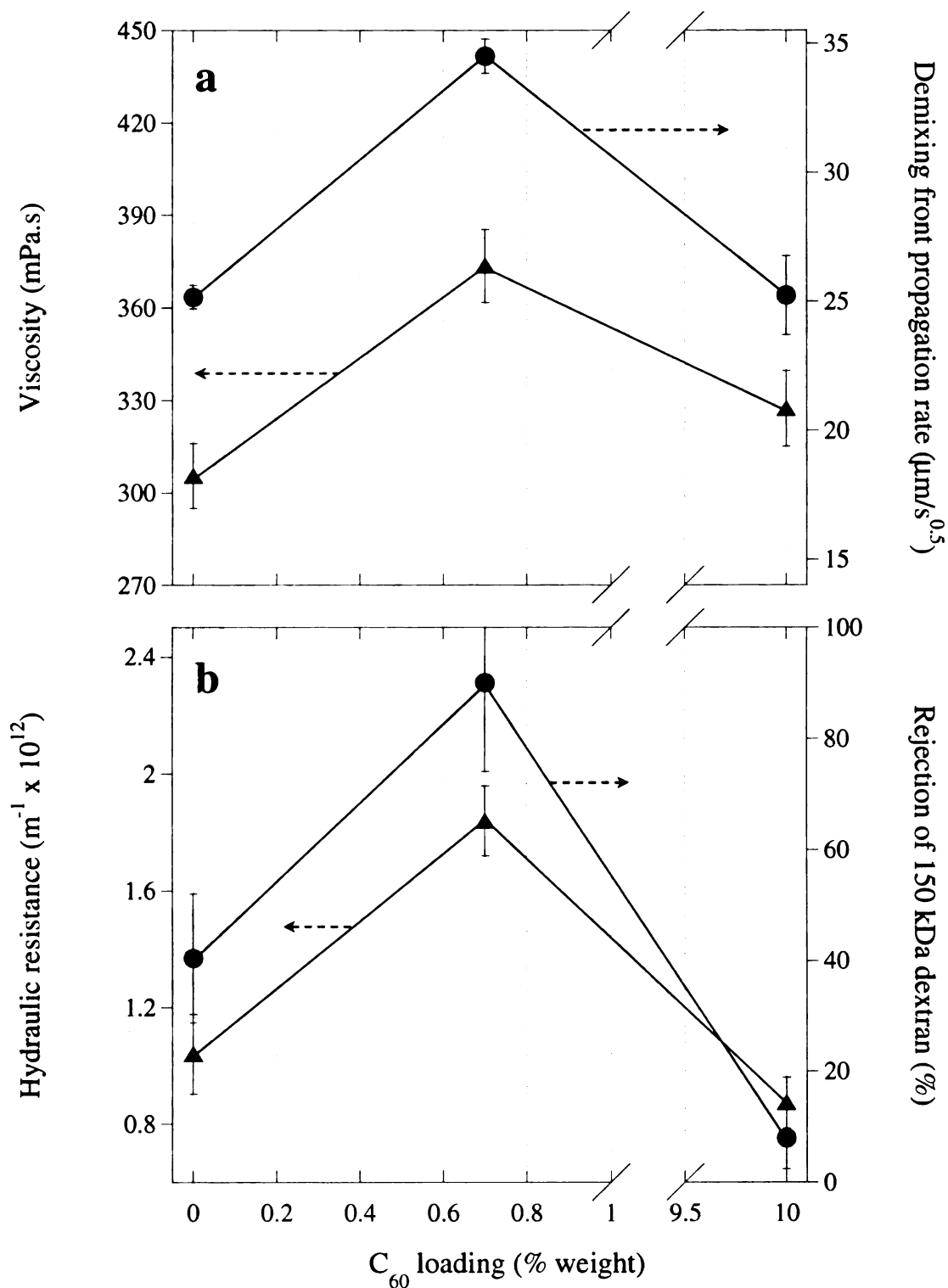


**Figure 2.1.** Viscosity and demixing front propagation rate for PSf-PVP- $C_{60}$  blends (a) and hydraulic resistance and 150 kDa rejection for  $C_{60}$ -filled PSf membranes (b) at 0% (control), 0.7 % and 10 % w/w  $C_{60}$ /PSf loadings.

Incorporation of different amounts of carbon fillers (carbon black [29] and spherical nanoparticles [30, 31]) into polymer blends were reported to increase blend viscosity with higher increases observed for fillers of smaller size. The observed effects of filler loading and size were attributed to a change in the relaxation modulus and the elastic recovery of the blend, and were correlated to changes in the available polymer-filler interfacial surface area [29] that is affected by both loading and size of the filler. The increase in viscosity observed in our study for casting mixtures with 0.7 % loading of nanoparticles is in agreement with the trends reported in these studies. Aerts et al. [20, 21] recorded an increase of viscosity of PSf/NMP blends filled with hydrophilic ( $\text{SiO}_2$ ) particles with an increase in filler loading up to 3 vol. % and interpreted this effect as a consequence of adsorption of polysulfone chains to the filler surface. In our study, a reversal of the viscosity trend at higher (10 %) filler loading was observed. We *hypothesize* that the reversal is due to filler aggregation. This hypothesis is consistent with results of a recent modeling study wherein the viscosity of polymer-nanoparticle ( $\text{C}_{60}$ ) melts was shown to be highly sensitive to the degree of nanoparticle clustering and to be proportional to the total surface area of nanoparticle aggregates [31]. The aggregation is also more likely for blends with low nanoparticle-polymer affinity, which is the case for the fullerene/polysulfone pair. Adding the dispersing aid (PVP) improved the affinity between fullerenes and polysulfone.

It must be noted that even though the particle size distribution of  $\text{C}_{60}$  clusters suspended in NMP at 1 mg/L (see section 2.3.1.1) was measured, the measured  $n\text{C}_{60}$  sizes may be differ from the sizes of  $n\text{C}_{60}$  in the casting mixture that contains the polymer and the

porogen. Generally, the relative chemical affinity and interactions between the filler and other casting mixture components may alter the aggregation state of the filler within the melt throughout the membrane formation process. For example, the addition of PVP, a known dispersing aide for  $C_{60}$  and carbon nanotubes [32, 33], can be expected to result in a decrease in the size of filler clusters especially at low filler loadings where there is a high excess of PVP with respect to the filler. As the filler loading is increased, the porogen effect should decrease allowing for aggregation to occur and for larger clusters with smaller specific surface area to form. This scenario is consistent with the increase of viscosity that we observed to accompany the increase of filler loading from 0.7% to 10% (Fig. 2.1 a)

### *2.3.1.3 Demixing behavior of polymer (PSf) – nanoparticle ( $nC_{60}$ ) – solvent (NMP) – porogen (PVP) blends exposed to nonsolvent (water): Effect of nanoparticle loading*

The results on the propagation rate of the polymer precipitation front (Fig. 2.1 a, Fig. SD.2.3) show higher precipitation front propagation rates and indicate a faster gelation for blends with 0.7 %  $C_{60}$  loading as compared to  $C_{60}$ -free controls and blends with 10 %  $C_{60}$  loading. In what follows, an analysis of this behavior will be offered in terms of the effect of the nanoparticle filler on the demixing process.

Figure 2.2 A shows a schematic of a typical isothermal phase diagram for a three component (polymer-solvent-nonsolvent) system. Point “a” represents a homogenous polymer-solvent blend, while the “a” → “c” transition illustrates the compositional path of

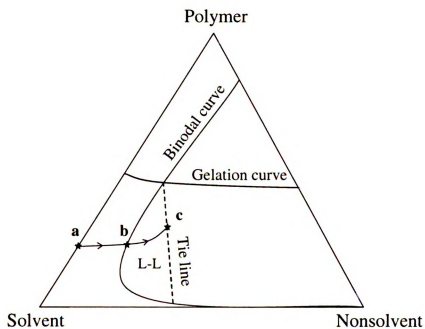
the blend as it incorporates nonsolvent and separates (i.e., demixes) into polymer-rich and polymer-lean phases. This results in the formation of a solid polymer matrix that is the membrane [10, 13]. Point “b” corresponds to the point of initiation of the phase separation as the system crosses the binodal curve and undergoes liquid-liquid demixing (region L-L) following compositional tie lines. At point “c”, the polymer concentration in the polymer-rich phase reaches critical value (gelation point) and the polymer solidifies forming the membrane. Pore size and porosity of the membrane are controlled by the time available for solvent-rich (i.e. polymer-lean) nuclei to form and grow in the blend; this is the time from the moment phase separation begins as the system enters the binodal region (point b, Fig. 2.2 A) and the time when gelation of the polymer-rich phase occurs (point c, Fig. 2.2 A). If gelation occurs earlier (i.e., faster “a” → “c” transition), the nuclei will have less time to grow, thus resulting in the formation of smaller pores [9].

In this study, the rate of precipitation front propagation was used as an indirect measure of the demixing rate (i.e., of how fast the gel is formed upon incorporation of nonsolvent). As the nonsolvent diffuses into the droplet of polymer blend, first the outermost interfacial layer of the droplet demixes into polymer-rich and polymer-lean phases (Region L-L, Fig. 2.2 A) and the polymer-rich phase within this layer reaches the gelation point (“c”). The entire process (if not diffusion limited) takes less than 1 s and manifests itself as an increase in the optical density of the precipitated portion of the droplet. As the nonsolvent diffuses further into the droplet, successive layers of the blend undergo transition from a completely mixed state to a gelled state. It is the reasoning that the rate of the advancement of the precipitation front should be proportional to the rate of

demixing of every one of the successive differential layers that was at the base of the postulate that the rate of precipitation front propagation can be used as a measure of the demixing rate. In the past, precipitation front propagation data was used to discriminate between instantaneous and delayed demixing [20]. By using this data only as a measure of the demixing rate we take a more conservative approach that recognizes that the difference between the instantaneous and the delayed demixing lies in the difference in the amount of time it takes for the system to reach (not the gelation state but) the binodal curve that can shift in response to the addition of a filler.

It should also be noted that the hydraulic resistance that the precipitated gel exerts to the nonsolvent is another factor that might control the propagation rate of precipitation front. However, because there was a reverse correlation between the rate of precipitation front propagation and the resistance of the resulting membrane (Fig. 2.1), we concluded that the hydraulic resistance of the precipitated region to the inflowing nonsolvent was a factor of secondary importance that played a mitigating role if any.

A)



B)



**Figure 2.2.** Schematic (A) of an isothermal phase diagram for a three component (solvent-polymer-nonsolvent) system and laser-scanned brightfield images (B) of demixing front propagation in PSf-C<sub>60</sub>-PVP-NMP blends as a function of time (in seconds) of exposure to nonsolvent (water).

The data on the rate of precipitation front advancement can be analyzed in terms of the thermodynamic destabilization effect of nanoparticulate fillers. Previous studies on the effect of porogen additives on the demixing of polymer blends showed that the addition of a fourth component (porogen) increases the thermodynamic instability of the system, hastening the onset of demixing [17, 19]. Addition of hydrophobic carbon nanoparticles (a fifth component) is likely to have an analogous effect on the demixing process; the addition of nanoparticles would result in an overall reduction of the blend's affinity for the polar nonsolvent (water), accelerating gelation as less nonsolvent is needed to initiate phase separation. This effect however, should be expected to be strongly dependent on the degree of dispersion of the filler within the blend. As the nanoparticles aggregate, the nanoparticle-polymer interfacial area will become smaller, decreasing the destabilizing effect of nanoparticles. Thus, C<sub>60</sub> aggregation (see section 2.3.1.2) would explain why the propagation front trend with C<sub>60</sub> loading is reversed at higher (10 %) C<sub>60</sub> content.

### **2.3.2 Membrane hydraulic properties**

Figure 2.1 b shows the permeability and observed rejection of 150 kDa dextran for C<sub>60</sub>-filled membranes as a function of C<sub>60</sub> loading. The membranes with 0.7 % C<sub>60</sub> loading show a simultaneous decrease in permeability and increase in rejection, as compared to C<sub>60</sub>-free membranes (controls) and membranes with 10 % C<sub>60</sub> loading. This result points to smaller skin pores and/or smaller overall porosity of the skin for the membranes with 0.7 % loading.

The results can be explained in terms of the properties of the casting mixtures. As mentioned in section 2.3.1.3, the porosity of the membrane skin will depend on demixing time (“b”-“c” transition, Fig. 2.2). Measurements of nonsolvent diffusion rate into C<sub>60</sub>-filled polymer blends (Fig. 2.1 a) show that blends with 0.7 % C<sub>60</sub> loading gel faster than C<sub>60</sub>-free and blends with 10 % C<sub>60</sub> loading. The decreased permeability and increased rejection of membranes prepared from blends with 0.7 % C<sub>60</sub> loading can be explained by shorter demixing periods that result in denser membrane skins (section 2.3.1.3). Furthermore, the hydrophobic character of the filler would result in an enhancement of solvent outflow towards the polymer-rich phase of the blend, hastening solvent-nonsolvent exchange and increasing the local polymer concentration. The combined effect of i) nanoparticle-induced destabilization of the system and ii) hastening of solvent transfer to the polymer-lean phase due to the hydrophobicity of the nanofiller would explain the accelerated gelation for the C<sub>60</sub>-filled membranes with respect to nanoparticle-free blends. The observed decreases in both viscosity and precipitation front propagation rate for the casting mixtures with 10% C<sub>60</sub> loading point to a mitigation of these effects due to a decrease in NP-polymer interfacial area upon filler aggregation, resulting in a reversal of the trend in the observed hydraulic properties for membranes with 10 % C<sub>60</sub> loading.

The observed changes in the demixing behavior of C<sub>60</sub>-filled blends can, in principle, be described using a phase diagram and the changes in the relative composition of the casting mixture during the demixing process. To accurately describe the changes,

however, a phase diagram for the five component (polymer, solvent, nonsolvent, porogen, and filler) system would have to be constructed. In addition to the obvious difficulty of visualizing and interpreting the evolution of the system within the confines of a 4-dimensional prism, measurements necessary to track nanofiller-induced changes in binodal and gelation curves may not be always possible. For the polymer blends studied in this work, cloud point measurements, for example, could only be conducted for the nanoparticle-free casting mixtures (see SD, Fig. SD.2.2). Although one can measure values of *apparent* cloud points [20, 21], in our opinion it is impossible to conclude with certainty whether the observed polymer precipitation upon nonsolvent addition in the presence of nanoparticles corresponds to the actual gelation point of the system or to other nanoparticle-induced effects such as, for example, settling of nanoparticle-polymer aggregates.

### **2.3.3 Nanocomposite membranes doped with nanoparticles of different shapes**

The effect of nanofiller shape on the demixing behavior of nanoparticle-filled blends was studied by preparing and characterizing membranes filled with carbon fillers of different shapes: C<sub>60</sub> (nanospheres) and SWCNTs (nanorods). The model fillers represented idealized zero- and one- dimensional fillers of very similar surface chemistry.

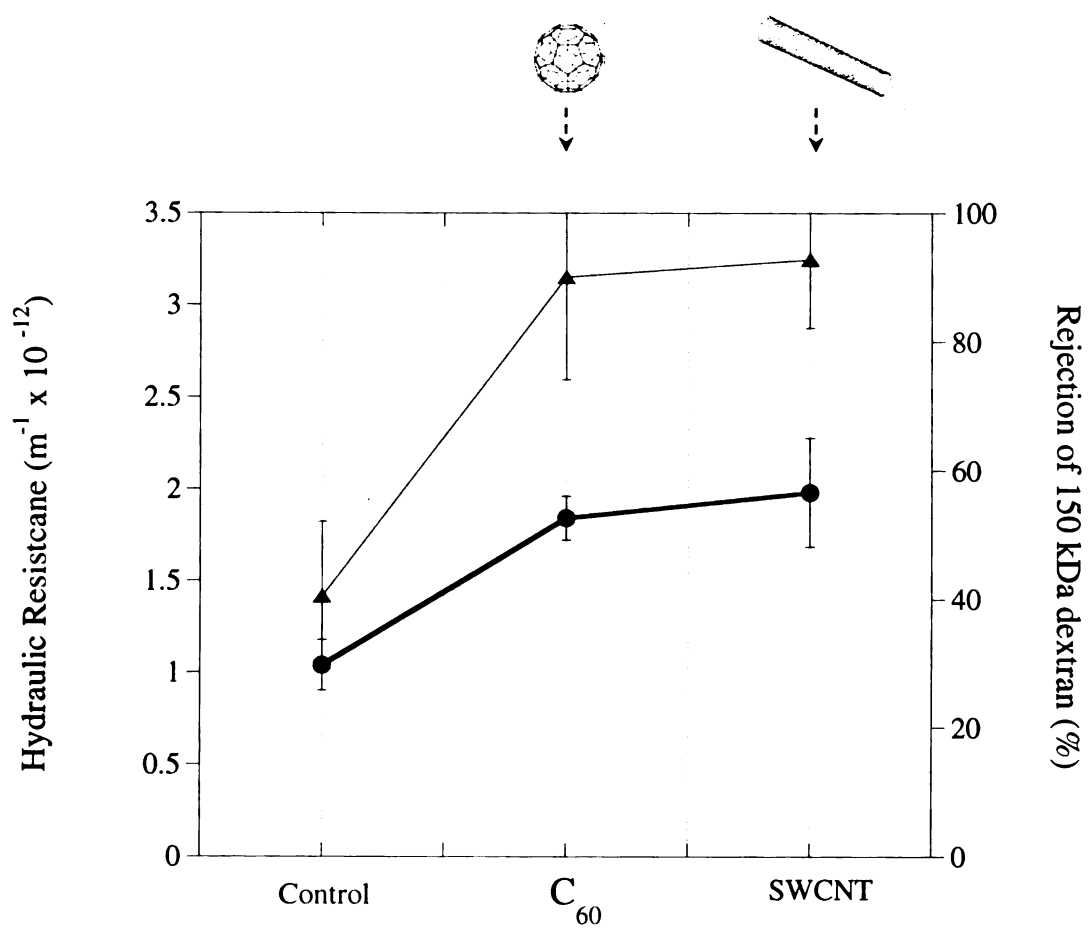


**Figure 2.3.** Hydraulic resistance (circles) and rejection (triangles) of 150 kDa dextran for PSff membranes filled with  $\text{C}_{60}$  and SWCNTs at a filler/polymer weight loading of 0.7 %.

The permeabilities and observed rejection of membranes filled with either C<sub>60</sub> or SWCNTs were similar (Fig. 2.3). Dynamic light scattering measurements indicated that both C<sub>60</sub> and SWCNTs suspended in NMP existed as aggregates with approximately the same effective diffusion coefficient that corresponded to the effective hydrodynamic diameter of ca. 180 nm (section 2.3.1.1). Given the identical surface chemistry of C<sub>60</sub> and SWCNTs, it can be expected that chemical interactions of both types of nanoparticles with the other mixture components are the same. With the hydrodynamic and chemical properties matching, the only difference between the two fillers was the morphology of the primary (as opposed to aggregated) nanoparticles. Evidently, this difference did not translate into measurable differences in hydraulic properties of C<sub>60</sub>- and SWCNT-filled membranes. This result was also consistent with the hypothesis that nanoparticle aggregation state within the casting mixtures controls the phase inversion process.

## 2.4. Conclusions

Nanoparticle-filled polysulfone membranes were synthesized by the wet phase inversion method. Three types of fullerene nanoparticles -  $C_{60}$  (nanospheres) and single-walled carbon nanotubes (nanorods) were used as model fillers representing idealized zero-, and one- dimensional fillers of identical surface chemistry. The hydraulic resistance and rejection of  $C_{60}$ -filled membranes peaked at the relatively low (0.7%) loading and were similar for  $C_{60}$ /PSf and SWCNT/PSf membranes cast from blends with the same nanoparticle loading. Demixing front propagation rate and casting mixture viscosity were found to correlate with membrane permeability and observed rejection. The observed correlations were explained in terms of the following effects:

1. Nanoparticles exert a thermodynamic destabilization effect within the polymer blend, hastening the onset of demixing thereby reducing the available time for pore growth and leading to faster gelation and formation of smaller pores. The destabilization of the blend is further enhanced by the nanoparticles' hydrophobicity. Hydrophobic nanoparticles enhance solvent transfer to the polymer-lean phase and accelerate gelation, with smaller pores formed as a result.
2. While  $C_{60}$  and SWCNTs have distinctly different shapes, both nanoparticles clustered to form aggregates with the similar effective diffusion coefficient that translated into the effective hydrodynamic diameter of ca. 180 nm.

The observed hydraulic properties for C<sub>60</sub>/PSf and SWCNT/PSf membranes at equal nanoparticle loadings were similar. Thus, the phase inversion process appears to depend on the size, shape (and chemistry) of the nanoparticle aggregate within the casting mixtures and not on the size, shape (and chemistry) of the primary nanoparticle.

Demixing front propagation rate and casting mixture viscosity were proposed as indirect indicators of the degree of aggregation and thermodynamic destabilizing effect of nanoparticle filler, respectively. Such easy-to-measure indicators can be potentially applied for the rational design of porous nanocomposites.

## **Acknowledgements**

This material is based upon work supported by the National Science Foundation under grant no. OISE-0530174. We thank Solvay Advanced Polymers, L.L.C. for providing the polysulfone for membrane synthesis and XG Sciences, Inc for donating exfoliated graphite nanoplatelets.

## **Supporting Documentation**

### **Fullerene-polysulfone nanocomposite membranes: Effect of filler shape and loading on membrane properties**

Original version submitted for a possible publication in

*Journal of Membrane Science*

by

Julian S. Taurozzi, Adam R. Rogensues, and Volodymyr V. Tarabara

Department of Civil and Environmental Engineering, Michigan State University,

East Lansing, MI 48824, USA

### **SD.2.1.SEM sample preparation procedure**

For SEM imaging, a droplet of the 1mg/mL nanoparticle/NMP organosols was deposited on a silica wafer and let to dry. The dry samples were coated with osmium for 20 s at a current of 10 mA using an osmium plasma coater (model NEOC-AT, Meiwa Shoji Co., Osaka, Japan). A Hitachi S-4700II field emission scanning electron microscope operated in ultra high resolution mode was used to record SEM images (Fig. SD.2.1).

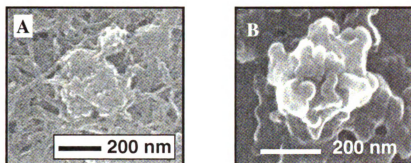


**Figure SD.2.1.** SEM images of 1 mg/mL SWCNT/NMP (A) and C<sub>60</sub>/NMP (B) organosols.

### **SD.2.2.Cloud point measurements**

The cloud points of nanoparticle free casting mixtures were determined following Aerts et al. method [1], by which mixtures of PSf and NMP of different polymer concentrations (12.2, 8.8, 6.1, 4.6 and 2.7 % w/w) were titrated with an NMP:Water (66:34 w/w) solution until appearance of turbidity. The experiments were conducted on a temperature controlled heat plate at constant 60 °C. The cloud point for each mixture was calculated from the added amounts of solvent and non solvent at which turbidity remained after 24 hs. of mixing. The obtained cloud points are shown in Fig. SD.2.2

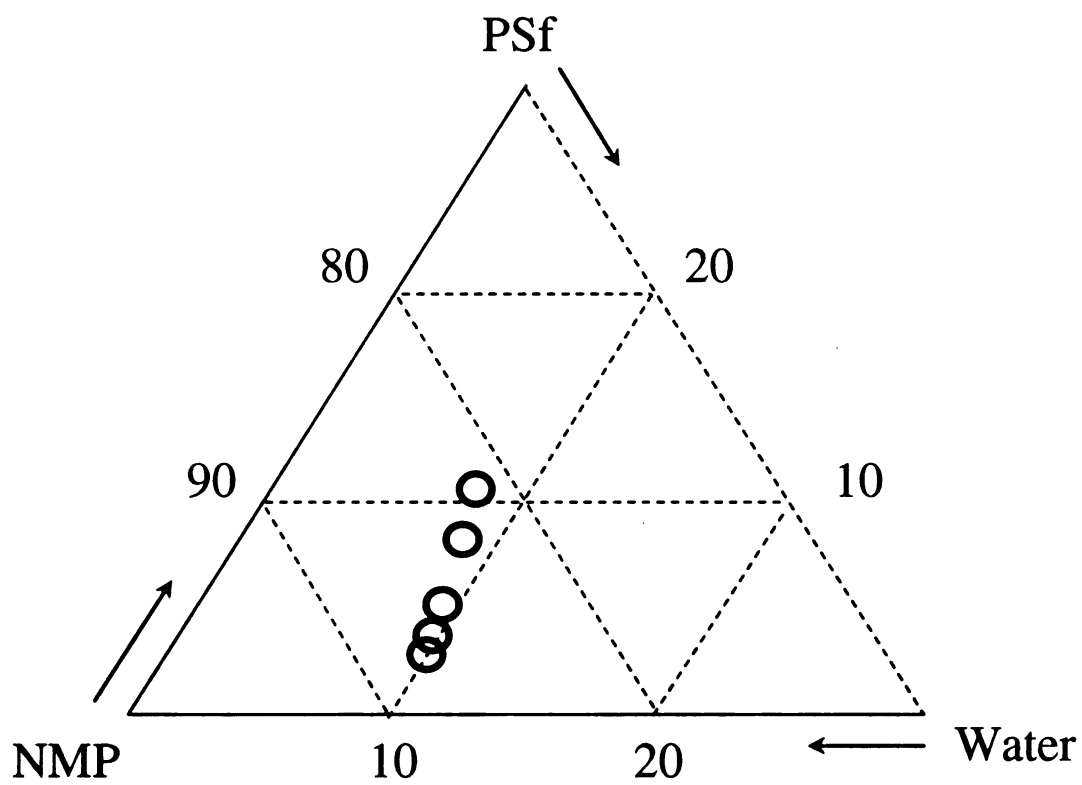


**Figure SD.2.2.**Cloud points for PSf-NMP-water system.

### SD.2.3.Sonication of silica powders

Table 1 shows the measured effective diameters for silica clusters obtained after sonication of source silica powders in N, N-Dimethylacetamide (DMA) using a horn probe ultra-sonicator (Sonicator 3000, Misonix Inc., Newtown, CT). A variety of source silica powders (Nanoamor Inc., Los Alamos, NM) with different primary particle sizes, ranging from 10 to 3000 nm, were sonicated at different sonication intensities and sonication times. In all cases, the size of the resulting silica clusters was at or above ~ 200 nm.

Primary particle size (nm)	Powder mass (g)	Solvent	Solvent (mL)	Sonication time (min)	Sonication intensity (%)	Cluster Size (nm)
10	0.5	DMA	40	5	100	259.4
10	0.5	DMA	40	15	100	248.3
10	0.05	DMA	40	30	100	212.6
10	0.05	DMA	40	45	100	195.8
10	0.5	DMA	40	30	20	244
10	0.5	DMA	40	5	50	271.8
80	0.5	DMA/PEG	40/6	15	100	222.2
80	0.5	DMA	40	15	100	197
1000	0.5	DMA	40	10	20	691.8
1000	0.5	DMA	40	5	50	559.5
1000	0.5	DMA	40	5	100	525.7
1000	0.5	DMA	40	15	100	398
3000	0.5	DMA	40	15	100	521.6

**Table SD.2.1.** Cluster sizes for different silica powders sonicated at a variety of intensities and times. 100 % sonication intensity corresponds to a maximum power output of 600 W. PEG denotes Polyethyleneglycol (400 Mw).

#### **SD.2.4.Demixing front propagation rate**

Precipitated front propagation rates were obtained from the slopes of front thickness as a function of the square root of time plots, as shown in Fig. SD.2.3. The thickness of the propagating front at different times was obtained using Olympus FluoView<sup>TM</sup> FV1000 dedicated software.



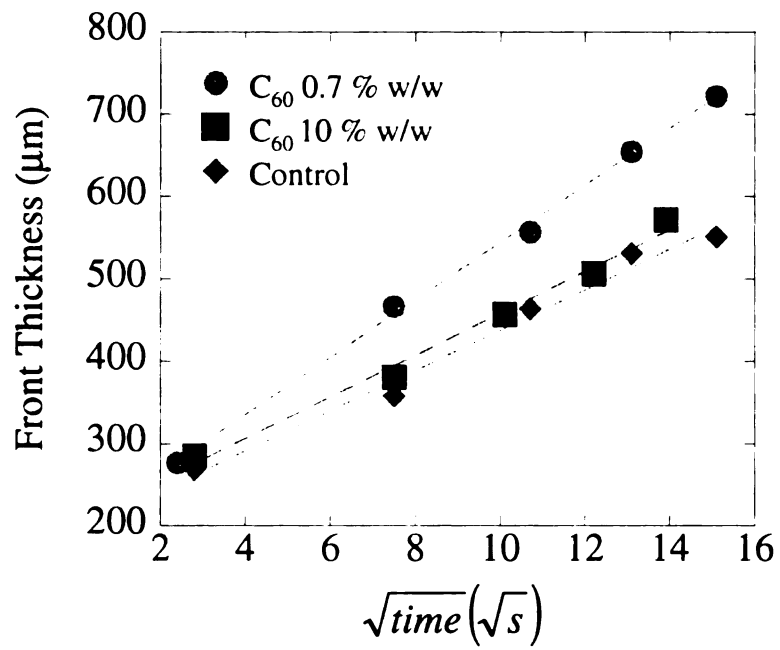


**Figure SD.2.3.** Front thickness vs. the square root of time plots for 0, 0.7 and 10 %  $\text{C}_{60}$  loading casting mixtures.

## References

1. L. Brunet, D. Y. Lyon, K. Zodrow, J. C. Rouch, B. Caussat, P. Serp, J. C. Remigy, M. R. Wiesner and P.J. J. Alvarez, Properties of membranes containing semi-dispersed carbon nanotubes, *Environ. Eng. Sci.* 25 (2008) 565-575.
2. K. Ebert, D. Fritsch, J. Koll and C. Tjahjaviguna, Influence of inorganic fillers on the compaction behaviour of porous polymer based membranes, *J. Membr. Sci.* 233 (2004) 71-78.
3. J. B. Li, J. W. Zhu and M. S. Zheng, Morphologies and properties of poly(phthalazinone ether sulfone ketone) matrix ultrafiltration membranes with entrapped TiO<sub>2</sub> nanoparticles, *J. Appl. Polym. Sci.* 103 (2006) 3623-3629.
4. S. P. Nunes, K. V. Peinemann, K. Ohlrogge, A. Alpers, M. Keller and A. T. N. Pires, Membranes of poly(ether imide) and nanodispersed silica, *J. Membr. Sci.* 157 (1999) 219-226.
5. W. K. Son, J. H. Youk, T. S. Lee and W. H. Park, Preparation of antimicrobial ultrafine cellulose acetate fibers with silver nanoparticles, *Macromol. Rapid Commun.* 25 (2004) 1632-1637.
6. N. M. Wara, L. F. Francis and B. V. Velamakanni, Addition of alumina to cellulose acetate membranes, *J. Membr. Sci.* 104 (1995) 43-49.
7. L. Yan, Y. S. Li, C. B. Xiang and S. Xianda, Effect of nano-sized Al<sub>2</sub>O<sub>3</sub>-particle addition on PVDF ultrafiltration membrane performance, *J. Membr. Sci.* 276 (2006) 162-167.
8. Y. Yang, H. Zhang, P. Wang, Q. Zheng and J. Li, The influence of nano-sized TiO<sub>2</sub> fillers on the morphologies and properties of PSF UF membrane, *J. Membr. Sci.* 288 (2007) 231-238.
9. M. Mulder, *Basic Principles of Membrane Technology*. Second ed. 2003, Dordrecht, Netherlands: Kluwer Academic.
10. P. J. Flory, *Principles of Polymer Chemistry*. 1953, New York: Cornell Univ. Press.
11. C. M. Tam, T. A. Tweddle, O. Kutowy and J. D. Hazlett, Polysulfone membranes. II. Performance comparison of polysulfone-poly(N-vinyl-pyrrolidone) membranes, *Desalination* 89 (1993) 275-287.
12. T.A. Tweddle, O. Kutowy, W. L. Thayer and S. Sourirajan, Polysulfone ultrafiltration membranes, *Ind. Eng. Chem. Prod. Res. Dev.* 22 (1983) 320-326.

13. P. van de Witte, P. J. Dijkstra, J. W. A. van den Berg and J. Feijen, Phase separation processes in polymer solutions in relation to membrane formation, *J. Membr. Sci.* 117 (1996) 1-31.
14. R. M. Boom, I. M. Wienk, Th. van den Boomgaard and C. A. Smolders, Microstructures in phase inversion membranes. Part 2. The role of a polymeric additive, *J. Membr. Sci.* 73 (1992) 277-292.
15. B. Chakrabarty, A. K. Ghoshal and M. K. Purkait, Preparation, characterization and performance studies of polysulfone membranes using PVP as an additive, *J. Membr. Sci.* 315 (2008) 36-47.
16. A. Idris and L. K. Yet, The effect of different molecular weight PEG additives on cellulose acetate asymmetric dialysis membrane performance, *J. Membr. Sci.* 280 (2006) 920-927.
17. J. H. Kim and K. H. Lee, Effect of PEG additive on membrane formation by phase inversion, *J. Membr. Sci.* 138 (1998) 153-163.
18. S. R. Kim, K. H. Lee and M. S. Jhon, The effect of ZnCl<sub>2</sub> on the formation of polysulfone membrane, *J. Membr. Sci.* 119 (1996) 59-64.
19. Q. Z. Zheng, P. Wang and Y. N. Yang, Rheological and thermodynamic variation in polysulfone solution by PEG introduction and its effect on kinetics of membrane formation via phase-inversion process, *J. Membr. Sci.* 279 (2006) 230-237.
20. P. Aerts, I. Genne, S. Kuypers, R. Leysen, I. F. J. Vankelecom and P. A. Jacobs, Polysulfone-aerosil composite membranes: Part 2. The influence of the addition of aerosil on the skin characteristics and membrane properties, *J. Membr. Sci.* 178 (2000) 1-11.
21. P. Aerts, E. Van Hoof, R. Leysen, I. F. J. Vankelecom and P. A. Jacobs, Polysulfone-aerosil composite membranes: Part 1. The influence of the addition of Aerosil on the formation process and membrane morphology, *J. Membr. Sci.* 176 (2000) 63-73.
22. W. L. Chou, D. G. Yu and M. C. Yang, The preparation and characterization of silver-loading cellulose acetate hollow fiber membrane for water treatment, *Polym. Adv. Technol.* 16 (2005) 600 - 607.
23. J. S. Taurozzi, H. Arul, V. Z. Bosak, A. F. Burban, T. C. Voice, M. L. Bruening and V. V. Tarabara, Effect of filler incorporation route on the properties of polysulfone-silver nanocomposite membranes of different porosities, *J. Membr. Sci.* 325 (2008) 58-68.
24. G. Jonsson, Methods for determining the selectivity of reverse osmosis membranes, *Desalination* 24 (1977) 19-37.

25. K. M. Persson, V. Gekas and G. Tragardh, Study of membrane compaction and its influence on ultrafiltration water permeability, *J. Membr. Sci.* 100 (1995) 155-162.
26. J-H Choi, Jonggeon Jegal and W-N Kim, Fabrication and characterization of multi-walled carbon nanotubes/polymer blend membranes, *J. Membr. Sci.* 284 (2006) 406-415.
27. A. J. Reuvers, J. W. A. van den Berg and C. A. Smolders, Formation of membranes by means of immersion precipitation. Part I. A model to describe mass transfer during immersion precipitation, *J. Membr. Sci.* 34 (1987) 45-65.
28. A. J. Reuvers and C. A. Smolders, Formation of membranes by means of immersion precipitation. Part 2. The mechanism of formation of membranes prepared from the system cellulose acetate–acetone–water, *J. Membr. Sci.* 34 (1987) 67-86.
29. J. L. White and J. W. Crowder, The influence of carbon black on the extrusion characteristics and rheological properties of elastomers: Polybutadiene and butadiene-styrene copolymer, *J. Appl. Polym. Sci.* 18 (1974) 1013-1038.
30. V. Pryamitsyn and V. Ganesan, Mechanisms of steady-shear rheology in polymer nanoparticle composites, *J. Rheol.* 50 (2006) 655-683.
31. J. F. Douglas and F. W. Starr, Origin of particle clustering in a simulated polymer nanocomposite and its impact on rheology, *J. Chem. Phys.* 119 (2003) 1777-1788.
32. J. Lee and H. H. Kim, Effect of encapsulating agents on dispersion status and photochemical reactivity of C60 in the aqueous phase, *Environ. Sci. Technol.* 42 (2008) 1552-1557.
33. V. C. Moore, M. S. Strano, E. H. Haroz, R. H. Hauge and R. E. Smalley, Individually suspended single-walled carbon nanotubes in various surfactants, *Nano Lett.* 3 (2003) 1379-1382.
34. J. P. DeRocher, B. T. Gettelfinger, J. Wang, E. E. Nuxoll and E. L. Cussler, Barrier membranes with different sizes of aligned flakes, *J. Membr. Sci.* 254 (2005) 21-30.
35. E. L. Cussler, S. E. Hughes, W. J. Ward and R. Aris, Barrier membranes, *J. Membr. Sci.* 38 (1988) 161-174.
36. D. M. Eitzman, R. R. Melkote and E. L. Cussler, Barrier membranes with tipped impermeable flakes, *AIChE Journal* 42 (1996) 2-9.
37. C. Yang, W. H. Smyrl and E. L. Cussler, Flake alignment in composite coatings, *J. Membr. Sci.* 231 (2004) 1-12.
38. N. K. Lape, E. E. Nuxoll and E. L. Cussler, Polydisperse flakes in barrier films, *J. Membr. Sci.* 236 (2004) 29-37.

39. J. Lu, I. Do, L. T. Drzal, R. M. Worden and I. Lee, Nanometal-decorated exfoliated graphite nanoplatelet based glucose biosensors with high sensitivity and fast response, *Acs Nano* 2 (2008) 1825-1832.
40. K. Kalaitzidou, H. Fukushima and L. T. Drzal, A new compounding method for exfoliated graphite-polypropylene nanocomposites with enhanced flexural properties and lower percolation threshold, *Compos. Sci. Technol.* 67 (2007) 2045-2051.

## CHAPTER THREE

### **Effect of filler incorporation route on the properties of polysulfone-silver nanocomposite membranes of different porosities**

Published in

*Journal of Membrane Science*

Volume 325, 2008, pages 58-68

by

Julian S. Taurozzi<sup>†</sup>, Hari Arul<sup>||</sup>, Volodymyr Z. Bosak<sup>‡</sup>, Anatoliy F. Burban<sup>‡</sup>, Thomas C. Voice<sup>†</sup>, Merlin L. Bruening<sup>‡</sup>, and Volodymyr V. Tarabara<sup>†</sup>

<sup>†</sup> Department of Civil and Environmental Engineering, Michigan State University, East Lansing, MI 48824, USA

<sup>||</sup> High School Honors Science, Mathematics, Engineering Program, Michigan State University

<sup>‡</sup> Department of Chemistry, The National University of "Kyiv-Mohyla Academy", 2, Skovoroda St., Kyiv, 04070, Ukraine

<sup>‡</sup> Department of Chemistry, Michigan State University, East Lansing, MI 48824, USA

## **CHAPTER THREE**

### **Effect of filler incorporation route on the properties of polysulfone-silver nanocomposite membranes of different porosities**

#### **Abstract**

Flat sheet porous polysulfone-silver nanocomposite membranes were synthesized by the wet phase inversion process. The effects of casting mixture composition and nanoparticle incorporation route on the morphological and separation properties of prepared membranes were studied by comparing nanocomposites of different preparations with silver-free controls. Silver nanoparticles were either synthesized ex-situ and then added to the casting solution as an organosol or produced in the casting solution via in-situ reduction of ionic silver by the polymer solvent. Nanocomposite membranes of three types differing in skin porosity and macrovoid structure were prepared. The structure and properties of nanocomposites were interpreted in terms of the coupling between the processes of nanoparticle formation and gelling of the polymer-rich phase during phase inversion. Larger nanoparticles preferentially located in the skin layer were observed in composites prepared via the ex-situ method while in-situ reduction of silver led to formation of smaller nanoparticles homogeneously distributed along the membrane cross section. In some cases, incorporation of nanoscale silver formed ex-situ resulted in macrovoid widening and an order of magnitude decrease in hydraulic resistance accompanied by only a moderate decrease in rejection. The accessibility of the silver nanoparticles embedded in the membrane was quantitatively assessed by the degree of the growth inhibition of a membrane biofilm due to the ionic silver released by the nanocomposites and was found to depend on the method of silver incorporation.

### 3.1 Introduction

Porous polymer nanocomposite membranes can be prepared using a number of nanoparticle incorporation strategies. These strategies can be grouped into four categories based on whether particles and membranes are pre-formed or synthesized in-situ during the formation of the nanocomposite. Methods that involve attachment or in-situ synthesis of nanoparticles on the pore surface of *existing* membranes [1-7] have the advantages of improved reproducibility of nanocomposite preparation, the possibility to reuse the membrane matrix or to regenerate nanoparticles, and better accessibility of immobilized nanoparticles to reactants in the permeate flow. In contrast, incorporation of nanoparticles during membrane formation [8-21] is appealing because it should allow the design of nanocomposite structures with improved mechanical and separation properties along with embedded nanoparticle-based functionalities. The structure of the resulting membranes is generally a function of the physical and chemical properties of the polymer matrix and nanoparticles as well as the method of nanoparticle incorporation.

A number of published studies describe the formation of organic-inorganic porous (10 kDa to 200 kDa) composite membranes by adding particles ( $\text{Al}_2\text{O}_3$  [18, 19],  $\text{ZrO}_2$  [11, 14],  $\text{TiO}_2$  [15, 20],  $\text{SiO}_2$  [8, 9, 12, 22],  $\text{Ag}^0$  [13, 21, 23]) to the solution of the membrane-forming polymer (cellulose acetate (CA) [13, 18, 23], polysulfone (PSf) [8, 9, 14, 17, 20], polyvinylidene fluoride (PVDF) [11, 12, 19], polyacrylonitrile (PAN) [21], polyamide-imide (PAI) [24], poly(vinylidene fluoride-co-hexafluoropropylene) [22], or

poly(phthalazinone ether sulfone ketone) (PPESK) [15]). These studies indicate that skin layer properties (porosity, surface porosity, thickness) as well as the macrovoid morphology of the support layer can be affected by nanoparticle incorporation. Both of these membrane regions are important; the skin layer determines the permeability, rejection, and selectivity of membranes, while the structure of the support layer affects its compaction behavior [25, 26]. Although nanoparticle-induced changes in membrane structure are specific to the particular filler/matrix combination, certain common trends can be identified. Increasing nanoparticle loading led to: (1) increased skin layer thicknesses ( $\text{SiO}_2/\text{PSf}$  [8, 9],  $\text{TiO}_2/\text{PSf}$  [20],  $\text{TiO}_2/\text{PPESK}$  [15]), (2) higher surface porosity of the skin ( $\text{ZrO}_2/\text{PSf}$  [14],  $\text{TiO}_2/\text{PSf}$  [20],  $\text{TiO}_2/\text{PPESK}$  [15],  $\text{SiO}_2/\text{PSf}$  [9]), (3) suppressed macrovoid formation ( $\text{SiO}_2/\text{PSf}$  [8, 9],  $\text{TiO}_2/\text{PSf}$  [20],  $\text{Al}_2\text{O}_3/\text{CA}$  [18],  $\text{TiO}_2/\text{PPESK}$  [15]) and (4) higher permeability of the membrane ( $\text{ZrO}_2/\text{PSf}$  [14],  $\text{SiO}_2/\text{PVDF}$  [12],  $\text{ZrO}_2/\text{PVDF}$  [11],  $\text{Al}_2\text{O}_3/\text{PVDF}$  [19],  $\text{Ag}/\text{CA}$  [13],  $\text{SiO}_2/\text{PSf}$  [9],  $\text{TiO}_2/\text{PSf}$  [20]. In a few cases, decreased ( $\text{Ag}/\text{PAN}$  [21]) permeability or a maximum permeability at intermediate nanoparticle loadings ( $\text{TiO}_2/\text{PPESK}$  [15]) was also reported. The rejection either peaked at intermediate loadings ( $\text{TiO}_2/\text{PSf}$  [20]), or decreased after a threshold in filler loading was exceeded ( $\text{SiO}_2/\text{PSf}$  [9],  $\text{SiO}_2/\text{PVDF}$  [12],  $\text{ZrO}_2/\text{PVDF}$  [11],  $\text{TiO}_2/\text{PPESK}$  [15]), or remained unchanged ( $\text{ZrO}_2/\text{PSf}$  [14],  $\text{Al}_2\text{O}_3/\text{PVDF}$  [19]). In a recent study, nanotube fillers were used to prepare a nanocomposite membrane when polysulfone was embedded with (acid-treated) multiwall carbon nanotubes [27]. The average porosity of the composite membranes peaked at a nanotube loading of 1.5%,

which also corresponded to the highest permeate flux. Interestingly, the only pronounced change in membrane macroscopic morphology was an increase in surface roughness.

Examples of simultaneous formation of the polymer matrix and the nanoparticles include chemical reduction of metal ions by a component of the membrane casting solution [13, 21, 28]. Bhattacharyya et al. reported on the formation of Fe/Ni nanoparticles in porous cellulose acetate membranes by in-situ reduction wherein the reducing agent ( $\text{NaBH}_4$ ) was a component of the non-solvent bath [28]. Yu et al. prepared silver-loaded cellulose acetate and polyacrylonitrile hollow fibers by the reduction of  $\text{Ag}^+$  by *N,N*-dimethylformamide, a polymer solvent, with the objective of producing biofouling-resistant ultrafiltration membranes [13, 21].

The results of the studies published to-date strongly imply that the microstructural changes induced by nanoparticle incorporation can potentially be controlled to prepare membranes with desirable properties. To enable the rational design of porous nanocomposite membranes, the role of essential process variables such as nanofiller size (relative to the characteristic size of matrix pores), the affinity of the filler material for the components of the casting mixture, and the effect of the matrix pores functioning as reactors for forming filler nanoparticles need to be understood. The overall goal of our research was to understand how the preparation condition (nanoparticle incorporation route, porosity of the host matrix, etc) influence the structure of the prepared nanocomposite membranes. To this end, we attempted to map nanocomposite membrane

properties to preparation conditions for a series of membrane morphologies and two nanoparticle incorporation routes. Three types of membranes differing in skin porosity and macrovoid structure were prepared, and silver nanoparticles were either synthesized ex-situ and then added to the casting solution as an organosol or produced in the casting solution via in-situ reduction of ionic silver during the phase inversion process.

Polysulfone was chosen as the matrix material due to its practical importance and wide use in the preparation of ultrafiltration membranes, while nanoscale silver was chosen for two reasons. First, there are established protocols for the preparation and characterization of silver sols in various dispersion media, including the organic solvents used in membrane preparation. Second, the presence and availability of silver can be detected by the extent of its antibacterial effect; this provides a convenient framework for the evaluation of the accessibility of silver in polymer matrices and serves as additional motivation in view of the potential application of silver-filled nanocomposites as biofouling-resistant materials.

## **3.2 Experimental**

### **3.2.1 Materials**

Silver nitrate (GR ACS crystals), N,N-dimethylformamide (99.8% anhydrous), N,N-dimethylacetamide (99.8% anhydrous), polyethylene glycol (MW avg. 400), 2-propanol (99.5%) and polysulfone (Udel P-3500 LCD pellets, MB8, 79 kDa) were all used as received. The ultrapure water used in all experiments was supplied by a commercial ultrapure water system equipped with a terminal 0.2  $\mu\text{m}$  capsule microfilter; the resistivity of water was greater than 16  $\text{M}\Omega\text{-cm}$ . The standard constituents of the Luria-Bertani (LB) medium and agar plates used for bacteria incubation were purchased from Difco Laboratories. *Escherichia coli* cell lysing agent, (B-PER), bovine serum albumin protein assay standards, and Bradford assay reagents were all purchased from Pierce Biotechnology and used according to the manufacturer's guidelines. For the measurements of the molecular weight cut-off of prepared membranes, 150 kDa dextran (DIN certified standard) was purchased from Sigma-Aldrich. Reagents used for ICP-MS analysis were ultra-pure nitric acid and single-element plasma grade standards in 1% nitric acid.

### **3.2.2 Preparation of polysulfone membranes**

All membranes were prepared by the wet phase inversion process wherein cast films of polysulfone (PSf) dissolved in a mixture of N,N-dimethylacetamide (DMAC) and

dimethylformamide (DMF) were immersed in a non-solvent with respect to polysulfone. DMAC served as the primary polymer solvent while DMF acted as the reducing agent for silver. To explore the effect of matrix porosity on the distribution and accessibility of filler nanoparticles, three membrane preparation protocols were adapted to produce membranes with different porosities. Membranes of three distinct types (Types I, II, and III) were obtained by varying the composition of the casting mixture and the composition and temperature of the non-solvent in the immersion bath (Table 1). Either polyethylene glycol (PEG) or 2-propanol was added to the casting mixture as a pore forming agent (porogen), and either water or propanol was used as the non-solvent medium.

PSf Type I membranes were prepared according to a known procedure [29-32], where DMAC or DMF are used as solvents for polysulfone. PEG was added to the casting mixture to increase the porosity of the cast membrane while maintaining a high polymer content (15% to 20%) and, therefore, sufficiently high viscosity ( $\geq 104$  cps) of the casting mixture [33-35]. To prepare Type I membranes, polysulfone pellets were suspended in a DMAC/DMF/PEG solution and left to dissolve overnight in an oven at 100 °C. The vial with the polymer solution was sealed to prevent solvent evaporation. Upon complete dissolution of the polymer, the resulting viscous solution was homogenized by mixing on a hot plate and was cast as a thin film on a 25 cm x 30 cm flat glass support using a micrometric film applicator (model 3570, Elcometer Inc., Rochester Hills, MI). All of the cast films had a drawdown thickness of  $(300 \pm 1)$   $\mu\text{m}$ , which was ensured by adjusting the applicator's outlet film gap with a micrometric screw.



Component	Membrane					
	PSf I	PSf II	PSf III	PSf/Ag I	PSf/Ag II	PSf/Ag III
PSf, %	19.97	10.08	10.12	19.20	9.88	9.92
DMAC, %	45.04	70.78	60.87	43.32	69.38	59.66
DMF, %	18.97	19.14	19.22	18.24	18.76	18.84
PEG, %	16.02	---	---	15.40	---	---
2-propanol, %	---	---	9.79	---	---	9.59
AgNO <sub>3</sub> , %	---	---	---	3.84	1.98	1.98

**Table 3.1.**Components of membrane casting mixture (% mass)

Immediately after casting, the film was immersed in a room-temperature water bath to induce phase inversion. Free standing membrane sheets were thoroughly rinsed with DI water to allow for complete solvent removal.

To prepare more porous Type II membranes, the above procedure was modified in the following manner: (1) the polysulfone content in the casting mixture was decreased by a factor of ca. 2, (2) no porogen was used, and (3) the temperature of the water in the immersion bath was raised to 70 °C.

To prepare Type III membranes, which are the most porous, the procedure used to prepare Type I membranes was modified as follows: (1) the polysulfone content in the casting mixture was decreased by a factor of ca. 2, (2) 2-propanol instead of PEG was used as the pore forming agent, and (3) 2-propanol (room temperature) was used instead of water as the non-solvent.

### **3.2.3 Preparation of polysulfone-silver nanocomposite membranes**

We adopted two silver incorporation approaches. In the first approach, Ag nanoparticles were synthesized ex-situ and were added to the casting solution as a Ag-DMF organosol.

The organosol was prepared by adding AgNO<sub>3</sub> to 5 mL DMF (reducing agent for silver) and heating the solution under intense stirring to allow for nanoparticle formation [36].

**The** obtained organosol was then added to the casting mixture, containing DMA, PSf and **a p**orogen.

The second approach involved an in-situ reduction of ionic  $\text{Ag}^+$  by DMF in the membrane casting mixture. In this case,  $\text{AgNO}_3$  was first dissolved in DMF at room temperature to minimize Ag reduction. The polymer solution was subjected to intense stirring under heating; once the casting mixture became homogeneous, the  $\text{AgNO}_3/\text{DMF}$  solution was added to it to initiate the reduction of silver ions to  $\text{Ag}^0$  with the concomitant formation of silver nanoparticles. Reduction was allowed to proceed for 1 min prior to casting the membrane.

Membranes prepared by these two approaches will be denoted as  $\text{PSf}/\text{Ag}^{\text{ex}}$  (Type) and  $\text{PSf}/\text{Ag}^{\text{in}}$  (Type), respectively, where “Type” is one of the three casting mixture compositions described earlier: Type I, Type II, or Type III. While the amount of polysulfone in  $\text{PSf}/\text{Ag}$  Type II and  $\text{PSf}/\text{Ag}$  Type III membranes was half of that in the  $\text{PSf}/\text{Ag}$  Type I membranes, the Ag-to-PSf mass ratio was adjusted to remain constant in all preparations (Table 1).

#### **3.2.4 Characterization of membranes: SEM, TEM, EDS, FTIR, XPS**

A Hitachi S-4700II Field Emission scanning electron microscope operated in ultra high resolution mode was used to record SEM images. The transmission electron microscope used for TEM/EDS characterization was a JEM-2200FS with field emission gun operation at 200 kV and a point resolution of 0.19 nm; images were taken using a Gatan 794 MSC digital camera. The instrument was equipped with an X-ray energy dispersive *spectroscopy* (X-EDS) system (Oxford Instruments) with an optimal energy resolution of

140 eV. SEM and TEM sample preparation procedures are described in the Supporting Documentation file.

XPS measurements of Ag-modified membranes were carried out using a PHI 5400 ESCA system (Physical Electronics, Chanhassen, MN) equipped with a non-monochromatic Mg X-ray. In all measurements a take-off angle of 45° was used.

Transmission ATR-FTIR measurements were performed using a Nicolet Magna-IR 550 spectrometer at a rate of 16 scans per second with a resolution of 1.928 cm<sup>-1</sup>. Omnic software was used to control spectral acquisition and to process the acquired data.

### **3.2.5 Permeability and rejection tests**

The hydraulic resistance of membranes was measured using a stirred Amicon 8010 dead-end ultrafiltration cell (Millipore Corp, Billerica, MA) connected to a pressurized container (100 psi, 5L, Alloy Products Corp., Waukesha, WI) filled with ultrapure water. Prior to each test, the membrane coupons were compacted until a steady permeate flow was attained. The permeate flux was measured continuously by collecting the filtered water on a digital balance (AV8101C, Ohaus Corp., Pine Brook, NJ) interfaced with a computer via an RS-232 port. The data from the balance were logged to a computer using a program written in LabView (version 7.1, National Instruments).

To eval

filtered

Dextra

analyz

blanks

**3.2.6**

The le

conce

Varia

Photo

conta

ionic

organ

durin

10%

To m

water

for fo

Parma

8010

To evaluate membrane rejection, 20 mg/L aqueous solutions of 150 kDa dextran were filtered through the compacted membranes using the same dead-end filtration system. Dextran concentration in the permeate was determined using a total organic carbon analyzer (model 1010, OI Analytical, College Station, TX). Calibration standards and blanks were run for each set of measurements.

### **3.2.6 Measuring silver losses**

The loss of silver during membrane preparation was assessed by measuring its concentration in the non-solvent immersion bath by atomic absorption (Spectra AA 200, Varian Inc., Palo Alto, CA) with a hollow cathode Ag lamp at 328.1 nm (Hamamatsu Photonics, Japan). All of the analyzed samples, calibration blanks, and Ag standards contained 2% HNO<sub>3</sub> v/v to ensure the complete oxidation of nanoparticulate silver to its ionic, soluble form. Calibration standards and blanks were doped with 100 µL of the organic solvent to mimic the chemical makeup of the solution in the immersion bath during membrane casting. In all cases, silver losses to the immersion bath were below 10% of the silver added to the casting mixture.

To measure the amount of silver leached from the membranes during filtration, ultrapure water was circulated continuously through Type III PSf/Ag<sup>in</sup> and PSf/Ag<sup>ex</sup> membranes for four consecutive days. A variable flow rate gear pump (model EW-74013-20, Cole-Parmer, Vernon Hills, IL) was used to deliver the feed water (50 mL) into the Amicon 8010 filtration cells containing the membranes. The permeate flux was directed back into

the feed vessel. Samples (2 mL) of the circulated water were collected every 24 hr for the 4-day period. The permeate samples were then analyzed for silver content with a Micromass (Thermo Electron Corporation) Platform quadrupole ICP-MS with a hexapole collision cell using a concentric nebulizer with water-cooled spray chamber and a CECTAC ASX-500 autosampler. Final sample concentrations were quantified using a set of single-element external calibration standards to enable measurements in the (0 to 2.5) ppb concentration range.

### **3.2.7 Membrane biofouling characterization**

Antibacterial properties of nanocomposite membranes were quantitatively assessed using the Bradford protein assay [37, 38]. Two-sample t-test analysis was performed to assess the statistical significance of the observed differences in antibacterial activity (see Supporting Documentation (SD) file for tables with t values).

#### *3.2.7.1 Biofilm growth inhibition under diffusive conditions*

The *E. coli* culture for membrane inoculation was grown overnight to achieve an optical density (OD<sub>600</sub>) of 0.4. This suspension was then diluted 1:100 in LB medium and 2 mL of this suspension was filtered through membranes. The fouled membranes were placed on an agar LB plate (feedside up) for incubation at 37 °C for 48 hr. After incubation, the fouled membranes were cut in thirds, each coupon was immersed into 1 mL of a 1:1 B-PER:water protein extraction solution to allow for cell disruption and protein

solubilization, and the mixture was then vortexed for ca. 1 min. The liquid phase was then centrifuged for 1 hr using an Adams compact II centrifuge (Becton Dickinson, Franklin Lakes, NJ) with a 6-place angle rotor at a fixed speed of 3,200 rpm, and the supernatant containing soluble proteins was decanted. Finally, 50  $\mu$ L of the obtained solution was dissolved in 1.5 mL of Bradford reagent to be analyzed using UV-Vis spectrophotometry. The intensity of the 595 nm peak in the absorption spectrum was recorded using the Bradford software module of a NanoDrop ND-1000 UV-Vis spectrophotometer (NanoDrop Technologies, Wilmington, DE) equipped with a Xenon flash lamp light source and a 2048-element linear silicon CCD detector. Measurements were performed in 10 s cycles with a wavelength resolution of 3 nm and an absorbance precision of 0.003. The calibration curve for protein quantification was obtained using BSA protein standards dissolved in the same solvent as that used for the measured samples (1:1 B-PER:water); this solvent was also used to record the measurement baseline. In control experiments with biofilm-free nanocomposites, the peak at 595 nm was not detected, which confirmed that there were no interferences due to silver. Triplicate results for each membrane type were obtained by analyzing three separate areas of each membrane, and the protein values were normalized by the area of the tested membrane sample. For each nanocomposite, its silver-free counterpart was used as the comparative basis. In all cases the amount of bacteria deposited both on the membrane surface and inside the membrane pores during filtration was negligible with respect to the amount subsequently grown during incubation.

#### *3.2.7.2 Biofilm growth inhibition under convective conditions*

To assess the performance of the nanocomposites under filtration conditions, filtration tests were conducted using an Amicon 8010 dead-end ultrafiltration cell (Millipore Corp, Billerica, MA). The convective flow tests were conducted for Type I PSf/Ag<sup>ex</sup>, PSf/Ag<sup>in</sup>, and PSf (control) membranes by continuously filtering LB medium through inoculated membranes for 48 hr. The inoculation (initial flow of 2 mL of bacteria solution through the membrane) and quantification procedures were conducted as explained in the previous section, but bacteria were grown while filtering LB broth rather than on an agar plate.

### *3.2.7.3 Assessment of silver leaching*

Silver leaching was assessed by filtering ultrapure water through nanocomposite membranes and quantifying the antibacterial effect of the permeate using the Bradford assay. In these tests, 10 mL of ultrapure water was first filtered through PSf/Ag<sup>in</sup> Type I nanocomposites. 9 mL of the obtained permeate was mixed with 1 mL of pre-concentrated (10x) liquid LB medium, and continuously filtered through an inoculated silver-free membrane for 24 hr.

For each nanocomposite sample, two 9 mL permeate samples were collected: one after the first day and another one after the second day of continuous filtration. After each day, biofilm growth on PSf membranes was quantified using the Bradford assay. The accumulated 48 hr growth was then calculated from the obtained results. Given that the

concentration of silver in the leachate collected for 2 days under convective conditions was already close to the detection limit of ICP-MS technique (see Results section), and considering that the intended effect of silver was biofouling mitigation, the degree of inhibition of the biofilm growth on these membranes was a convenient and appropriate surrogate measure of the silver content of the leachate.

### **3.3. Results and Discussion**

#### **3.3.1 Silver-free polysulfone membranes**

Three strategies were used to prepare more porous PSf membranes of Types II and III: a) decreasing the polymer content of the casting mixture, b) increasing the temperature of the non-solvent bath, and c) altering the composition of the non-solvent bath (Table 1). Relative to the Type I system, the polymer content of the casting solutions was decreased by a factor of 2 for both Type II and Type III membranes. The viscosity of the casting mixture has a direct influence on the gelation rate of the membranes [33, 35, 39] as the solvent/non-solvent exchange in lower viscosity mixtures proceeds faster, allowing for the formation of more porous materials. For the PSf Type II membranes no porogens were added; instead, the temperature of the non-solvent bath was increased to hasten the onset of demixing and produce a higher porosity structure [33].

For the PSf Type III membranes, 2-propanol (weak non-solvent) was added as a porogen to the casting mixture to bring it closer to the limit of its polymer solubility and to induce instantaneous demixing at lower polymer content thereby producing more porous membranes. 2-Propanol was used instead of water as the less effective non-solvent in the immersion bath to synergistically retard gel formation and further increase the porosity. By weakening the non-solvent character of the immersion bath, the coagulation process develops as a gradual, less abrupt transition, allowing for the formation of a more porous membrane [31, 33].

3.3.

The

of l

into

men

low

3.3.

fee

ord

3.3.

Silv

cell

inve

the c

3.1

could

of dir

Fig.

### *3.3.1.1 Surface morphology*

The surface of the silver-free PSf Type I membranes was of low porosity with pore sizes of less than 10 nm (Fig. 3.1 a). Type II membranes showed a more porous skin, with interconnected surface pores 30 nm to 100 nm in size (Fig. 3.1 b). In Type III membranes, well-defined, larger pores with the typical pore size of 0.5  $\mu\text{m}$  and with lower surface density were observed (Fig. 3.1 c). In some experiments (see section 3.3.3.1), the opposite (i.e. more porous) side of the PSf Type II membranes faced the feed. SEM imaging of this surface showed a macroporous structure, with pores on the order of 20  $\mu\text{m}$  to 50  $\mu\text{m}$  in diameter and of regular shape (Inset A, Fig. 3.1 b).

### *3.3.1.2 Cross-sectional morphology*

Silver-free membranes of all three types had the asymmetric porous structure, with both cellular pores and macrovoids typical of polysulfone membranes prepared by phase inversion. In PSf Type I membranes, tear-shaped elongated macrovoids extended from the ca. 25  $\mu\text{m}$ -thick lower porosity layer towards the permeate side of the membrane (Fig. 3.1 d). In Type II and III membranes, a more pronounced cross-sectional asymmetry could be observed. In the PSf Type II membranes, a hierarchy of three macrovoid types of dimensions increasing with the distance away from the membrane skin was observed (Fig. 3.1 e). In PSf Type III membranes, the elongated narrower macrovoids quickly

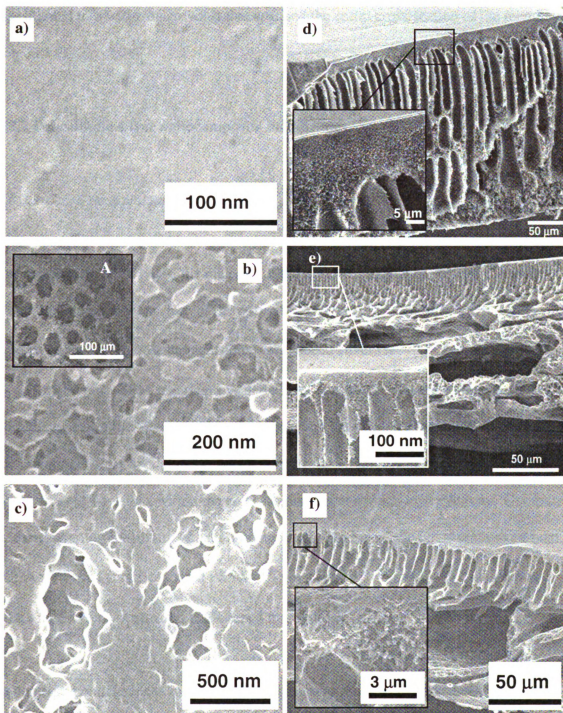


**Figure 3.1.** SEM surface (a, b, c) and cross-section (d, e, f) images of PSf Type I (a, d), Type II (b, e) and Type III (c, f) membranes. Inset A shows the permeate side surface of PSf Type II membranes.

transitioned into wider macrovoids that spanned the entire cross-section of the membrane (Fig. 3.1 f).

### **3.3.2 Polysulfone-silver nanocomposite membranes**

#### *3.3.2.1 Cross-sectional morphology*

For membranes of all types, the majority of the observed nanoparticles were located along the internal pore surface of the polymeric matrix (Fig. 3.1). TEM EDS results confirmed that the nanoscale inclusions were indeed silver (see SD). For the PSf/Ag<sup>ex</sup> Type I membrane, SEM imaging revealed a high density of crystalline silver particles with diameters in the 50 nm to 500 nm range along the skin area but nowhere else along the membrane cross-section (Fig. 3.1 c); smaller (less than 50 nm) nanoparticles were observed at all locations within the cross-section but at a much lower density. Compared to corresponding membranes containing no silver (Fig 3.1 a), the cross-sections of both PSf/Ag<sup>ex</sup> Type I (Fig. 3.2 c) and PSf/Ag<sup>in</sup> Type I (Fig. 3.2 b) nanocomposites showed wider macrovoids of stressed tear-shaped morphology.

In contrast, no differences in cross-sectional morphologies were observed upon silver modification for the Type II (Fig. 3.2 e and Fig. 3.2 f versus Fig. 3.2 d) and Type III (Fig. 3.2 h and Fig. 3.2 i versus Fig. 3.2 g) membranes, and no large (> 50 nm) silver crystals were detected along their cross-sections. However, silver nanoparticles in the 20 nm to 50 nm range were scattered throughout the entire cross-section of all of the silver modified

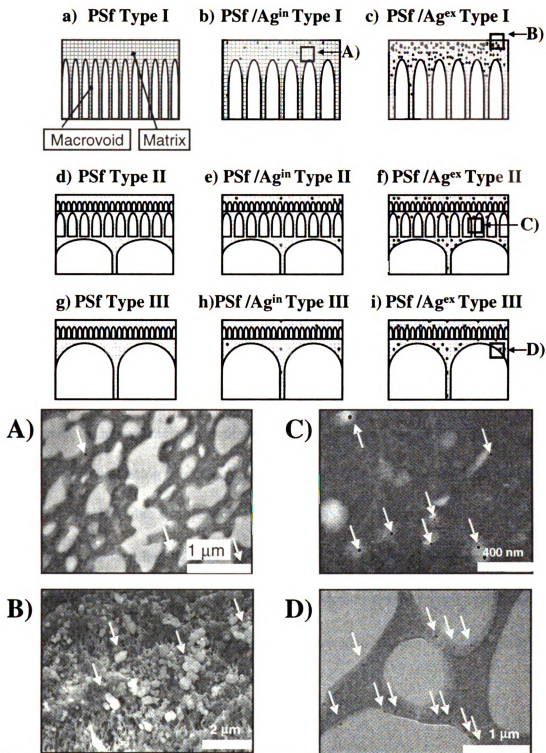


**Figure 3.2.** Schematic illustration of the distribution of silver nanoparticles in the silver-polysulfone nanocomposites prepared using different methods of silver incorporation. On micrographs, the black dots with arrows pointing to them correspond to silver nanoparticles. TEM micrographs (A, C and D) show membrane cross-sections, while SEM micrograph (B) shows the top cross section layer, with large silver clusters embedded into the polysulfone matrix.

membranes (Figures 3.2 A, 3.2 C, 3.2 D). While some nanoparticles in PSf/Ag<sup>ex</sup> membranes could be observed embedded within the polymer of the interpore walls, most nanoparticles were located along the pore surface (Fig 3.2 D). For all three membrane types, the ex-situ variations appeared to have a higher nanoparticle density with a relatively higher number of bigger nanoparticles than their in-situ counterparts. This difference between PSf/Ag<sup>ex</sup> and PSf/Ag<sup>in</sup> membranes could arise for several reasons: 1) longer reduction period for the silver in PSf/Ag<sup>ex</sup> nanocomposites; 2) pre-formed silver nanoparticles in PSf/Ag<sup>ex</sup> casting mixtures acting as nucleation sites for further nanoparticle growth; 3) limited silver availability for nanoparticle growth under conditions of developing porosity in PSf/Ag<sup>in</sup> cast films; and 4) a heterogeneous environment for nanoparticle formation in PSf/Ag<sup>in</sup> membranes wherein other components of the casting mixture could delay the nucleation and retard the growth of Ag<sup>0</sup>. The apparent higher nanoparticle densities observed in PSf/Ag<sup>ex</sup> membranes may also be due to the fact that the larger particles in the PSf/Ag<sup>ex</sup> composites are more readily observed. The total amount of silver was approximately the same in PSf/Ag<sup>ex</sup> and PSf/Ag<sup>in</sup> casting mixtures, and minimal Ag was detected in the non-solvent after casting.

### 3.3.2.2 Surface morphology

PSf/Ag Type I nanocomposite membranes showed a higher density of nanoscale surface pores as compared to their PSf Type I counterparts, with no significant overall differences in pore size between PSf/Ag<sup>ex</sup>, PSf/Ag<sup>in</sup> or PSf Type I membranes (Fig. 3.3).

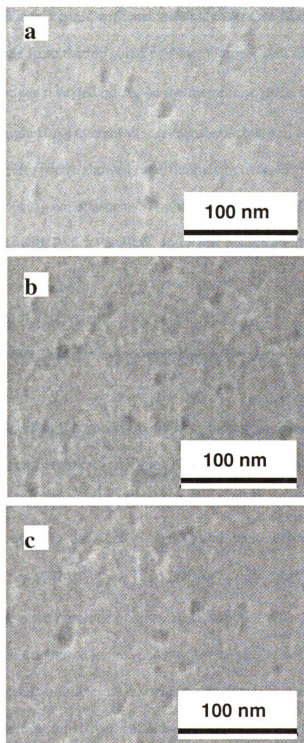


**Figure 3.3.** Representative SEM images of the surfaces of PSf Type I (a), PSf/Ag<sup>in</sup> Type I (b) and PSf/Ag<sup>ex</sup> Type I (c) membranes.

For PSf Type II and Type III membranes, there were no discernible differences in the SEM images of membranes prepared with and without silver (see SD). No silver particles were observed to protrude from the top surface of membranes, and XPS analysis of PSf/Ag<sup>ex</sup> Type I membranes revealed no Ag on the membrane surface. (The PSf/Ag<sup>ex</sup> Type I system had the highest Ag content of any membrane but still had no detectable silver on its surface.) FTIR spectra showed no difference between Type I membranes prepared with and without Ag nanoparticles. The above findings imply that the Ag does not form chemical bonds with PSf. XPS, EDS, and FTIR results are included in the SD file.

#### *3.3.2.3 Formation-structure links for nanocomposite membranes*

As illustrated in Fig. 3.2, silver incorporation did not produce visible macroscale morphological changes for membranes of Types II and III. For the less porous Type I membranes, the introduction of silver did induce macrovoid broadening along with an increase in surface porosity (Fig. 3.3); however, no significant morphological differences could be observed between PSf/Ag<sup>in</sup> Type I and PSf/Ag<sup>ex</sup> Type I membranes. These findings indicate that the mere presence of silver nanoparticles in the casting mixture, regardless of their size, is enough to induce changes in the morphology of the polymeric matrix for relatively dense membranes. We attribute this to an increase in the demixing rate in the forming membrane when nanoparticles are added to the casting solution. Because of faster demixing rates in the lower viscosity mixtures used to prepare Type II and Type III membranes, the effect of the filler was not noticeable. The absence of an

et

P

ar

ca

ln

P

h

la

3

tw

D

D

S

d

ce

c

D

P

P

Co

P

effect of Ag incorporation on the structure of Type II and Type III membranes could be partly due to the fact that the Ag loading in the casting solution was smaller for Type II and III membranes (Table 1). (The Ag/PSf ratio was constant, but less PSf was used in casting of Type II and III membranes).

In all cases, nanoparticles seemed to be preferentially concentrated along the internal pore surface (Insets A, C and D, Fig. 3.2), with PSf/Ag<sup>ex</sup> membranes showing apparent higher coverage densities, due to the fact that the ex-situ Ag incorporation approach gave larger nanoparticles. That PSf/Ag<sup>ex</sup> Type I membranes showed larger silver crystals (Fig. 3.2 B) concentrated in the denser top cross-section layer can be explained by noting that two opposing processes take place in the casting mixture: 1) nanoparticle formation via DMF-assisted reduction of ionic silver, and 2) nanoparticle re-dissolution into the DMAC, a component of the casting mixture that cannot reduce silver but can dissolve it. Such interplay between silver reduction and dissolution results in a pseudo bimodal size distribution of nanoparticles in the cast membranes. The fact that the large silver crystals could only be observed in PSf/Ag<sup>ex</sup> (Type I) membranes can be due to two reasons: 1) casting mixtures for PSf/Ag<sup>ex</sup> and PSf/Ag<sup>in</sup> membranes of Types II and III have higher DMAC:Ag ratios; 2) PSf/Ag<sup>in</sup> of Types I, II and III incorporate the silver in predominantly ionic form due to negligible reduction of silver at room temperature [36] prior to incorporation into the casting mixture. Thus, the enhanced dissolution process can be responsible for the absence of larger crystals in membranes other than denser PSf/Ag<sup>ex</sup> Type I nanocomposites.

In summary, the filler distribution and matrix microstructure of nanocomposites can not be interpreted to arise from changes in the type or growth conditions of the filler or changes in the composition of the casting solution alone; instead, interactions in the quaternary system of polymer, solvent, non-solvent, and filler have to be considered to predict nanocomposite structure.

#### *3.3.2.4 Permeability and rejection of nanocomposite membranes*

The more compact Type I membranes showed a much higher (up to two orders of magnitude) resistance than the other membrane types (Table 2), which correlates with their lower surface porosity. Interestingly, for Type I membranes an order of magnitude decrease in membrane resistance upon silver modification was not accompanied by a major change in membrane rejection of 150 kDa dextran (Table 2). This suggests that while Type I Ag/PSf nanocomposites and their silver-free counterparts have pores of approximately same size, the density of pores is higher in the nanocomposites. This effect of silver on porosity was corroborated by SEM imaging as mentioned above (Fig. 3.3).

Membranes of Type II showed both higher permeabilities (lower resistances) and higher rejections than Type III membranes, likely because of the lower pore density in Type III membranes (Table 2). The comparison of PSf/Ag membranes of types II and III and their silver-free counterparts shows that while the inclusion of silver did not affect flux, there were significant differences in rejection.

Membrane		Resistance, $\times 10^{12} \text{ m}^{-1}$	Rejection , % 150 kDa dextran
Type I	PSf	$58.8 \pm 11.8$	$82.5 \pm 12.2$
	PSf/Ag <sup>in</sup>	$5.61 \pm 1.02$	$70.9 \pm 4.0$
	PSf/Ag <sup>ex</sup>	$4.03 \pm 0.75$	$67.6 \pm 5.1$
Type II	PSf	$0.16 \pm 0.03$	$35.1 \pm 0.2$
	PSf/Ag <sup>in</sup>	$0.15 \pm 0.01$	$32.1 \pm 1.8$
	PSf/Ag <sup>ex</sup>	$0.15 \pm 0.02$	$23.0 \pm 6.6$
Type III	PSf	$0.64 \pm 0.16$	$17.8 \pm 3.7$
	PSf/Ag <sup>in</sup>	$0.53 \pm 0.06$	$8.8 \pm 3.4$
	PSf/Ag <sup>ex</sup>	$0.66 \pm 0.09$	$5.4 \pm 2.8$

**Table 3.2.**Resistance and rejection values for all membrane types. Mass fractions of silver were the same for PSf/Ag<sup>ex</sup> and PSf/Ag<sup>in</sup> casting mixtures

In summary, the introduction of silver nanoparticles into the polymeric matrix induced noticeable changes in morphological properties and permeate flux only in membranes with a denser polymeric matrix (Type I membranes). However, rejection was affected for membranes of all types.

### **3.3.3 Antibacterial properties of nanocomposites**

Biofouling tests were conducted to determine the antibacterial effectiveness of nanocomposites of different porosities. Given that the nanoparticles are embedded within the polymeric structure of the membrane, the biocidal capacity of the nanocomposite membranes relies on their ability to leach out biotoxic silver ions ( $\text{Ag}^+$ ) to the solution. The measured extent of bacteria growth inhibition was then used to assess silver leaching by nanocomposites and to evaluate accessibility of embedded nanoparticles.

Recently, several comprehensive studies on the bacteriostatic and bactericidal properties of silver (both in ionic and nanoparticle form) have been published [40-44]. Silver nanoparticles can attach to the cell membrane to impede or disrupt vital metabolic processes, such as cellular respiration and membrane mediated transport mechanisms [43, 44]. Nanoparticles can also intercalate into the cell membrane [42-44], penetrate into the cell [43], and interact with proteins [43] or DNA [43] - macromolecules, possessing functional groups (amine, thiol, phosphate) that are known to have a high affinity for silver. Similar interactions can occur with silver ions, which can impact critical metabolic functions of the cell via protein denaturation [41], or cause lethal mutations and affect

cellular replication due to silver induced DNA condensation [41]. Ions can either enter the cell from the solution of the medium surrounding the cell, or can be introduced inside the cell as a result of leaching of nanoparticles located in the close proximity or within the cell [43].

The Bradford assay was chosen for the direct measurement of the amount of bacteria in the membrane biofilm. A significant advantage of the Bradford assay over commonly applied biofouling quantification methods such as colony counting, dye-based, and microscopy methods [45] is that the assay accounts for intrapore fouling. To our knowledge this is the first application of the Bradford assay to quantify membrane biofouling.

A thick biofilm and a large amount of extracellular polymeric substances (EPS) could be observed on the surfaces of all PSf membranes (Fig. 3.4 a, for example) after filtration of a bacterial solution and subsequent growth of the bacteria on agar. Under the same conditions, there was much less bacterial growth on the surfaces of both PSf/Ag<sup>in</sup> (Fig. 3.4 b) and PSf/Ag<sup>ex</sup> (Fig. 3.4 c) nanocomposites with respect to their silver-free counterparts. To quantify the amount of bacteria grown on a membrane, we lysed the *E. coli* cells present inside and on the surface of the membranes and determined the amount of released protein using a Bradford assay. As shown in Figure 3.5, the PSf/Ag<sup>in</sup> membranes showed less released protein than the PSf/Ag<sup>ex</sup> membranes of the same type. This conclusion was confirmed by t-testing, with a level of confidence higher than 95% for differences between PSf/Ag<sup>ex</sup> and PSf/Ag<sup>in</sup> membranes of Types I, II and III

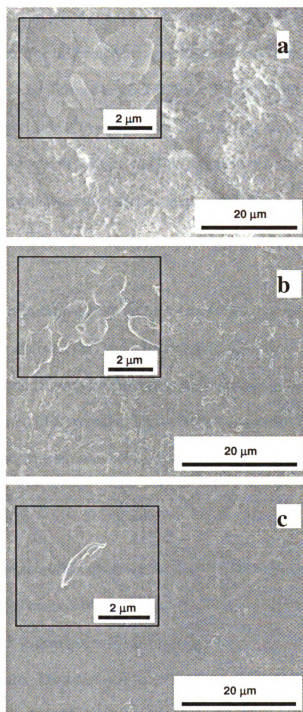


**Figure 3.4.** Typical SEM images of the surface of biofouled PSf Type I silver-free (a), PSf/Ag<sup>in</sup> (b) and PSf/Ag<sup>ex</sup> (c) membranes. Evident is the stark contrast between the thick biofilm developed on the surface of a silver-free membrane (a), and the absence of biofilm growth on the nanocomposite surface. The sample preparation procedure is detailed in section 3.2.4.

inoculated using the standard procedure when bacteria were deposited onto the skin surface of the membrane. The difference between PSf/Agex and PSf/Agin was significantly different at a confidence level of 90% for Type II membranes inoculated through the porous support side (“Type II reverse” in Fig. 3.5). The observed difference in antibacterial activity between PSf/Agin and PSf/Agex could result from a higher number of smaller nanoparticles, and, therefore, higher total surface area of the filler, in PSf/Agin membranes.

Figure 3.5 shows that the biofilm growth on the more porous membranes (Types II and III) was more extensive than that on Type I membranes, presumably because the higher porosity of the Type II and III surfaces facilitates initial attachment of bacteria, which leads to further growth and EPS secretion. The developing biofilm could also act as a protective barrier for subsequent bacteria by hindering the diffusion of silver ions towards the biofilm.

With all membranes, the nanoscale silver was somewhat effective in reducing biofilm growth (Figure 3.5). In all cases, silver modified membranes showed a significant decrease (higher than 95 % confidence level) in antibacterial efficiency with respect to the silver free counterparts. The t-test analysis indicates that for the very porous membranes, simulated by Type II membranes operated with the porous support side facing the feed, the antibacterial effect was less dependent on the method of silver incorporation; this was probably due to the fact that the access of bacteria to silver was limited by the silver diffusion rate and not by the availability of silver nanoparticles.

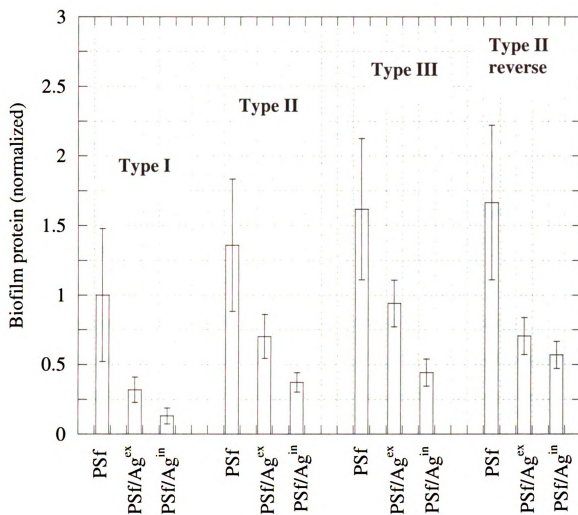


**Figure 3.5.** Bradford assay results describing the biofilm growth on the surface of PSf membranes and PSf/Ag nanocomposites of different porosities under diffusive transport conditions.

While the accessibility of silver is a function of both the route of nanoparticle incorporation and the morphology of the polymeric matrix, these two factors are interdependent and it is thus difficult to separate their influence on filler's accessibility to the permeate flow. Note that the membrane skin, which in this experiment was on the permeate side, provided an absolute barrier to the bacteria, so the number of inoculated bacteria retained by the membrane was the same as that in all other biofouling assays. Thus a straightforward comparison with the Type II membranes inoculated on the skin side should be possible.

Finally, consideration must be given to the fact that the mass of silver contained in more porous nanocomposites (types II and III) was lower than in the denser Type I membranes (although the PSf/Ag mass ratio was the same). The lower absolute amount of silver, coupled with the fact that more porous membranes have a rougher surface and, therefore, higher surface area, could have also contributed towards the observed higher bacteria growth in more porous matrices.

### **3.3.4 Practical aspects of the application of silver nanocomposites as membrane and membrane spacer materials**

#### *3.3.4.1 Effect of antibacterial activity on the efficiency of hydraulic cleaning*

To evaluate the responsiveness of biofilms formed on PSf and PSf/Ag membranes to hydraulic cleaning, rinsing was included as a part of the biofouling assay. During the

rinsing step, membranes were washed with ultrapure water for 30 seconds. Even though in all cases there was an observed, and expected, decrease in the measured protein content after hydraulic rinsing (see SD), statistical analysis showed that the differences in the efficiency of hydraulic cleaning between nanocomposites and their silver-free counterparts were not statistically significant.

#### *3.3.4.2 Antibacterial efficiency of nanocomposite membranes under convective transport conditions*

As stated in the experimental section, PSf/Ag<sup>in</sup> and PSf/Ag<sup>ex</sup> nanocomposites of Type III were tested in a continuous deionized water recirculation system, and the leached silver was periodically measured using ICP-MS. Both PSf/Ag<sup>in</sup> III and PSf/Ag<sup>ex</sup> III leached comparable amounts of silver with final 4-day silver loss values (expressed as a percent of the calculated mass of silver originally present in the coupons) of 0.0016% and 0.0014% for the PSf/Ag<sup>in</sup> III and PSf/Ag<sup>ex</sup> III, respectively. One could expect even slower leaching for nanocomposites of types I and II because of their lower porosity. In all cases the leachates had a silver concentration around or below 1 µg/L, which is 100 times below the EPA standard (0.1 mg/L) for Ag<sup>+</sup> in drinking water. Interestingly, this concentration is also significantly below reported values (4 µg/mL to 85 µg/mL) for the concentration of silver (ionic or nanoparticulate form or both) that results in observed toxicity for *E. coli*[40-44, 46]. It should be noted, however, that ionic silver released from the nanocomposites might be enhanced in the presence of exogenous complexing agents that could be found in more complex water matrices.

While the values of silver concentration were within the range of the calibration curve, they were close to the ICP-MS detection limit. For this reason, further leaching tests involved indirect measurement of silver by the degree of biofilm growth inhibition, as explained in section 3.2.7.2. The biofilm growth inhibition under *convective* flow conditions was studied only for Type I membranes. The hypothesis was that the leached silver would be carried away from the membrane surface with the permeate flow and thus the growth inhibition capacity of the nanocomposite would be suppressed. To test the hypothesis under the most conservative conditions, Type I membranes were chosen as those that showed the highest growth inhibition in preliminary tests without permeate flow (Fig. 3.5). The results obtained for the inhibition of biofilm growth under conditions of convective flow through the membrane are shown in Fig. 3.6. The first two bars of Fig. 3.6 describe the extent of biofilm growth after continuous 48 hr of filtration of LB medium through nanocomposite samples that were previously used to filter 2 mL of an *E. coli* solution. There was no significant difference between the growth observed on PSf/Ag<sup>in</sup> Type I membranes and PSf controls. We attribute this to the fact that leached silver is convectively transported towards the permeate side of the membrane and away from bacteria accumulated on the membrane surface facing the feed. This finding emphasizes the limited efficiency of biocide-releasing membranes in inhibiting the biofilm development on the upstream side of the membrane due to the fact that leachate is carried away from the growing biofilm. This conclusion is further corroborated by the result of a silver leaching test under convective conditions where silver-containing feed

(permeate from a bacteria-free silver nanocomposite) is directed to the membrane surface inoculated

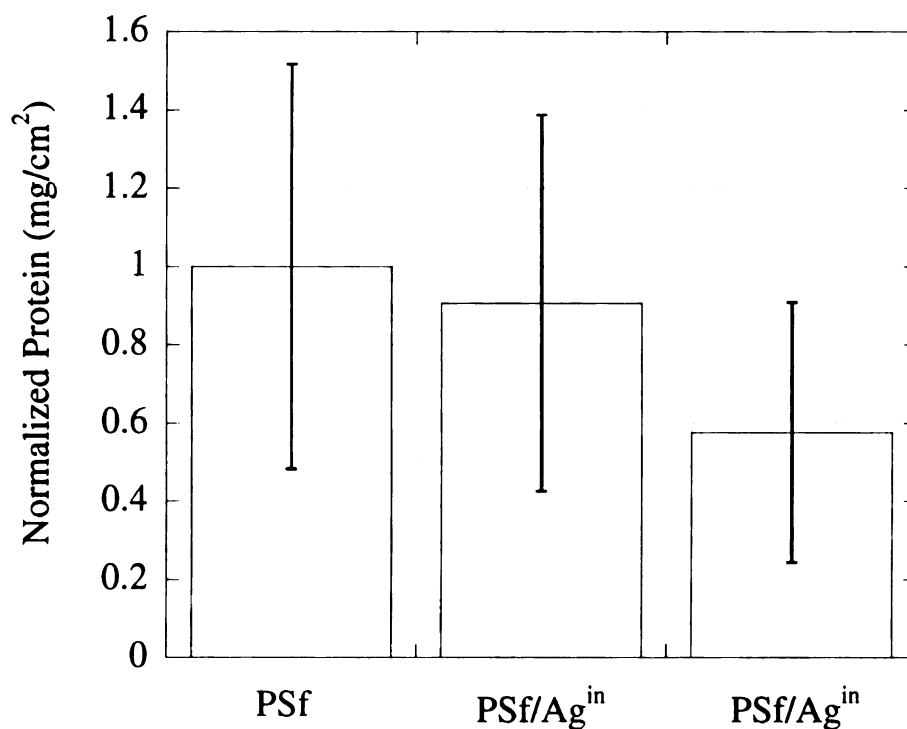


**Figure 3.6.** Biofilm growth on PSf/Ag Type I nanocomposites after 48 hr of continuous filtration of a) LB medium (first two columns) and b) leachate obtained by continuously filtering DI water through PSf/Ag Type I nanocomposite for 2 days (third column). The leachate was Ag-loaded water obtained from the filtration of DI water through a bacteria-free PSf/Ag Type I nanocomposite; the leachate was then mixed with LB medium to be filtered through an inoculated Ag-free membrane.

with bacteria (section 3.2.7.3.) The third column of Fig. 3.6 illustrates the inhibition of the biofilm growth on the membrane surface when 2-day nanocomposite leachate is filtered through a membrane inoculated with bacteria, where a significant (90 % confidence level) decline was observed in this case.

Although convective flow essentially eliminated the biocidal activity of PSf/Ag membranes, the built-in antibacterial capacity should still be effective in reducing intrapore fouling in more porous membranes. The silver-releasing nanocomposites could also be used as materials for macroporous membrane spacers to inhibit the biofilm growth on downstream membrane surfaces. The leached silver would primarily be targeting, and absorbed by, bacteria growing on the downstream target membrane. Given the extremely low concentrations of silver necessary to inhibit the growth of membrane biofilms, such approaches may be advantageous relative to the use of the biocide as a bulk water additive wherein the biocide's ability to reach the membrane could be affected by the presence of other surfaces and components of the water that could act as sinks for the biocidal agent.

### 3.4. Conclusions

In this study, the effects of casting mixture composition and nanoparticle incorporation route on the morphological and separation properties of prepared porous nanocomposite membranes were studied using silver as the model filler material. We demonstrated that:

- (1) The reduction of ionic silver by polymer solvents prior to or during the phase inversion process can be employed to synthesize silver-polymer nanocomposites of a range of porosities and nanoscale silver distributions.
- (2) Ex-situ and in-situ routes of filler incorporation result in markedly different nanocomposite morphologies. The two methods yield differences in both the size of the filler and its distribution along the cross-section of the matrix.
- (3) The effects of filler incorporation are more pronounced for less porous membranes. For casting mixtures that yield membranes with relatively low porosity, the induced morphological changes - macrovoid broadening and an increase in surface pore size and density - translate into an improvement in separation properties wherein a significant decrease in the hydraulic resistance is accompanied by only a minor decrease in rejection. To predict the structure of such nanocomposite membranes, interactions in the quaternary system of polymer, solvent, non-solvent, and filler have to be considered.

(4) The built-in antibacterial capacity due to the gradual release of ionic silver by the prepared nanocomposites can be effective in reducing intrapore biofouling in porous membranes of a wide range of porosities. Such nanocomposites could in principle be used as materials for macroporous membrane spacers to inhibit the biofilm growth on downstream membrane surfaces.

In summary, incorporation of nanoparticles into a forming membrane matrix appears to be an attractive approach to the design of nanocomposite structures with improved mechanical and separation properties and with embedded nanoparticle-based functionalities.

## **Acknowledgements**

This material is based upon work supported by the National Science Foundation under Grant No. OISE-0530174. Robin Diets is acknowledged for his assistance with membrane permeability and rejection measurements. We also thank Solvay Polymers for providing the polysulfone for membrane synthesis. JST acknowledges support by Nordberg and McCowan fellowships. Any opinions, findings, and conclusions or recommendations expressed in this material are those of the authors and do not necessarily reflect the views of the National Science Foundation.

## Supporting Documentation

### **Effect of filler incorporation route on the properties of polysulfone-silver nanocomposite membranes of different porosities**

Published in

*Journal of Membrane Science*

Volume 325, 2008, pages 58-68

by

Julian S. Taurozzi<sup>†</sup>, Hari Arul<sup>||</sup>, Volodymyr Z. Bosak<sup>‡</sup>, Anatoliy F. Burban<sup>‡</sup>, Thomas C. Voice<sup>†</sup>, Merlin L. Bruening<sup>‡</sup>, and Volodymyr V. Tarabara<sup>†</sup>

<sup>†</sup> Department of Civil and Environmental Engineering, Michigan State University, East Lansing, MI 48824, USA

<sup>||</sup> High School Honors Science, Mathematics, Engineering Program, Michigan State University

<sup>‡</sup> Department of Chemistry, The National University of "Kyiv-Mohyla Academy", 2, Skovoroda St., Kyiv, 04070, Ukraine

<sup>‡</sup> Department of Chemistry, Michigan State University, East Lansing, MI 48824, USA

### **SD.3.1.SEM sample preparation procedure**

For SEM imaging, all samples were coated with osmium for 20 s at a current of 10 mA using an osmium plasma coater (model NEOC-AT, Meiwa Shoji Co., Osaka, Japan). To image membrane cross-sections, samples were freeze-fractured upon immersion in liquid nitrogen, coated and mounted on SEM sample holders. For biofilm observation, membranes were fixed by immersion in a solution of glutaraldehyde and paraformaldehyde (2.5% v/v each) in 0.1 M sodium cacodylate buffer for 30 min followed by a 10 min immersion in 0.1 M sodium cacodylate buffer. The fixed samples were then dehydrated by sequential rinsing in solutions of ethanol in water with increasing ethanol concentrations (25, 50, 75, 95, and 100% ethanol).

### **SD.3.2.TEM sample preparation procedure**

For TEM sample sectioning, the membranes were embedded in LRwhite resin (medium grade, London Resin Co., UK) for 24 hr and further polymerized for 24 hr in an oven at 60 °C. Ultrathin (70 nm) sections of the embedded samples were cut using an ultramicrotome (Power Tome XL, RMC, Boeckeler Instruments, Tucson, AZ) equipped with a diamond knife (Diatome, 35° angle). For ultrathin section observation, a JEOL 100 CX TEM with an accelerating voltage of 100 kV and a maximum theoretical resolution of 0.2 nm, coupled to a MegaView III Camera (Soft Imaging System, Lakewood, CO) was employed. Standard copper grids (300 mesh, Electron Microscopy Sciences) were used to support samples.

To verify that silver nanoparticles were not dissolved during embedding, a control test was performed. Silver nanoparticle hydrosol was prepared [32] with a mean particle diameter of around 50 nm (ZetaPALS, Brookhaven Instrument Corp., Holtsville, NY). The obtained hydrosol was then added to the vial with LR white resin, and vortexed to allow for nanoparticle dispersion within the resin. The nanoparticles were left in the viscous medium for 24 hr, emulating the membrane embedding process, and the resin was then polymerized in an oven at 60 °C. Ultrathin sections of the nanoparticle-doped resin were obtained following the same procedure as that for membrane sample sectioning, and observed using the same TEM instrument. The TEM micrographs clearly showed well defined crystalline nanoparticles within the measured 50 nm size range. Similar images were obtained under the TEM for the hydrosol dried on a formvar coated TEM grid, verifying that dissolution of silver in the embedding resin was negligible.

### **SD.3.3.TEM-EDS analysis**

The transmission electron microscope used for TEM/EDS characterization was a JEM-2200FS with field emission gun operation at 200 kV and a point resolution of 0.19 nm; images were taken using a Gatan 794 MSC digital camera. The instrument was equipped with an X-ray energy dispersive spectroscopy (X-EDS) system (Oxford Instruments) with an optimal energy resolution of 140 eV. The following image shows the spectra obtained from the analysis of a nanoparticle loaded portion of a PSf/Agin Type I membrane.

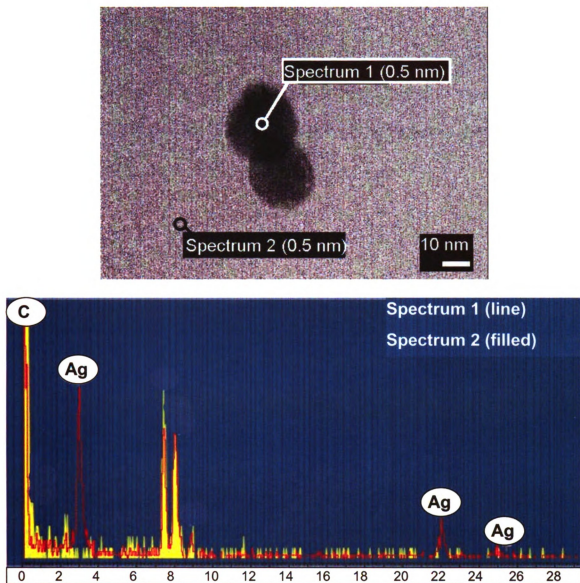


**Figure SD.3.1.** TEM image (top) of silver nanoparticles (Spectrum 1) embedded in the PSf matrix (Spectrum 2) of a PSf/Ag<sup>in</sup> Type I membrane, and EDS spectra (bottom) of both the PSf matrix (yellow filled spectrum) and the Ag nanoparticles (line spectrum) showing the silver peaks for the nanoparticle. The x-axis for the EDS spectra is in KeV units.

#### **SD.3.4.ATR-FTIR analysis**

ATR-FTIR measurements were performed using a Nicolet Magna-IR 550 spectrometer at a rate of 16 scans per second with a resolution of  $1.928\text{ cm}^{-1}$ . Omnic software was used to control spectral acquisition and to process the acquired data.

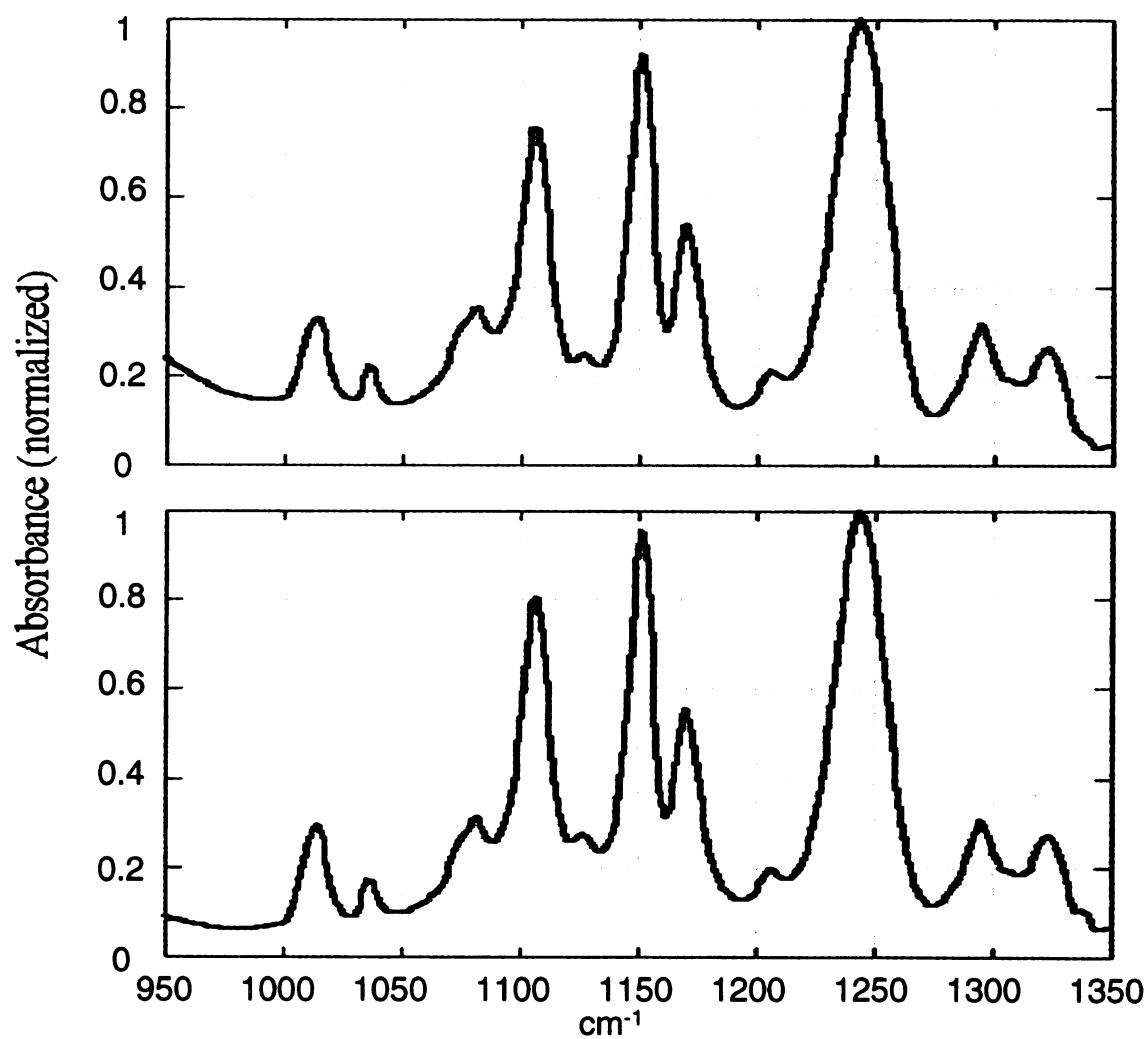
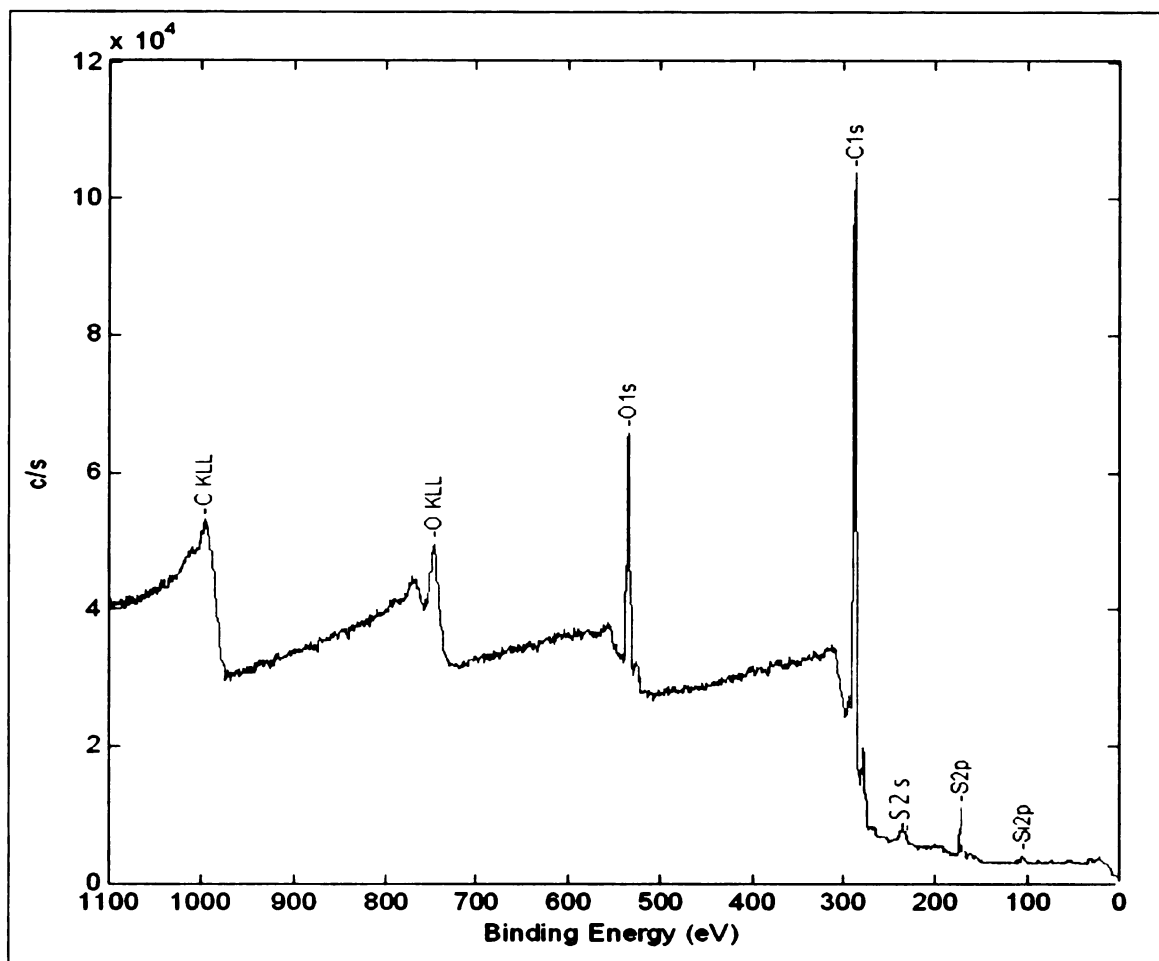


**Figure SD.3.2.**FTIR spectra of PSf Type I (Top) and PSf/Ag<sup>in</sup> Type I (bottom) membranes.

### **SD.3.5.XPS analysis**

XPS measurements of Ag-modified membranes were carried out using a PHI 5400 ESCA system (Physical Electronics, Chanhassen, MN) equipped with a non-monochromatic Mg X-ray. In all measurements a take-off angle of 45° was used. The following shows the results obtained from the analysis of a PSf/Ag<sup>in</sup> Type I membrane.



C1s	N1s	O1s	Si2p	S2p	Ag3d
80.50	0.02	15.62	0.83	2.97	0.06

**Figure SD.3.3.** XPS survey spectrum and atomic concentration (relative) table for a PSf/Ag<sup>in</sup> Type I membrane. The silver signal is not visible in the survey spectrum.

### **SD.3.6.Effect of antibacterial activity on the efficiency of hydraulic cleaning**

To evaluate the responsiveness of biofilms formed on PSf and PSf/Ag membranes to hydraulic cleaning, rinsing was included as a part of the biofouling assay. During the rinsing step, membranes were washed with ultrapure water for 30 seconds. The following figure shows the measured protein values for the membranes with and without rinsing.

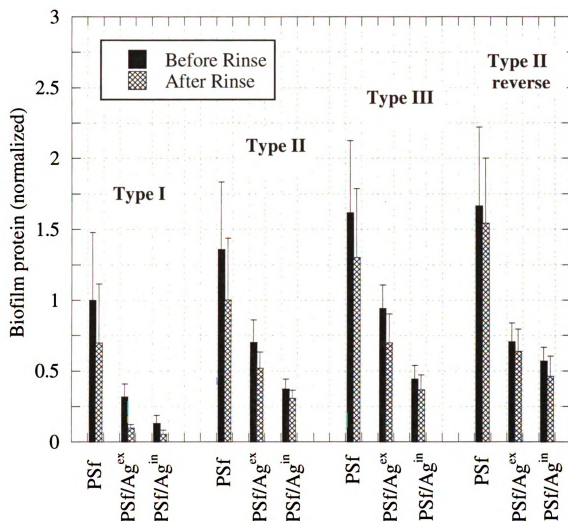


**Figure SD.3.4.** Bradford assay results describing the biofilm growth on the surface of PSf membranes and PSf/Ag nanocomposites of different porosities under diffusive transport conditions, both with and without hydraulic rinsing.

**SD.3.7.T-test tables**

T-tests were performed to determine whether differences in the biocidal effects for the tested nanocomposites were statistically significant. The following tables summarize the comparative t values for the analyzed pairs. The more general, two-sample T-test (instead of the commonly used pooled T-test) was applied, due to the large variance differences between sample sets.

		Mean	Error	t values (vs. PSf)	t values (Ag <sup>ex</sup> vs Ag <sup>in</sup> )
Type I	PSf	1.000	0.479	---	---
	PSf/Ag <sup>in</sup>	0.318	0.092	2.82	---
	PSf/Ag <sup>ex</sup>	0.130	0.058	3.64	3.50
Type II	PSf	1.358	0.475	---	---
	PSf/Ag <sup>in</sup>	0.702	0.159	2.65	
	PSf/Ag <sup>ex</sup>	0.373	0.070	4.15	3.82
Type III	PSf	1.618	0.509	---	---
	PSf/Ag <sup>in</sup>	0.939	0.169	2.56	
	PSf/Ag <sup>ex</sup>	0.442	0.097	4.59	5.15
Type II (reverse)	PSf	1.665	0.555	---	---
	PSf/Ag <sup>in</sup>	0.705	0.133	3.40	---
	PSf/Ag <sup>ex</sup>	0.569	0.097	3.93	1.67

**Table SD.3.1.** Statistical data analysis for released protein on diffusive biofouling experiments without hydraulic rinsing (Figure 3.5 of main document). Mean values are normalized to that of PSf/Type I membranes, errors are calculated with a 90% confidence level, the “t values” columns indicate the comparative basis for each pair.

	Mean	Error	t values (vs. Psf-I)
Psf-I	1.000	0.518	---
Psf-I/Ag <sup>in</sup>	0.906	0.481	0.344
Accum. 2 days	0.576	0.333	1.705

**Table SD.3.2.** Statistical data analysis for released protein on convective biofouling experiments (Figure 3.6 of main document). Mean values are normalized to that of PSf/Type I membranes, errors are calculated with a 90% confidence level, the “t values” columns indicate the comparative basis for each pair.

## References

1. T. H. Bae and T. M. Tak, Preparation of TiO<sub>2</sub> self-assembled polymeric nanocomposite membranes and examination of their fouling mitigation effects in a membrane bioreactor system, *J. Membr. Sci.* 266 (2005) 1-5.
2. J. Dai and M. L. Bruening, Catalytic nanoparticles formed by reduction of metal ions in multilayered polyelectrolyte films, *Nanoletters* 2 (2002) 497 - 501.
3. Z. Li, H. Huang, T. Shang, F. Yang, W. Zheng, C. Wang and S. K. Manohar, Facile synthesis of single-crystal and controllable sized silver nanoparticles on the surfaces of polyacrylonitrile nanofibres, *Nanotechnol.* 17 (2006) 917-920.
4. R. Molinari, L. Palmisano, E. Drioli and M. Schiavello, Studies on various reactor configurations for coupling photocatalysis and membrane processes in water purification, *J. Membr. Sci.* 206 (2002) 399-415.
5. L. Wu and S. M. C. Ritchie, Removal of trichloroethylene from water by cellulose acetate supported bimetallic Ni/Fe nanoparticles, *Chemosphere* 63 (2006) 285-292.
6. L. F. Wu, M. Shamsuzzoha and S. M. C. Ritchie, Preparation of cellulose acetate supported zero-valent iron nanoparticles for the dechlorination of trichloroethylene in water, *J. Nanopart. Res.* 7 (2005) 469-476.
7. J. Xu and D. Bhattacharyya, Fe/Pd nanoparticle immobilization in microfiltration membrane pores: Synthesis, characterization, and application in the dechlorination of polychlorinated biphenyls, *Ind. Eng. Chem. Res.* 46 (2007) 2348-2359.
8. P. Aerts, I. Genne, S. Kuypers, R. Leysen, I. F. J. Vankelecom and P. A. Jacobs, Polysulfone-aerosil composite membranes: Part 2. The influence of the addition of aerosil on the skin characteristics and membrane properties, *J. Membr. Sci.* 178 (2000) 1-11.
9. P. Aerts, E. Van Hoof, R. Leysen, I. F. J. Vankelecom and P. A. Jacobs, Polysulfone-aerosil composite membranes: Part 1. The influence of the addition of Aerosil on the formation process and membrane morphology, *J. Membr. Sci.* 176 (2000) 63-73.
10. L. Ballinas, C. Torras, V. Fierro and R. Garcia-Valls, Factors influencing activated carbon-polymeric composite membrane structure and performance, *J. Phys. Chem. Solids* 65 (2004) 633-637.
11. A. Bottino, G. Capannelli and A. Comite, Preparation and characterization of novel porous PVDF-ZrO<sub>2</sub> composite membranes, *Desalination* 146 (2002) 35-40.

12. A. Bottino, G. Capannelli, V. D'Asti and P. Piaggio, Preparation and properties of novel organic-inorganic porous membranes, *Separ. Purif. Technol.* 22-23 (2001) 269-275.
13. W. L. Chou, D. G. Yu and M. C. Yang, The preparation and characterization of silver-loading cellulose acetate hollow fiber membrane for water treatment, *Polym. Advan. Technol.* 16 (2005) 600-607.
14. I. Genne, S. Kuypers and R. Leysen, Effect of the addition of ZrO<sub>2</sub> to polysulfone based UF membranes, *J. Membr. Sci.* 113 (1996) 343-350.
15. J. B. Li, J. W. Zhu and M. S. Zheng, Morphologies and properties of poly(phthalazinone ether sulfone ketone) matrix ultrafiltration membranes with entrapped TiO<sub>2</sub> nanoparticles, *J. Appl. Polym. Sci.* 103 (2006) 3623-3629.
16. D. E. Meyer, K. Wood, L. G. Bachas and D. Bhattacharyya, Degradation of chlorinated organics by membrane-immobilized nanosized metals, *Environ. Prog.* 23 (2004) 232-242.
17. O. Monticelli, A. Bottino, I. Scandale, G. Capannelli and S. Russo, Preparation and properties of polysulfone-clay composite membranes, *J. Appl. Polym. Sci.* 103 (2007) 3637-3644.
18. N. M. Wara, L. F. Francis and B. V. Velamakanni, Addition of alumina to cellulose acetate membranes, *J. Membr. Sci.* 104 (1995) 43-49.
19. L. Yan, Y. S. Li, C. B. Xiang and S. Xianda, Effect of nano-sized Al<sub>2</sub>O<sub>3</sub>-particle addition on PVDF ultrafiltration membrane performance, *J. Membr. Sci.* 276 (2006) 162-167.
20. Y. Yang, H. Zhang, P. Wang, Q. Zheng and J. Li, The influence of nano-sized TiO<sub>2</sub> fillers on the morphologies and properties of PSF UF membrane, *J. Membr. Sci.* 288 (2007) 231-238.
21. D. G. Yu, M. Y. Teng, W. L. Chou and M. C. Yang, Characterization and inhibitory effect of antibacterial PAN-based hollow fiber loaded with silver nitrate, *J. Membr. Sci.* 225 (2003) 115-123.
22. X. He, Q. Shi, X. Zhou, C. Wan and C. Jiang, In situ composite of nano SiO<sub>2</sub>-P(VDF-HFP) porous polymer electrolytes for Li-ion batteries, *Electrochim. Acta* 51 (2005) 1069-1075.
23. W. K. Son, J. H. Youk, T. S. Lee and W. H. Park, Preparation of antimicrobial ultrafine cellulose acetate fibers with silver nanoparticles, *Macromol. Rapid Commun.* 25 (2004) 1632-1637.

24. K. Ebert, D. Fritsch, J. Koll and C. Tjahjajawiguna, Influence of inorganic fillers on the compaction behaviour of porous polymer based membranes, *J. Membr. Sci.* 233 (2004) 71-78.
25. G. Jonsson, Methods for determining the selectivity of reverse osmosis membranes, *Desalination* 24 (1977) 19-37.
26. K. M. Persson, V. Gekas and G. Tragardh, Study of membrane compaction and its influence on ultrafiltration water permeability, *J. Membr. Sci.* 100 (1995) 155-162.
27. J. H. Choi, J. Jegal and W. N. Kim, Fabrication and characterization of multi-walled carbon nanotubes/polymer blend membranes, *J. Membr. Sci.* 284 (2006) 406-415.
28. D. E. Meyer and D. Bhattacharyya, Impact of membrane immobilization on particle formation and trichloroethylene dechlorination for bimetallic Fe/Ni nanoparticles in cellulose acetate membranes, *J. Phys. Chem. B* 111 (2007) 7142-7154.
29. M. J. Han and D. Bhattacharyya, Changes in morphology and transport characteristics of polysulfone membranes prepared by different demixing conditions, *J. Membr. Sci.* 98 (1995) 191-200.
30. V. Kaiser and C. Stropnik, Membranes from polysulfone/N,N-dimethylacetamide/water system; Structure and water flux, *Acta Chimica Slovenica* 47 (2000) 205-213.
31. P. Radovanovic, S. W. Thiel and S. T. Hwang, Formation of asymmetric polysulfone membranes by immersion precipitation.2. The effects of casting solution and gelation bath compositions on membrane-structure and skin formation, *Journal Of Membrane Science* 65 (1992) 231-246.
32. C. Stropnik, V. Kaiser, V. Musil and M. Brumen, Wet-phase-separation membranes from the polysulfone/N,N-dimethylacetamide/water ternary system: The formation and elements of their structure and properties, *Journal Of Applied Polymer Science* 96 (2005) 1667-1674.
33. R.E. Kesting, *Synthetic polymeric membranes, a structural perspective*. 2nd ed. 1985: John Wiley & Sons, Inc.
34. J. H. Kim and K. H. Lee, Effect of PEG additive on membrane formation by phase inversion, *Journal of Membrane Science* 138 (1998) 153-163.
35. Q. Z. Zheng, P. Wang and Y. N. Yang, Rheological and thermodynamic variation in polysulfone solution by PEG introduction and its effect on kinetics of membrane formation via phase-inversion process, *J. Membr. Sci.* 279 (2006) 230-237.
36. I. Pastoriza-Santos and L. M. Liz-Marzan, Formation and stabilization of silver nanoparticles through reduction by N,N-Dimethylformamide, *Langmuir* 15 (1999) 948-951.

37. M. M. Bradford, A rapid and sensitive method for the quantitation of microgram quantities of protein utilizing the principle of protein-dye binding, *Anal. Biochem.* 72 (1976) 248-254.
38. J. D. Gu and L. Pan, Comparing the growth characteristics of three bacteria involved in degrading rubbers, *J. Polym. Environ.* 14 (2006) 273-279.
39. K. Boussu, C. Vandecasteele and B. Van der Bruggen, Study of the characteristics and the performance of self-made nanoporous polyethersulfone membranes, *Polymer* 47 (2006) 3464-3476.
40. C. Baker, A. Pradhan, L. Pakstis, D. J. Pochan and S. I. Shah, Synthesis and antibacterial properties of silver nanoparticles, *J. Nanosci. Nanotechnol.* 5 (2005) 244-249.
41. Q. L. Feng, J. Wu, G. Q. Chen, F. Z. Cui, T. N. Kim and J. O. Kim, A mechanistic study of the antibacterial effect of silver ions on *Escherichia coli* and *Staphylococcus aureus*, *J. Biomed. Mater. Res.* 52 (2000) 662-668.
42. S. K. Gogoi, P. Gopinath, A. Paul, A. Ramesh, S. S. Ghosh and A. Chattopadhyay, Green fluorescent protein-expressing *Escherichia coli* as a model system for investigating the antimicrobial activities of silver nanoparticles, *Langmuir* 22 (2006) 9322-9328.
43. J. R. Morones, J. L. Elechiguerra, A. Camacho, K. Holt, J. B. Kouri, J. T. Ramirez and M. J. Yacaman, The bactericidal effect of silver nanoparticles, *Nanotechnology* 16 (2005) 2346-2353.
44. I. Sondi and B. Salopek-Sondi, Silver nanoparticles as antimicrobial agent: a case study on *E. coli* as a model for Gram-negative bacteria, *J. Colloid Interface Sci.* 275 (2004) 177-182.
45. J. Mallevialle, P. E. Odendaal and M. R. Wiesner, *Water Treatment Membrane Processes*. 1996: McGraw-Hill.
46. K. Y. Yoon, J. H. Byeon, J. H. Park and J. Hwang, Susceptibility constants of *Escherichia coli* and *Bacillus subtilis* to silver and copper nanoparticles, *Sci. Total Environ.* 373 (2007) 572-575.

## CHAPTER FOUR

### **Silver nanoparticle arrays on track etch membrane support as flow-through optical sensors for water quality control**

Published in

Environmental Nanotechnology special issue of

*Environmental Engineering Science* journal

Volume 24 (1), 2007, pages 122-137

by

Julian S. Taurozzi<sup>‡</sup> and Volodymyr V. Tarabara<sup>‡</sup>

<sup>‡</sup> Department of Civil and Environmental Engineering, Michigan State University,

East Lansing, MI 48824, USA

## CHAPTER FOUR

### **Silver nanoparticle arrays on track etch membrane support as flow-through optical sensors for water quality control**

#### **Abstract**

Silver nanoparticle arrays were assembled on the surface of polycarbonate track etch membranes using 3-aminopropyltrimethoxysilane as the chemical linker. The assembled arrays were sub-monolayer and reproducibly regular. The nanoparticle-modified membranes were characterized in terms of their hydraulic and optical properties and were evaluated as flow-through surface-enhanced Raman scattering (SERS) sensors for water quality monitoring. The membrane-supported nanoparticle arrays were found to be SERS-active with slightly lower but significantly more reproducible enhancements in comparison with enhancements afforded by source nanoparticle suspensions. Large enhancements of up to  $10^5$  were demonstrated due to preconcentration by recirculating analyte solution through nanoparticle-modified membranes that were shown to retain their hydraulic properties. The findings point to the promise of combining high specification SERS-active systems and the flow-through design for the development of analytical sensors for the trace detection of aqueous pollutants.

## 4.1. Introduction

Timely detection of water supply contamination, accurate assessment of related risks, and development of appropriate remediation strategies depend on the availability of reliable water quality monitoring technologies [1]. At the core of these technologies are deployable environmental sensors subject to such criteria as fingerprinting capability, low fouling characteristics, reproducibility, and low detection limits. The lack of sensing devices that meet these demands is the main limitation of pollution detection methods in use today.

The detection process can be viewed as consisting of two consecutive stages: (1) selective *preconcentration*/separation of pollutants and (2) *measurement* of pollutant concentration. To reliably determine the occurrence of molecular contaminants or microbial pathogens in natural and treated waters, large volumes (up to 1000 liters) of source water have to be sampled and preconcentrated to much smaller volumes. For rapid assaying of microbial pathogens, for example, acceptable concentrate volumes are smaller than 1 liter and often are as small as several milliliters [2, 3] . In addition to separating pollutants from the system matrix, preconcentration enhances detection sensitivity, which is especially important for the detection of water pollutants in very low concentrations. The practical worth of preconcentration is exemplified by the use of membranes for the detection of microbial pathogens in aqueous systems [3-8].

At the measurement stage, the employed detection methods have to be sensitive and selective. The remarkable sensitivity and molecular specificity afforded by surface enhanced Raman scattering (SERS) [9-13] makes this spectroscopic technique especially attractive for those sensing applications, where both low detection limits and fingerprinting capability are needed [14]. Reports of single-molecule detection using SERS [15] and the design of flow-through SERS systems [16] have further amplified interest in possible uses of this technique for environmental sensing [17-21].

The SERS effect can be observed when a light-scattering molecule is adsorbed on a SERS-active substrate, typically a roughened surface of certain coinage metals, gold and silver being primary examples. The choice of the type of the enhancing substrate remains application-specific because different types of SERS-active substrates exhibit different properties; island metal films on a solid support, for example, are more stable, while for aggregated metal colloids higher enhancements are generally expected [22]. What all SERS-active systems have in common, however, is that the morphology of substrates has a profound effect on their optical properties. In the case of nanoparticle suspensions, the relatively poor stability of sols and the dependence of nanoparticle aggregate morphology on the nature and concentration of the analyte partly offsets the advantage of high enhancements typical of such substrates. The difficulty in fabricating SERS-active substrates that reproducibly yield high enhancements is the single most significant factor that hampers further applications of the SERS method for sensing. Development of highly enhancing, but also stable, reproducible, and robust SERS-active substrates is, therefore, very important for SERS to mature into an “off-the-shelf” detection method.

One approach to improve reproducibility of SERS is the immobilization of nanoparticles on stable supports [23, 24]. Permeable supports are of particular interest as they may allow for the added advantage of preconcentration. The idea of using filters as SERS substrates has been approached previously from different perspectives by several research groups [25-29]. The studies involved coverage of a permeable substrate - filter paper or aluminum based membranes - with silver nanoparticles. The substrate preparation has been based either on the filtration of silver colloids through polymeric membranes [28] or on the chemical reduction of silver directly on the filter surface [26, 27]. Since the filtration-based methods involved retention of silver particles in the membranes, the filtering ability of such membranes could be expected to be greatly inhibited. Recently, the method of vacuum deposition of silver onto an aluminum membrane filter was reported wherein the filter permeability could be expected to remain unchanged [29]. By filtering a small amount of analyte solution through the membrane, an improved detection capability was demonstrated.

The objective of this work was to develop flow-through SERS-active substrates by assembling arrays of silver nanoparticles on the surface of track etch polycarbonate membranes [30, 31]. Previously, nitrogen functionalities have been successfully introduced to polycarbonate and other polymeric structures by using plasma treatment [32-36] and by employing the reactivity of polycarbonate with amines [37, 38]. Our approach was to employ 3-aminopropyltrimethoxysilane and cysteamine as chemical linkers between polycarbonate surface and silver nanoparticles. SERS enhancing

properties of resulting membrane-supported arrays were tested and compared with those of source nanoparticle suspensions using methylene blue (MB) as an analyte relevant for pathogen detection and inactivation techniques [39, 40]. Finally, we considered sensitivity in a broader context that included membrane-enabled preconcentration as the factor that augments the inherently high sensitivity of nanoparticle-based SERS substrates and studied the effect of preconcentration on the sensitivity of the developed sensors.

## **4.2. Experimental**

### **4.2.1 Materials**

The ultrapure water used in the experiments was supplied by a commercial ultrapure water system (Lab Five, USFilter Corp., Hazel Park, MI) equipped with a terminal 0.2  $\mu\text{m}$  capsule microfilter (PolyCap, Whatman Plc., Sanford, ME). The resistivity of water was greater than 16  $\text{M}\Omega\text{-cm}$ . Boil off nitrogen and 99.9999 % purity argon gases were used in the plasma experiments.

### **4.2.2 Synthesis of silver nanoparticles**

Aqueous suspensions of silver nanoparticles (Ag hydrosols) were prepared using the procedure described by Lee and Meisel [41]. 90 mg of silver nitrate were added to 500 mL of ultrapure water and brought to 100  $^{\circ}\text{C}$ . 10 mL of 1 % by weight solution of trisodium citrate were added dropwise to the boiling water under vigorous stirring. To prepare sols with a narrower particle size distribution, sodium citrate solution was added as quickly as possible and in the smallest droplets possible. Gradual color change of the solution from transparent to greenish gray was indicative of the progress of silver particle nucleation reaction. The erlenmeyer flask containing the solution was loosely capped with a ceramic crucible to avoid significant solvent loss due to evaporation. After 40 minutes of boiling, the hydrosol was left to cool down. The loss of water to evaporation

was compensated by the addition of ultrapure water to restore the original volume of 500 mL. After allowing the hydrosol to cool down to room temperature, it was stored at 4 °C.

To precoagulate sol, 100 µL of silver sol were mixed with 100 µL of ultrapure water and 10 µL of a 0.5 mol/L NaClO<sub>4</sub> aqueous solution. For SERS measurements in precoagulated Ag hydrosols, 30 µL of the precoagulated suspension were removed and 20 µL of the analyte solution were added, yielding a final 1:10 dilution of the sample in the precoagulated sol. The resulting preparation was used for SERS measurements.

#### **4.2.3 Membranes and membrane surface modification**

25 mm diameter, 5 µm nominal pore size hydrophobic polyvinylpyrrolidone(PVP)-free polycarbonate track etch (PCTE) membrane filters were purchased from Sterlitech (Sterlitech Corp, Kent, WA). Based on the value of pore density ( $4 \cdot 10^5$  pores/cm<sup>2</sup>) reported by the manufacture the average distance between pores was estimated to be ca. 16 µm.

Two approaches to membrane modification were explored. The first approach was to treat membranes with nitrogen plasma to directly introduce nitrogen functionalities on the membrane surface, or to treat membranes with argon plasma and then immerse them in allylamine to introduce reactive radicals on the polycarbonate surface that would later

react with the unsaturated bond of allylamines. The second approach was the direct interfacial reaction of polycarbonate with amine containing molecules, APTMS or CysA.

#### *4.2.3.1 Nitrogen plasma and argon/allylamine plasma treatment*

Bare (non-modified) membranes were subjected to pure nitrogen plasma treatment. A plasma etching system (PX-250, March Instruments, Concord, CA), connected to a pure nitrogen supply at 9 scfm constant flow was used to generate the plasma. After 5 minutes of plasma treatment, membranes were immersed in silver hydrosol for 24 hours. In a separate set of experiments, bare membranes were subjected to pure argon plasma treatment using the plasma etching system and flow rate described above. After 5 minutes of plasma treatment, membranes were immersed in a 1 % by weight allylamine aqueous solution for 5 minutes, rinsed with ultrapure water for 1 hour and immersed in silver hydrosol for 24 hours. After each treatment, membranes were separated from the silver sol and rinsed with ultrapure water to eliminate excess hydrosol. The modified membranes were kept in ultrapure water until further use.

#### *4.2.3.2 APTMS used as a linker*

It has been shown that closely packed arrays of gold and silver particles can be assembled on a surface of a glass slide modified with APTMS [42]. Other studies have shown that aminosilanes react with polycarbonate via the amino group [43]; the proposed reaction pathway for the APTMS/polycarbonate reaction can be seen in Fig. 4.1. The membranes

were immersed in a 25 % by weight solution of APTMS in methanol for 5 minutes. After incubation in APTMS, membranes were rinsed in pure methanol for 45 minutes with three changes of the solvent. After the final rinse, membranes were immersed in silver hydrosol for 24 hours. Aggregation of silver suspension in the immediate vicinity of the derivatized membrane initiated by residual physisorbed APTMS was indicative of poor rinsing and such samples were discarded. The aggregation could be recognized by an initial darkening of the suspension, a gradual increase in transparency, and appearance of a lilac tint in the suspension. Prolonged rinsing in methanol was found to be necessary to avoid these effects.

#### *4.2.3.3 CysA used as a linker*

In the case of CysA, the amino group would preferentially react with the polycarbonate surface leaving an available thiol group for silver chemisorption. The membranes were immersed in a 3.24 mol/L aqueous solution of CysA for 60 minutes. After CysA incubation, membranes were rinsed in ultrapure water for 15 minutes with three changes of the solvent. After the final rinse, membranes were immersed in silver hydrosol for 24 hours.

#### **4.2.4 XPS, UV-vis, Raman and SERS measurements**

XPS measurements of bare and APTMS-modified membranes were conducted using PHI 5400 ESCA system (Physical Electronics, Chanhassen, MN), equipped with a

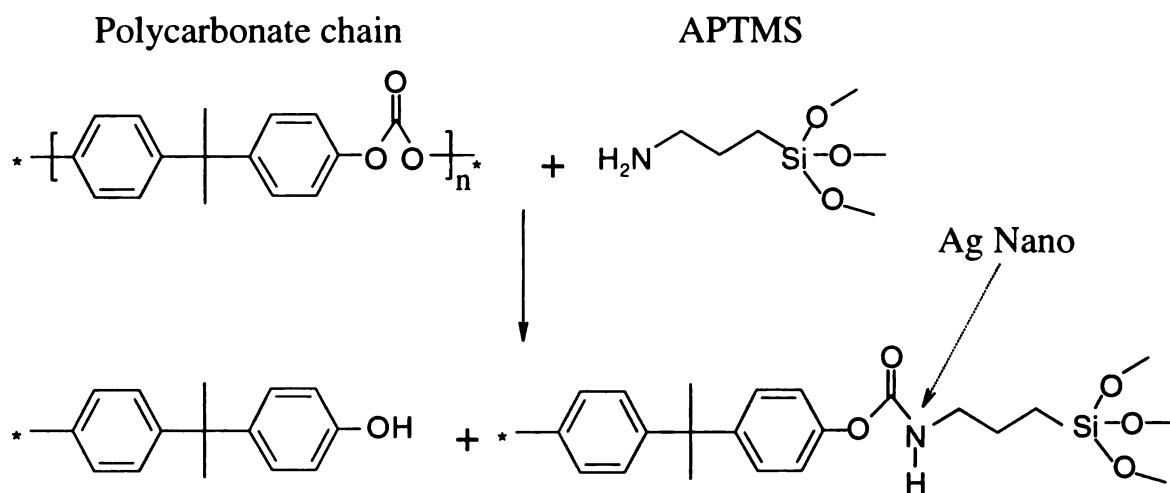


**Figure 4.1.** Proposed mechanism for the APTMS reaction with polycarbonate and further silver chemisorption to the incorporated nitrogen.

non-monochromatic Mg X-Ray. Measurements were done using a take off angle of 45 degrees. Raman and SERS spectra were recorded at a spectral resolution of  $5\text{ cm}^{-1}$  and coverage from  $250\text{ cm}^{-1}$  to  $4,000\text{ cm}^{-1}$  using Kaiser Optical Systems HoloProbe Raman spectrograph coupled to an Olympus BX-60 optical microscope and equipped with a motorized sample stage. A frequency doubled YAG laser emitting at 532 nm with a beam power of 5 mW was employed as the excitation source. The laser spot diameter was less than  $2\text{ }\mu\text{m}$  (with 100x objective). Exposure times (5 ms to 5 s) and the number of accumulations (1 to 25) were adjusted in each measurement to avoid detector saturation. Measured intensity values were normalized to account for variations in exposure times and accumulations. To record Raman signal from membrane-based substrates, the substrates were placed on the sample stage with the SERS-active surface facing the microscope lens. To record Raman signal from liquid samples and hydrosols, the samples were transferred to glass capillaries with ca. 2 mm internal diameter; the laser beam was then focused on the center of the capillary containing the sample.

UV-vis absorption spectra of the silver hydrosol and treated membranes were recorded using a photodiode array spectrophotometer (Multi-Spec 1501, Shimadzu, Kyoto, Japan). Spectral coverage was from 180 nm to 800 nm with a spectral sampling interval of 1 nm and with 100 accumulations per measurement. Absorption spectra of ultrapure water and bare membranes were used as baselines in measurements of absorption of hydrosols and treated membranes, correspondingly. Measurements were performed using square quartz cells of 3 mL nominal capacity (Fisherbrand quartz, Fisher Scientific International, Hampton, NH).

#### **4.2.5 Particle size and zeta potential measurements**

Particle size distribution of the prepared silver hydrosol was measured using multi-angle light scattering apparatus (ZetaPALS, BI\_MAS Option, Brookhaven Instrument Corp., Holtsville, NY ) equipped with a solid state laser emitting 15 mW beam at 660 nm. Measurements were recorded in 10 cycles of 2 minutes each, with a 30 % cutoff dust filter, using 3 mL sample cells provided by the equipment manufacturer. Samples were diluted in a 10 mmol/L KCl solution to reach a measurement count rate in the range of 50 kcps to 500 kcps. Zeta potential was measured by phase analysis light scattering (ZetaPALS, Brookhaven Instrument Corp., Holtsville, NY) using the same laser line as the particle sizing module described above. Measurements were conducted in 10 runs of 10 cycles each, using 3 mL sample cells provided by the equipment manufacturer. Samples were diluted in a 1 mmol/L KCl solution prior to measurements.

#### **4.2.6 SEM and TEM imaging**

SEM imaging was carried out using Hitachi S-4700II Field Emission scanning electron microscope operated in high vacuum, ultra high resolution mode. Samples were mounted on aluminum SEM specimen stubs, membrane sample surfaces were made conductive by sputtering gold on them for 3 minutes at a current of 20 mA (Emscope SC 500 sputter coater) prior to the SEM imaging. For higher resolution, smaller electron beam spot size and shorter working distances were employed. Samples were also imaged by transmission electron microscopy (JEOL JEM 2010, JEOL USA, Inc., Peabody, MA).

Copper (cat. no. 3HGC500, Electron Microscopy Sciences, Hatfield, PA) and formvar carbon covered copper (cat. no. 200-CU) TEM grids were used to support the samples. The grids were drop-coated by Ag hydrosol and examined at an accelerating voltage of 100 kV.

#### **4.2.7 SERS characterization of APTMS modified membranes**

To assess the Raman enhancing properties of membrane-based substrates, methylene blue (MB) was used as a test compound. Aqueous solutions of MB with concentrations ranging from  $10^{-4}$  mol/L to  $10^{-7}$  mol/L were tested on the modified membranes. 20  $\mu$ L of each solution were dropped on the surface of a modified membrane and let to dry (“drop and dry” method). For each concentration, measurements were conducted on five different membranes, on three different areas of each membrane’s surface.

#### **4.2.8 Membranes filtration performance**

Clean water flux tests were conducted to determine intrinsic membrane resistance. Amicon 8010 ultrafiltration cell (Millipore Corp, Billerica, MA) was used as the membrane module. Variable feed water flow rate was achieved by varying the delivery pressure of the compressed zero air tank. Ultrapure water was stored in a pressurized container (100 psi, 5L, Alloy Products Corp., Waukesha, WI). Pressurized air from the air tank pressure regulator (cat no. 8069621, Controls Corp. of America, VA. Beach, VA) connected to the inlet of the water container was used to deliver feed water to the

filtration cell. The permeate flux was measured continuously by collecting the filtered water on a digital weighing balance (AV8101C, Ohaus Corp., Pine Brook, NJ) interfaced with a computer via a built-in RS-232 port. In all experiments, the feed water flow rate was sequentially increased by increasing the outlet pressure of the compressed zero air tank from 0 psi to 28 psi. The data from the weighing balance was logged to a computer using a program written in LabView (version 7.1, National Instruments). Data were acquired at a 5 s time interval. Clean water flux tests were conducted both for untreated membranes and modified membranes.

#### **4.2.9 Preconcentration studies**

A variable flow rate positive displacement pump (model XX80EL000, Millipore Corp, Billerica, MA) was used to deliver feed aqueous solution of MB into the filtration cell (Amicon 8010, Millipore Corp, Billerica, MA) containing the modified membrane. The permeate flux was directed back into the feed solution container to allow for continuous recirculation of the solution. Dilute solutions of the tested compound were recirculated through the APTMS modified membranes for 2 hours. To evaluate the effect of flow-induced preconcentration, a modified membrane was immersed for 2 hours in a solution of equal concentration to that used for the preconcentration experiments, and then let to dry.

### 4.3. Results and Discussion

#### 4.3.1 Silver nanoparticle hydrosol

Prepared hydrosols had suspended solids fraction of  $3 \times 10^{-4}$  by weight and ionic strength of ca.  $8.6 \times 10^{-3}$  mol/L, as calculated based on the amount of citrate and nitrate salts used in the preparation of the hydrosol. No aggregation was observed in the stored hydrosols over the duration of experiments. Figure 4.2 shows SEM and TEM micrographs of the silver nanoparticles. Two types of particles were observed – ones that were approximately spherical and ones that were rod shaped, the former type being clearly predominant.

Effective diameter of silver nanoparticles in the hydrosol, as measured using light scattering, was found to be  $58.8 \text{ nm} \pm 0.6 \text{ nm}$  with a polydispersity factor [44] of  $0.319 \pm 0.004$ . As Fig. 4.3 illustrates, particle size distribution profile of the sol shows two major peaks at 13.76 nm and 78.86 nm and two minor peaks with effective diameters higher than 500 nm. The first two peaks can be attributed to spherical particles. The peaks that correspond to larger particles together with the relatively high polydispersity of the measurement are likely to be due to the presence of rod-shaped particles that skew the size distribution pattern to higher diameters. To estimate the length of rod shaped particles, the following expression for the diffusion coefficient of rod-shaped particles can be used [45]:

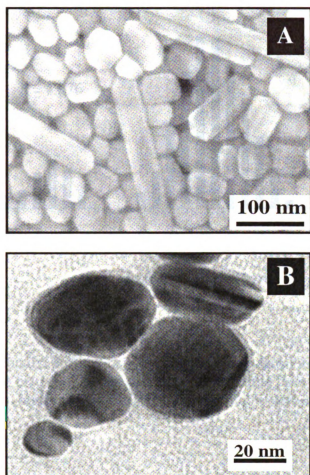


**Figure 4.2.**Micrographs of Ag nanoparticles: SEM image of filtered hydrosol (A), and TEM image of Ag nanoparticles deposited onto TEM grids by drop-coating (B).

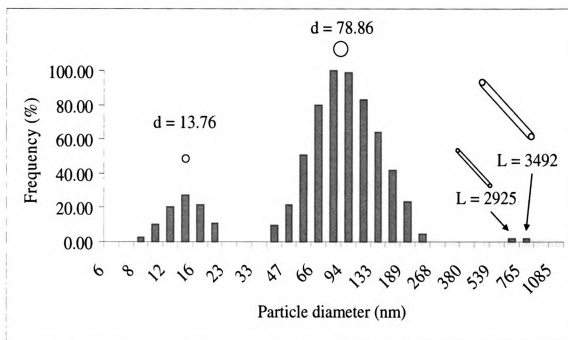


**Figure 4.3.** Size distribution profile of silver nanoparticle suspension. Also shown are the predominant spherical diameters for the two major distribution peaks, and the estimated rod lengths for the two high end size peaks (Schematics not to scale)

$$D = k_B T \frac{6 - 0.5(\gamma_{\parallel} + \gamma_{\perp})}{3\pi\eta_0 L}, \quad (1)$$

where

$$\gamma_{\parallel} = 1.27 - 7.4(\delta^{-1} - 0.34)^2, \quad \gamma_{\perp} = 0.19 - 4.2(\delta^{-1} - 0.39)^2, \quad \delta = \ln\left(\frac{2L}{w}\right)$$

and  $D$  is the particle diffusion coefficient;  $k_B$  is the Boltzmann constant,  $T$  is the absolute temperature,  $\eta_0$  is the viscosity of the suspending liquid,  $L$  is the rod length, and  $w$  is the rod width. By comparing equation (1) and the expression for the diffusion coefficient of

spherical particles,  $D = \frac{k_B T}{3\pi\eta_0 d}$  (2), a relationship between sphere diameter and rod

length for an equal diffusion coefficient can be obtained:

$$L = d[6 - 0.5(\gamma_{\parallel} + \gamma_{\perp})]. \quad (3)$$

Using the above analysis, the equivalent rod lengths were calculated to be ca. 2.9  $\mu\text{m}$  and 3.5  $\mu\text{m}$ .

Zeta potential of the silver sol, calculated using the Smoluchowski model, was found to be  $-24.27 \text{ mV} \pm 0.98 \text{ mV}$ , which was indicative of a stable suspension.

### 4.3.2 Modified membranes characterization

#### 4.3.2.1 Surface chemistry

To evaluate surface chemistry of membranes derivatized with APTMS, XPS studies were conducted. Prior to treatment, XPS analysis showed the presence of carbon and oxygen with peaks C(1s)[0.314] = 84.14 % and O(1s)[0.733] = 15.86 %, in accordance with the chemical composition of a bare polycarbonate surface. After APTMS treatment, nitrogen and silica peaks appeared as follows, C(1s)[0.314] = 77.70 %, N(1s)[0.499] = 1.80 %, O(1s) [0.733] = 18.75 % and Si(2p)[0.368] = 1.75 % indicating the presence of APTMS at the membrane surface.

#### *4.3.2.2 Silver nanoparticle array morphology*

Under the hydraulic conditions tested in our experiments, particles were not removed from the membrane surface. However, under mechanical stress, such as tapping or scratching, the particles could be easily removed; the modified membranes, therefore, were handled using tweezers and were stored immersed in ultrapure water in a Petri dish.

The distribution of nanoparticles on the membrane surface was evaluated using SEM imaging. Figure 4.4 A illustrates the flat surface and narrow pore size distribution of a bare PCTE membrane. Figure 4.4 (B, D) shows the membrane surface after modification by APTMS and silver. Homogeneous sub-monolayer coverage of the membrane surface by silver nanoparticles, as well as some internal pore coverage can be observed. The membrane surface coverage by silver particles was determined using image processing (ImageJ v1.34s, National Institutes of Health, USA) of SEM micrographs of modified membranes (Figures 4.4 B, 4.4 D). The surface coverage was calculated to be 56.6%.

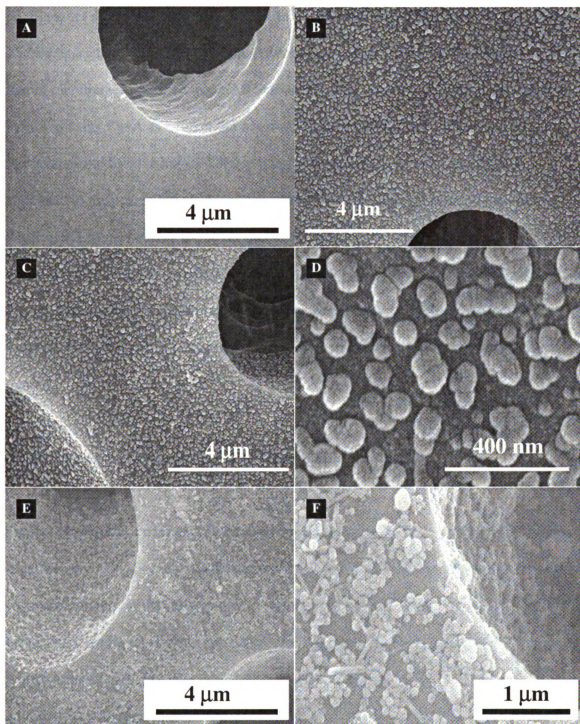


**Figure 4.4.** SEM micrographs of PCTE membrane filter that is non-modified (A), modified using APTMS linker (B, C, D), and modified using CysA linker (E, F).

(E, F) shows silver nanoparticle coverage of a CysA-modified membrane; in this case surface aggregation is evident and the coverage is less homogeneous in comparison with that of membranes modified using APTMS as a linker. Interestingly, those membranes modified using CysA as a linker did not show Raman enhancement properties while membranes modified using APTMS as a linker were SERS-active. This could be attributed to the possibility of chemisorption of remnant cysteamine molecules onto the silver nanoparticles during the silver immersion stage of membrane modification. This would hamper direct analyte-silver nanoparticle interaction and weaken SERS signal. Plasma treatments with subsequent incubation of treated membranes in the silver hydrosol did not result in any noticeable coverage of the membranes surface by silver particles.

#### *4.3.2.3 Optical properties of modified membranes*

Optical properties of nanoparticle arrays were studied with UV-vis absorption and Raman spectroscopy. UV-vis analysis of the modified membranes was possible due to the semi-translucent nature of the membranes. In the absorption spectrum of the Ag hydrosol, a broad band at 410 nm is observed, which corresponds to the surface plasmon resonance within primary particles. The same band, but blue shifted by  $(13.2 \pm 1.5)$  nm (95 % confidence) with respect to the silver sol absorption peak was observed for the silver nanoparticles attached to the modified membranes (Fig. 4.5). The shift was attributed to preferential exclusion of larger particles, including rod-shaped particles, from the membrane surface, as indicated by SEM results. The fact that a band at larger

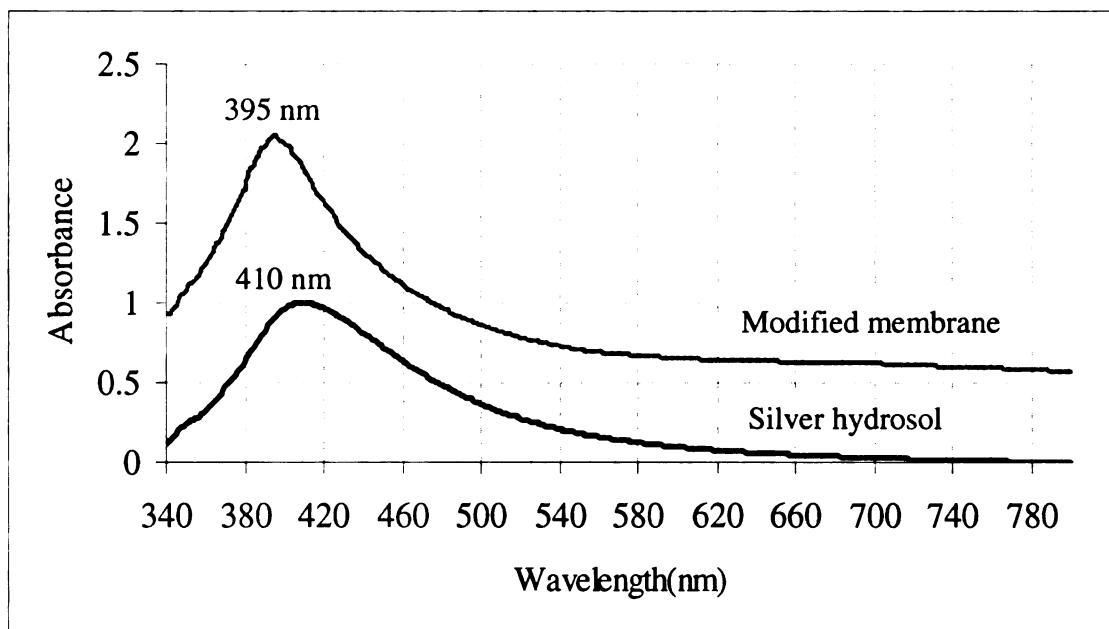


**Figure 4.5.** UV-vis spectra of a modified PCTE membrane (bare membrane used as baseline), and of silver hydrosol (250  $\mu$ L in 2 mL ultrapure water, ultrapure water used as baseline).

wavelengths does not emerge in the absorption spectrum of the modified membrane points to the absence of electromagnetic coupling between primary particles that is at the absence of surface aggregation. This observation is corroborated by SEM imaging results.

To evaluate Raman enhancing properties of modified membranes and compare them with those of source hydrosols, MB was chosen as the test compound. Figure 4.6 shows UV and Raman spectra of MB with relevant band assignments [46]. The excitation wavelength used in this work was 532 nm that is far from the resonance frequency of MB. Much lower detection limits, and perhaps higher enhancements factors, could have been observed had the resonant excitation been chosen. Nonetheless, this laser line is suitable for the comparison of modified membranes and silver hydrosol with respect to their Raman enhancing properties, which was one of the goals of this study.

First, Raman spectra of bare and modified membranes were recorded. In contrast to the spectrum of the bare membrane, the spectrum of the modified membrane was found to be relatively featureless (Fig. 4.7). Raman spectra of aqueous solutions of MB with concentrations ranging from  $10^{-7}$  mol/L to  $10^{-2}$  mol/L were then measured. The two most intense peaks on the Raman spectrum,  $1401\text{ cm}^{-1}$  and  $1626\text{ cm}^{-1}$ , correspond to the symmetric CN stretch and CC ring stretch, respectively. A linear increase in Raman intensity for both these peaks was observed for solutions in the  $10^{-5}$  mol/L to  $10^{-3}$  mol/L

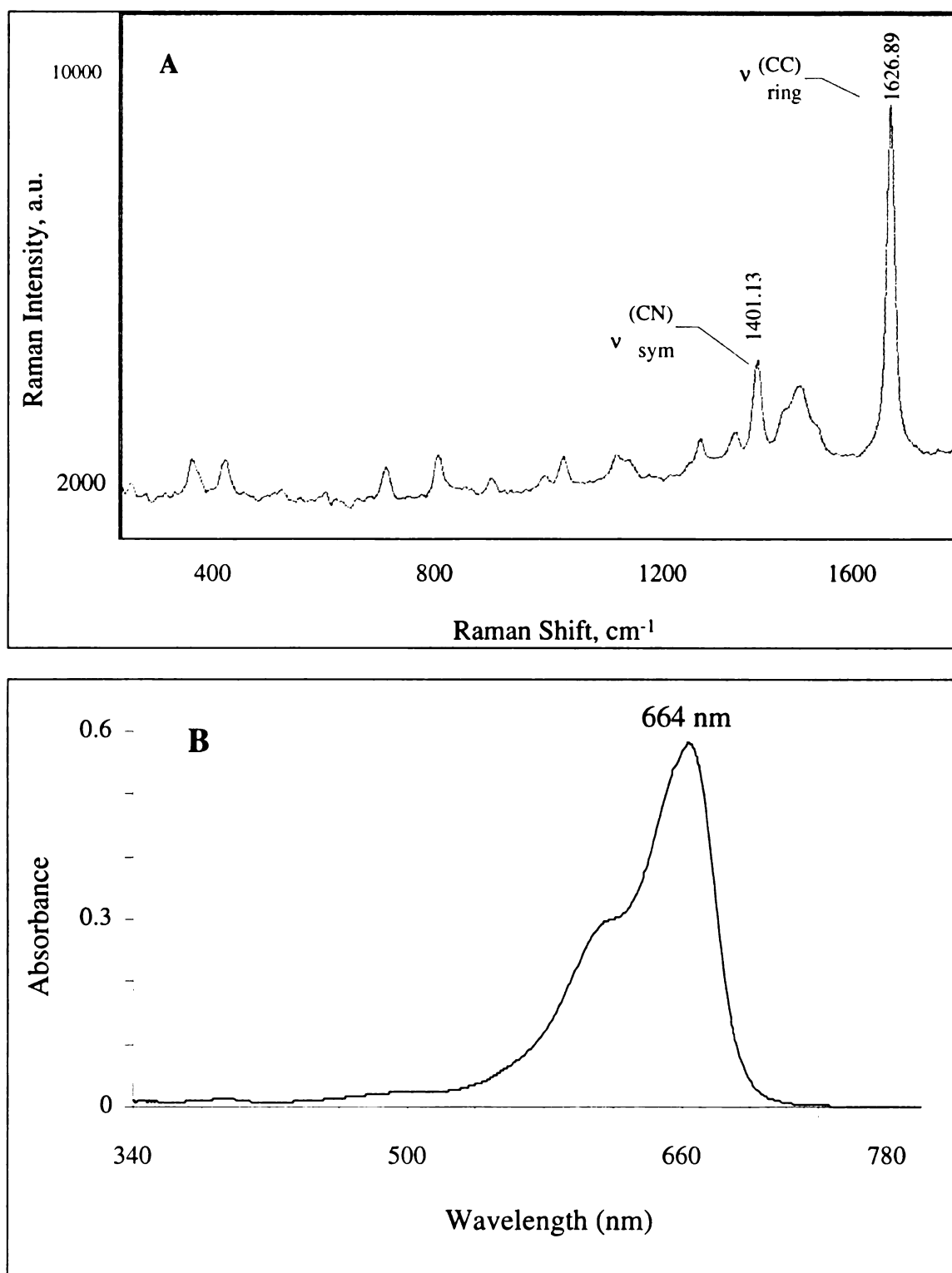


**Figure 4.6.** Absorption (A) and Raman spectra (B) of methylene blue.

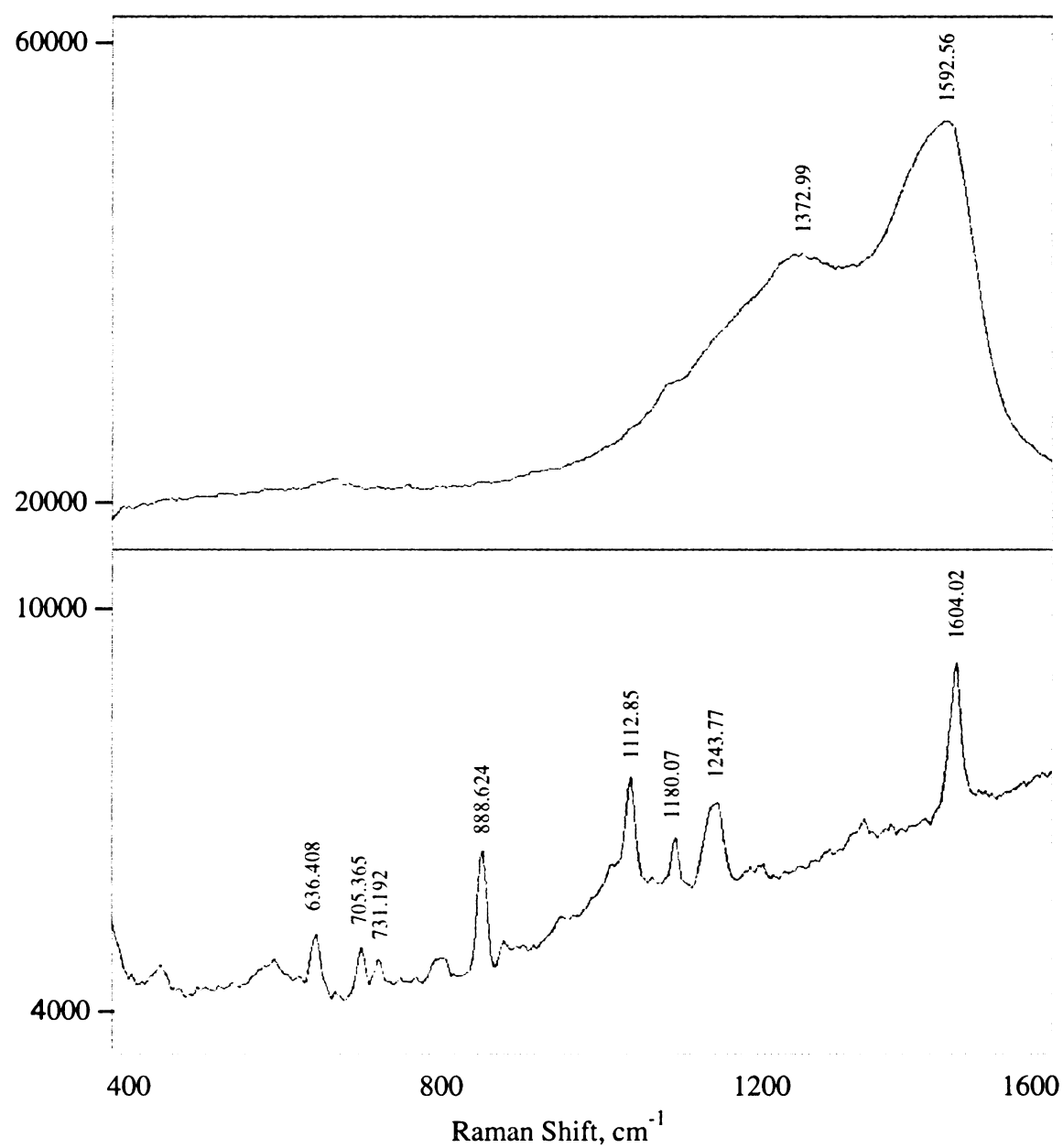


**Figure 4.7.** Raman spectra of an untreated membrane (bottom) and modified membrane (top). Y-axis label: Raman Intensity (a.u).

range. To avoid saturation effects, Raman intensity recorded for  $10^{-4}$  mol/L solutions was used in the computation of enhancement SERS enhancement factors.

To evaluate the Raman enhancement of assembled nanoparticle arrays, Raman spectra from solutions of known concentrations of MB on the membrane surface were recorded and compared to those obtained from the same solution concentrations on the precoagulated silver hydrosol. Figure 4.8 shows the Raman spectra recorded for a 1 mmol/L solution of MB, and the enhanced peaks from silver sol and modified membrane at  $1626\text{ cm}^{-1}$ . A slight shift of the peaks can be observed, pointing to varying MB/silver nanoparticles interactions for the different enhancing substrates. To calculate the enhancement factors of the silver sol and the modified membranes, the following equation was used:

$$EF = \frac{I_a C_b}{I_b C_a}, \quad (4)$$

where  $I_a$  and  $I_b$  indicate the normalized Raman intensities for a given peak,  $I_a$  being the enhanced intensity (from the Ag hydrosol or the modified membranes) and  $I_b$  the comparative basis, at MB concentrations  $C_a$  and  $C_b$ . By comparing intensities of the  $1626\text{ cm}^{-1}$  peak in the SERS spectrum of a) 0.01 mmol/L solution of MB at the modified membrane surface and b)  $10^{-6}$  mol/L solution of MB enhanced by precoagulated sol with Raman signal from  $10^{-4}$  mol/L aqueous MB solution, average enhancement factors of 157.9 (t95%=141.3) and 111.7 (t95%=11.8) were obtained for silver sol and modified membrane, respectively, considering all possible intensity combinations between

enhanced peaks and source MB peaks. While the EF of the sol is slightly higher than that of the modified membrane, so is the standardized error, indicating that the modified

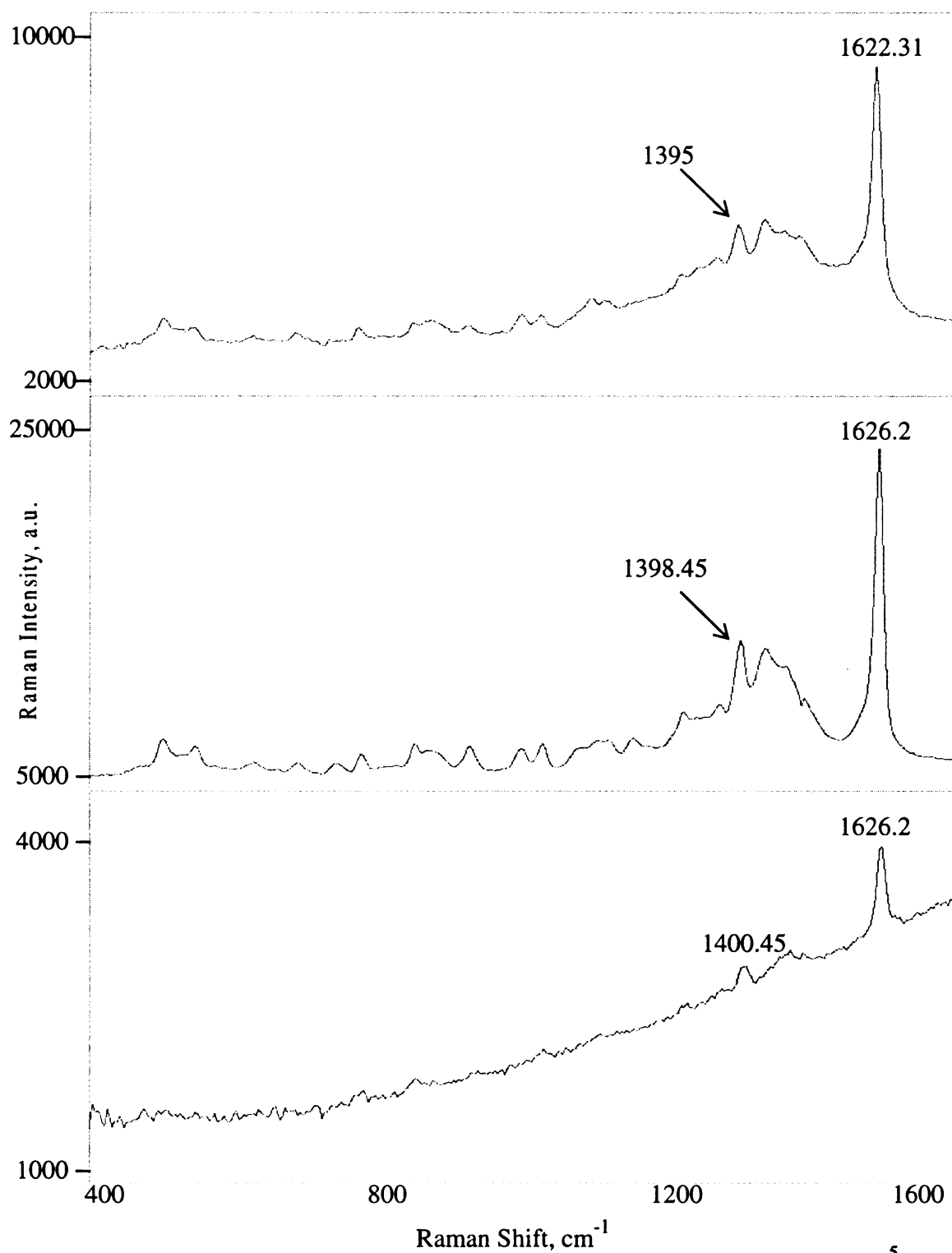


**Figure 4.8.** Raman spectrum of a 1 mmol/L aqueous solution of MB (bottom), a  $10^{-5}$  mol/L aqueous solution of MB in pre-coagulated silver sol (middle), and a  $10^{-5}$  mol/L aqueous solution of methylene blue after “drop and dry” on a modified membrane (top).

membranes have better SERS reproducibility than the sols. The observed EF values are summarized in the Fig. 4.9. The main body (box) of the plot encloses the middle 50% range of the EF measurements (and excludes lower and upper quartiles of the data set) while the line that crosses the box corresponds to the EF data median. Whiskers indicate the sample maximum and minimum, and open circles correspond to outliers. As can be seen from Fig. 4.9; the spread in EF values significantly higher for the precoagulated sol than for sols, indicative of lower reproducibility. A narrower and more symmetric distribution can be observed for the modified membranes; also, the median value of EF from modified membranes was higher than that for the hydrosol.

#### *4.3.2.4 Filtration performance of modified membranes*

To study possible changes in the filtration performance of membranes after modification, clean water flux tests were conducted both for untreated membranes and nanoparticle-modified membranes (Fig. 4.10). Membrane resistance was calculated to be  $(1.09 \cdot 10^7 \pm 0.01) \text{ m}^{-1}$  and  $(1.15 \cdot 10^7 \pm 0.02) \text{ m}^{-1}$  for bare and modified membranes, respectively. As Fig. 4.10 illustrates, the flux versus pressure trendline was drawn for the first three points only, using linear least square fitting. The subsequent points were not considered since they did not follow the linear trend, likely due to membrane pore constriction at higher transmembrane pressure differentials. The above measurements clearly indicate that the particle attachment to membrane surface did not result in any significant changes in the membrane resistance.

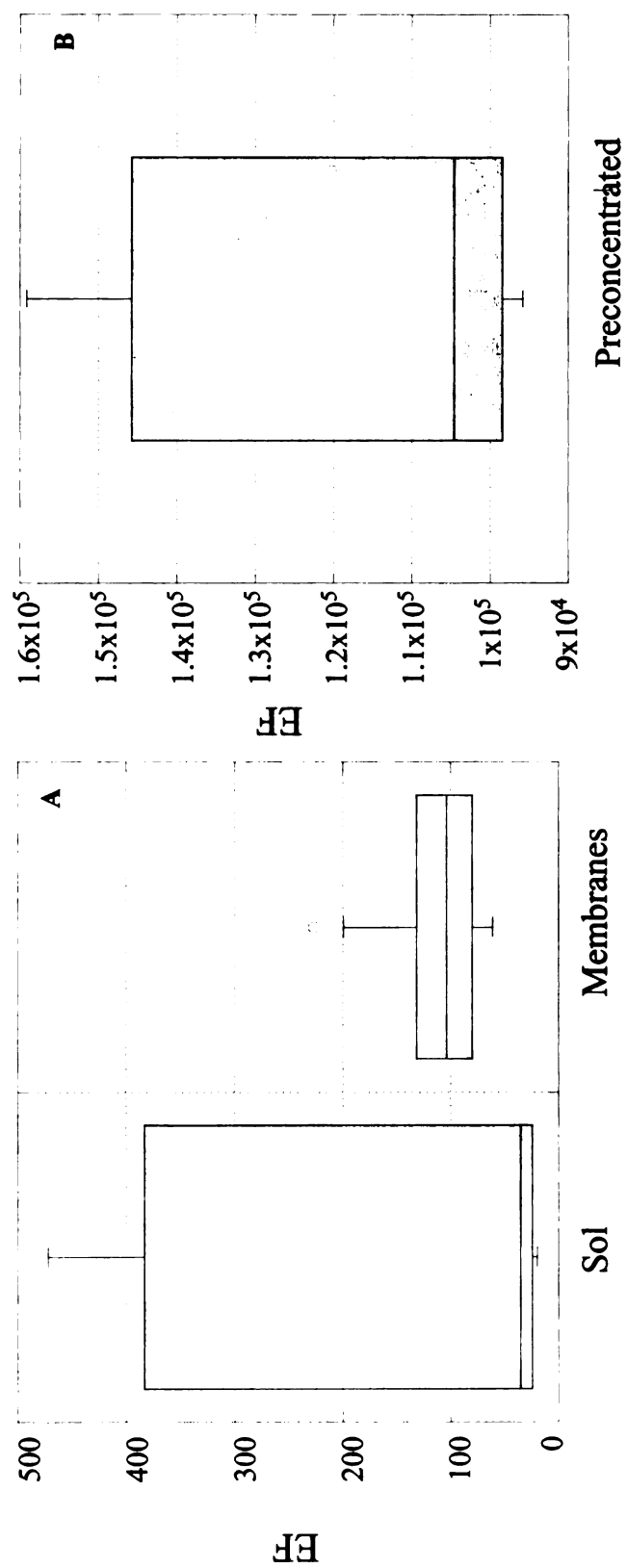


**Figure 4.9.** Box plots for enhancement factors of MB on precoagulated sol and modified membranes (A) and after preconcentration of modified membranes (B).

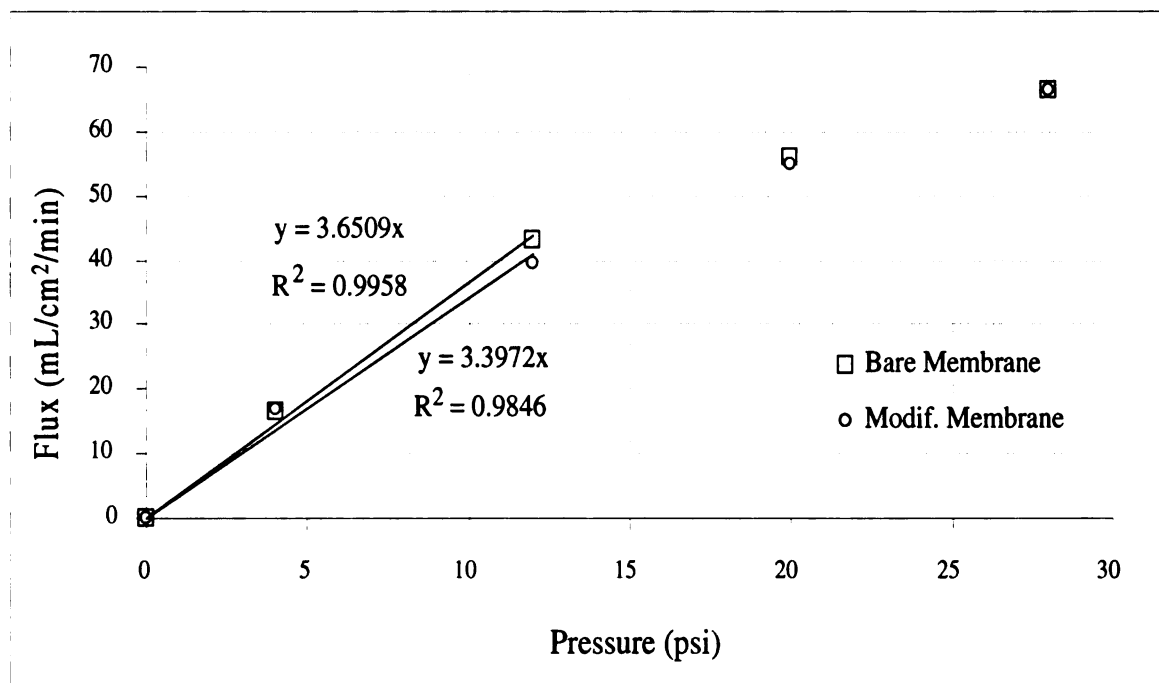


**Figure 4.10.**Results of clean water flux test for bare and modified membranes.

#### 4.3.2.5 Preconcentration

We considered sensitivity in a broader context that included membrane-enabled preconcentration as the factor that augments the inherently high sensitivity of nanoparticle-based SERS substrates. To evaluate the effect of preconcentration on the sensitivity of the developed sensors, an aqueous solution of known concentration ( $10^{-7}$  mol/L) of MB was filtered through the membrane at a constant volume flow of 4 mL/sec for 2 hours. The membrane was let to dry and the SERS spectrum of MB at the membrane surface was then recorded. To ensure that any increased enhancement was solely due to preconcentration, parallel measurements were conducted both for modified membranes immersed in a  $10^{-7}$  mol/L MB(aq) solution for 2 hours, and modified membranes inoculated with a  $10^{-7}$  mol/L MB (aq) solution using “drop and dry” method. While no MB peaks were observed in the SERS spectrum from the modified membranes after “drop and dry” or 2 hours immersion, preconcentration resulted in the appearance of the  $1390\text{ cm}^{-1}$  peak (Fig. 4.11). For all tested membranes, the preconcentration experiments have reproducibly resulted in an improved detection limit. Interestingly, the MB peak at  $1627\text{ cm}^{-1}$  did not appear after preconcentration, instead, the  $1401\text{ cm}^{-1}$  peak was shifted  $10\text{ cm}^{-1}$  with respect to its original position. Shifts could also be noticed at the precoagulated sol and modified membranes; the shifts in SERS are indicative of the disturbance of the electronic configuration of an analyte due to chemisorption. We attribute the difference in SERS spectra from MB chemisorbed by the

“drop and dry” method and chemisorbed during preconcentration experiments to the different molecule-surface interactions. Convective forces present during

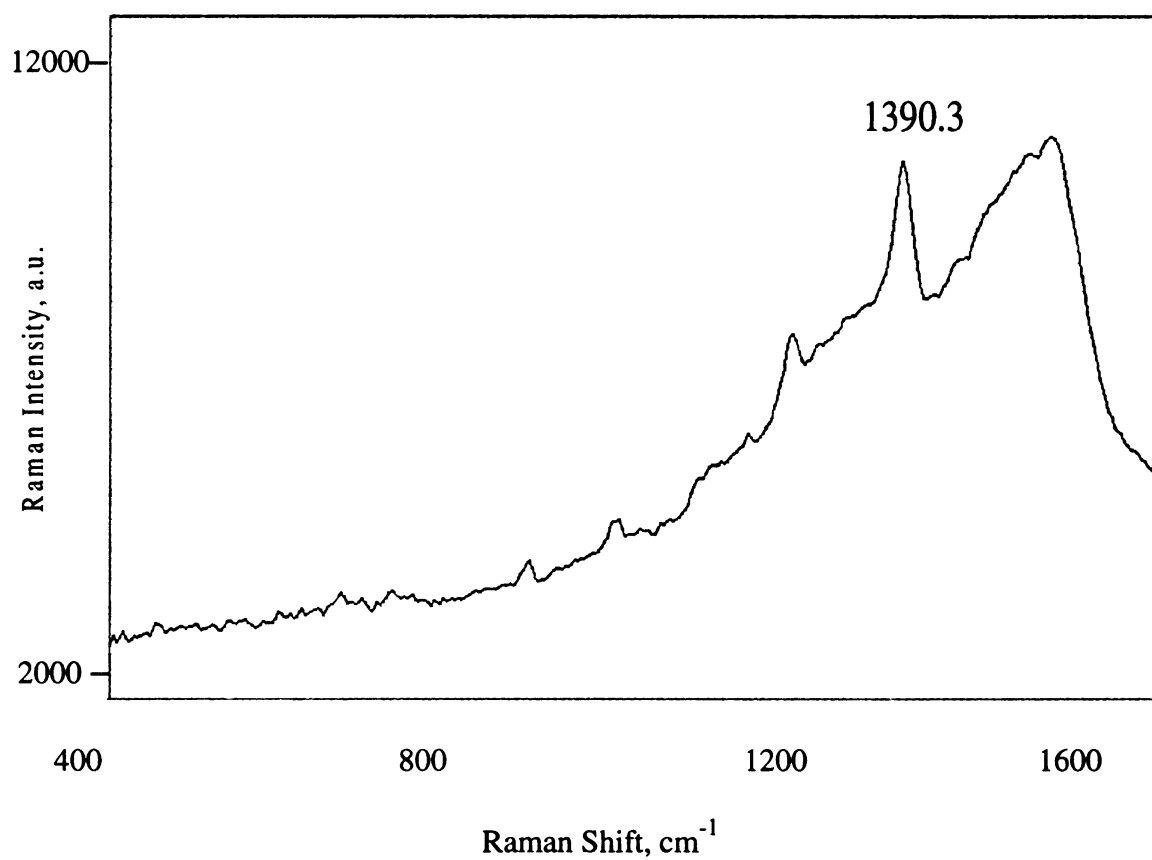


**Figure 4.11.** Raman spectrum of a  $10^{-7}$  mol/L aqueous solution of MB after 2 hours of pre-concentration on a modified membrane.

preconcentration together with the natural hydrophobicity of the membrane substrates might favor MB chemisorption to the silver nanoparticles through the CN bond, rather than through the less polar CC bond, which could explain the predominance of the CN peak.

Based on the intensity of the  $1401\text{ cm}^{-1}$  band in the Raman spectrum of a  $10^{-2}\text{ mol/L}$  MB aqueous solution, the enhancement factor (EF) was calculated using (4) to be  $1.17 \cdot 10^5$  ( $t_{95\%} = 1.92 \cdot 10^4$ ); the data distribution can be observed in Figure 4.9 B. This result shows that preconcentration is effective in increasing the enhancement provided by the membrane substrate and that the detection limit can be significantly lowered (since by “drop and dry” or prolonged immersion no detection of MB  $10^{-7}\text{ mol/L}$  was possible). Additionally, the spread in the measurements (with respect to the EF value) is one order of magnitude lower than the averaged EF; for precoagulated silver sols the the relative width of the spread is considerably larger.

The effect of convective flow across the membrane on the improved MB adsorption to nanoparticles immobilized on the membrane surface can be rationalized in terms of diffusive and convective transport of analyte molecules. The thickness of the boundary layer formed by a fluid in motion in the vicinity of a flat plate can be roughly estimated as [47]:

$$\delta = \sqrt{\frac{\nu l}{u}}, \quad (5)$$

where  $\delta$  is the boundary layer thickness,  $\nu$  is the kinematic viscosity of the fluid,  $l$  is the plate length, and  $u$  is the velocity of the fluid far from the surface. In our experiments,  $u = j / A$ , where  $j$  is the volumetric flowrate and  $A$  is the membrane area. Given that  $u = 0.8 \cdot 10^{-4}$  m/s and taking  $l$  to be the average distance between pores (ca. 16  $\mu\text{m}$ ), the thickness of the boundary layer can be estimated from (5) to be ca. 45  $\mu\text{m}$ . The time it takes for a molecule to be transported by Brownian diffusion across the boundary layer is then given by:

$$t_d = \frac{\langle \delta \rangle^2}{2D}, \quad (6)$$

where  $D$  is the diffusion coefficient of the solute. By estimating the molar volume of MB by the LeBas method [48] and using Hayduk-Laudie correlation [49] applicable to small (MW < 1000 Da) non-electrolyte solutes to estimate the diffusion coefficient of MB, we obtain  $D \approx 2.96 \cdot 10^{-10}$  m<sup>2</sup>/s. Now, using (6)  $t_d$  is estimated to be ca 3.4 ms, which is of the same order of magnitude as time  $t_c \approx l / u = 2$  ms that the analyte molecule spends in the vicinity of the membrane. This means that by imposing the convective flow, the boundary layer is compressed sufficiently in our experiments, for the MB molecules to be able to diffuse across the boundary layer to the upstream membrane surface as they are transported by the convective flow past the membrane surface and into the membrane pore.

This balance between convective and diffusive transport can also be viewed in terms of the probability of a solute molecule to reach (and chemisorb to) the silver coated membrane surface. Equation (6) can be rewritten as:

$$u_d = \frac{2D}{d}, \quad (7)$$

where  $u_d$  can be interpreted as the velocity of a solute that travels a distance  $d$  due to Brownian motion. A “pseudo” Peclet number can be obtained as the ratio of convective to diffusive velocities:

$$\frac{u}{u_d} = \frac{ud}{2D} \quad (8)$$

As can be seen from equation (8), this ratio will be directly proportional to the convective velocity and the distance from the membrane surface. For a fixed  $u$ , for all distances

$d > \frac{2D}{u}$  the ratio (8) will be higher than one, implying that more molecules will be

driven to the membrane per unit time when convection is present, than when only diffusion occurs, thereby enhancing mass transport of the analyte to the membrane surface.

#### **4.4. Conclusions**

Silver nanoparticle arrays were assembled on track etch membrane supports and established to be SERS-active with reproducible Raman enhancements. The improved reproducibility was attributed to the well defined geometry of track etch membranes. The hydrodynamic control of analyte transport to the permeable SERS-active surface was demonstrated to allow for a dramatic improvement of the detection limit of the sensor. Better insight into processes that govern analyte partitioning from dissolved phase onto the surface of the permeable substrate is needed; boundary layer structure, membrane morphology, and surface chemistry of membrane and SERS-active sites are likely to determine the extent of preconcentration. The reported findings indicate the potential benefit of combining high specification SERS-active systems and the flow-through design for the development of analytical sensors for the trace detection of pollutants in water.

## **Acknowledgements**

This material is based upon work supported by the National Science Foundation under Grant No. OISE-0530174. Authors thank Eliza Tsui (Rice University) for recording TEM images of silver hydrosol particles and Dr. Jérôme Rose (Centre Européen de Recherche et d'Enseignement des Géosciences de l'Environnement) for assisting with high resolution SEM imaging of filtered Ag hydrosol particles. Helpful comments by two anonymous reviewers are gratefully acknowledged. Any opinions, findings, and conclusions or recommendations expressed in this material are those of the authors and do not necessarily reflect the views of the National Science Foundation.

## References

1. Water quality monitoring: A practical guide to the design and implementation of fresh water studies and monitoring programmes, ed. J. Bartram and R. Ballance. 1996: UNEP/WHO.
2. S. A. Hashsham, L. M. Wick, J. M. Rouillard, E. Gulari and J. M. Tiedje, Potential of DNA microarrays for developing parallel detection tools (PDTs) for microorganisms relevant to biodefense and related research needs, *Biosens. Bioelectron.* 20 (2004) 668-683.
3. M.D. Sobsey. Methods to identify and detect microbial contaminants in drinking water. in *Strategies for Drinking Water Contaminants*. 1999. Washington, DC: Commission on Geosciences, Environment and Resources.
4. J. Juliano and M.D. Sobsey. Simultaneous concentration of *Cryptosporidium*, bacteria and viruses from water by hollow fiber ultrafiltration. in *Water quality technology*. 1997. Denver, CO.: American Water Works Association.
5. H. A. Morales-Morales, G. Vidal, J. Olszewski, C. M. Rock, D. Dasgupta, K. H. Oshima and G. B. Smith, Optimization of a reusable hollow-fiber ultrafilter for simultaneous concentration of enteric bacteria, protozoa, and viruses from water, *Appl. Environ. Microbiol.* 69 (2003) 4098-4102.
6. W. Quintero-Betancourt, E. R. Peele and J. B. Rose, *Cryptosporidium parvum* and *Cyclospora cayetanensis*: a review of laboratory methods for detection of these waterborne parasites, *J. Microbiol. Methods* 49 (2002) 209-224.
7. T. M. Straub and D. P. Chandler, Towards a unified system for detecting waterborne pathogens, *J. Microbiol. Methods* 53 (2003) 185-197.
8. M. R. Wiesner and S. Chellam, The promise of membrane technologies, *Environ. Sci. Technol.* 33 (1999) 360.
9. M. G. Albrecht and J. A. Creighton, Anomalously intense Raman-spectra of pyridine at a silver electrode, *J. Am. Chem. Soc.* 99 (1977) 5215-5217.
10. A. Campion and P. Kambhampati, Surface-enhanced Raman scattering, *Chem. Soc. Rev.* 27 (1998) 241-250.
11. R. K. Chang and T. E. Furtak, *Surface Enhanced Raman Scattering*. 1982, New York: Plenum Press.
12. D. L. Jeanmaire and R. P. Vanduyne, Surface Raman spectroelectrochemistry.1. Heterocyclic, aromatic, and aliphatic-amines adsorbed on anodized silver electrode, *J. Electroanal. Chem.* 84 (1977) 1-20.

13. M. Moscovits, Surface-enhanced spectroscopy, *Rev. Modern Phys.* 57 (1985) 783-826.
14. T. Vo-Dinh, SERS chemical sensors and biosensors: New tools for environmental and biological analysis, *Sens. Actuators, B* 29 (1995) 183-189.
15. K. Kneipp, Y. Wang, H. Kneipp, I. Itzkan, R. R. Dasari and M. S. Feld, Population pumping of excited vibrational states by spontaneous surface-enhanced Raman scattering, *Phys. Rev. Lett.* 76 (1996) 2444-2447.
16. N. Weissenbacher, B. Lendl, J. Frank, H. D. Wanzelbock and R. Kellner, Surface enhanced Raman spectroscopy as a molecular specific detection system in aqueous flow-through systems, *Analyst* 123 (1998) 1057-1060.
17. P. A. Mosier-Boss and S. H. Lieberman, Detection of volatile organic compounds using surface enhanced Raman spectroscopy substrates mounted on a thermoelectric cooler, *Anal. Chim. Acta* 488 (2003) 15-23.
18. K.I. Mullen, L.G. Crane, D.X. Wang and K.T. Carron, Trace detection of ionic species with surface enhanced raman spectroscopy, *Spectroscopy* 7 (1992) 24-32.
19. S. Sanchez-Cortes, C. Domingo, J. V. Garcia-Ramos and J. A. Aznarez, Surface-enhanced vibrational study (SEIR and SERS) of dithiocarbamate pesticides on gold films, *Langmuir* 17 (2001) 1157-1162.
20. T. Vo-Dinh, Surface-enhanced Raman spectroscopy using metallic nanostructures, *Trends Anal. Chem.* 17 (1998) 557-582.
21. N. Weissenbacher, B. Lendl, J. Frank, H. D. Wanzelbock, B. Mizaikoff and R. Kellner, Continuous surface enhanced Raman spectroscopy for the detection of trace organic pollutants in aqueous systems, *J. Mol. Struct.* 410 (1997) 539-542.
22. K. Kneipp, H. Kneipp, R. Manoharan, E. B. Hanlon, I. Itzkan, R. R. Dasari and M. S. Feld, Extremely large enhancement factors in surface-enhanced Raman scattering for molecules on colloidal gold clusters, *Appl. Spectrosc.* 52 (1998) 1493-1497.
23. Z. X. Luo and Y. Fang, SERS of C-60/C-70 on gold-coated filter paper or filter film influenced by the gold thickness, *J. Colloid Interface Sci.* 283 (2005) 459-463.
24. M. Volkan, D. L. Stokes and T. Vo-Dinh, A sol-gel derived AgCl photochromic coating on glass for SERS chemical sensor application, *Sens. Actuators, B - Chem.* 106 (2005) 660-667.
25. Y. Kurokawa and Y. Imai, Surface-enhanced Raman-scattering (SERS) using polymer (cellulose-acetate and Nafion) membranes impregnated with fine silver particles, *Journal of Membrane Science* 55 (1991) 227-233.

26. J. J. Laserna, A. D. Campiglia and J. D. Winefordner, Surface-enhanced Raman spectrometry on a silver-coated filter-paper substrate, *Anal. Chim. Acta* 208 (1988) 21-30.
27. A. S. L. Lee and Y. S. Li, Surface-enhanced Raman-spectra using silver-coated paper substrates, *J. Raman Spectrosc.* 25 (1994) 209-214.
28. M. Muniz-Miranda and M. Innocenti, AFM and micro-Raman investigation on filters coated with silver colloidal nanoparticles, *Appl. Surf. Sci.* 226 (2004) 125-130.
29. R. J. Walsh and G. Chumanov, Silver coated porous alumina as a new substrate for surface-enhanced Raman scattering, *Appl. Spectrosc.* 55 (2001) 1695-1700.
30. P. Apel, Track etching technique in membrane technology, *Radiat. Meas.* 34 (2001) 559-566.
31. K. P. Han, W. D. Xu, A. Ruiz, P. Ruchhoeft and S. Chellam, Fabrication and characterization of polymeric microfiltration membranes using aperture array lithography, *Journal of Membrane Science* 249 (2005) 193-206.
32. M. Bryjak, I. Gancarz, G. Pozniak and W. Tylus, Modification of polysulfone membranes 4. Ammonia plasma treatment, *Eur. Polym. J.* 38 (2002) 717-726.
33. I. Gancarz, G. Pozniak and M. Bryjak, Modification of polysulfone membranes 3. Effect of nitrogen plasma, *Eur. Polym. J.* 36 (2000) 1563-1569.
34. C. Jama, O. Dessaux, P. Goudmand, B. Mutel, L. Gengembre, B. Drevillon, S. Vallon and J. Grimblot, Surface modifications of polycarbonate (PC) and polyethylene terephthalate (PET) by cold remote nitrogen plasma (CRNP), *Surf. Sci.* 352 (1996) 490-494.
35. K. R. Kull, M. L. Steen and E. R. Fisher, Surface modification with nitrogen-containing plasmas to produce hydrophilic, low-fouling membranes, *Journal of Membrane Science* 246 (2005) 203-215.
36. K. Schroder, A. Meyer-Plath, D. Keller, W. Besch, G. Babucke and A. Ohl, Plasma-induced surface functionalization of polymeric biomaterials in ammonia plasma, *Contrib. Plasma Phys.* 41 (2001) 562-572.
37. V. S. Foldi and T. W. Campbell, Preparation of copoly(carbonate-urethanes) from polycarbonates, *J. Polym. Sci.* 56 (1962) 1-9.
38. H. Ishida and Y. H. Lee, Study of exchange reaction in polycarbonate-modified polybenzoxazine via model compound, *J. Appl. Polym. Sci.* 83 (2002) 1848-1855.
39. S. E. Murinda, L. T. Nguyen, S. J. Ivey, B. E. Gillespie, R. A. Almeida, F. A. Draughon and S. P. Oliver, Molecular characterization of *Salmonella* spp. isolated from bulk tank milk and cull dairy cow fecal samples, *J. Food Prot.* 65 (2002) 1100-1105.

40. J. P. R. Pelletier, S. Transue and E. L. Snyder, Pathogen inactivation techniques, *Best Pract. Res. Clin. Haematol.* 19 (2006) 205-242.
41. P. C. Lee and D. Meisel, Adsorption and surface-enhanced Raman of dyes on silver and gold sols, *J. Phys. Chem.* 86 (1982) 3391-3395.
42. K. C. Grabar, R. G. Freeman, M. B. Hommer and M. J. Natan, Preparation and characterization of Au colloid monolayers, *Anal. Chem.* 67 (1995) 735-743.
43. G. L. Wilkes and C. Li, The mechanism for 3-Aminopropyltriethoxysilane to strengthen the interface of polycarbonate substrates with hybrid organic-inorganic sol-gel coatings, *J. Inorg. Organomet. Polym.* 7 (1997).
44. J. C. Brown, P. N. Pusey and R. Dietz, Photon Correlation Study Of Polydisperse Samples Of Polystyrene In Cyclohexane, *Journal Of Chemical Physics* 62 (1975) 1136-1144.
45. S. R. Mishra, H. S. Rawat, S. C. Mehendale, K. C. Rustagi, A. K. Sood, Ranjini Bandyopadhyay, A. Govindaraj and C. N. R. Rao, Optical limiting in single-walled carbon nanotube suspensions, *Chemical Physics Letters* 317 (2000) 510.
46. R. R. Naujok, R. V. Duevel and R. M. Corn, Fluorescence and Fourier-transform surface-enhanced Raman-scattering measurements of Methylene-Blue adsorbed onto a sulfur-modified gold electrode, *Langmuir* 9 (1993) 1771-1774.
47. H. Schlichting, *Boundary Layer Theory*. 1968, New York: McGraw Hill.
48. LeBas, *The molecular volumes of liquid chemical compounds*, ed. Longmans. 1915, London.
49. W. Hayduk and H. Laudie, Prediction of diffusion-coefficients for nonelectrolytes in dilute aqueous-solutions, *AIChE J.* 20 (1974) 611-615.

MICHIGAN STATE UNIVERSITY LIBRARIES



3 1293 03063 2008